Medical Image Segmentation and Analysis using Statistical Shape Modelling and Inter-Landmark Relationships

by

Karim Lekadir

A thesis submitted in partial fulfilment

of the requirements for the degree of

Doctor of Philosophy

of the

University of London

Department of Computing

Imperial College London

2009

Abstract

The study of anatomical morphology is of great importance to medical imaging, with applications varying from clinical diagnosis to computer-aided surgery. To this end, automated tools are required for accurate extraction of the anatomical boundaries from the image data and detailed interpretation of morphological information. This thesis introduces a novel approach to shape-based analysis of medical images based on Inter-Landmark Descriptors (ILDs). Unlike point coordinates that describe absolute position, these shape variables represent relative configuration of landmarks in the shape. The proposed work is motivated by the inherent difficulties of methods based on landmark coordinates in challenging applications. Through explicit invariance to pose parameters and decomposition of the global shape constraints, this work permits anatomical shape analysis that is resistant to image inhomogeneities and geometrical inconsistencies. Several algorithms are presented to tackle specific image segmentation and analysis problems, including automatic initialisation, optimal feature point search, outlier handling and dynamic abnormality localisation. Detailed validation results are provided based on various cardiovascular magnetic resonance datasets, showing increased robustness and accuracy.

Acknowledgement

I would like to thank Professor Yang for the opportunity and continued support, David Yates for showing me the right place at the right time, my parents for giving me the best they could, my five siblings, twelve nephews/nieces and those to come, my late uncle, Theodoros, Anil and Gerardo for the laughters, Uri and Alexei for the stimulating discussions, Vari and Martin McGowan for their warmth, Laurent for his philosophy, Kanwal and Ose for their kindness, Aurélia, the United Kingdom for making me feel at home ever since the first minute, France for all it gave me, Algeria and Mexico for all they taught me, all the staff of the Cafés around London where this thesis was partly written, the people in Charring Cross Hospital who put me back on my feet after two knee surgeries. Last but not least, I would like to thank Bob Lablaw, Antonin Dvorak, Herman Hesse, Charles Darwin, the original Linstead Hall, and Cucurrucucu Paloma.

Table of Contents

List of Figures

List of Tables

List of Acronyms

ASM	Active Shape Model
CT	Computed Tomography
ILM	Inter-Landmark Motion
ILD	Inter-Landmark Descriptor
LV	Left Ventricle
MRI	Magnetic Resonance Imaging
PCA	Principal Component Analysis
PDM	Point Distribution Model
RV	Right Ventricle

1

Introduction

1.1 Background

Anatomical shape analysis is an important topic of medical image computing, with applications to a range of clinical problems. For example, identification of changes in morphology is essential for assessing progression of diseases and efficacy of therapeutic measures. For dynamic objects such as the heart, changes in morphology may provide an insight into the contractile behaviour of the myocardium and its haemodynamic responses. Computational anatomy is also playing an increasingly important role in image guided surgery in terms of both pre-operative planning and intra-operative guidance. With the increasing capability of imaging devices, particularly real-time imaging techniques, there is a significant demand on automatic techniques for accurate delineation and interpretation of 3D anatomical morphology. Despite extensive efforts from the medical image computing community in the last 20-30 years, the development of automatic methods is faced with a number of challenges.

The first issue is that most anatomical structures are complex not only in terms of geometry but also due to considerable variation across subjects and time. As a result, it is generally difficult to accurately localise and quantify the target anatomical structure without detailed domain-specific knowledge. An active field of research is to develop either model or statistical based frameworks for incorporating prior knowledge of the anatomical structure. In this thesis, statistical shape modelling is used as the basis for capturing the variability of a family of anatomical shapes.

The second fundamental challenge is the adaptation of automatic methods to varying image features corresponding to the same anatomical structure. For imaging modalities such as Computed Tomography (CT), these features are relatively consistent due to the fact that pixel intensities are fully calibrated. This greatly facilitates the development of automatic image segmentation and analysis methods. For Magnetic Resonance Imaging (MRI), however, the versatility of the modality for capturing tissue property and functional indices such as flow, perfusion and diffusion, means that there is no single measure for defining the anatomical boundaries. Despite significant advances in recent years in image quality, inhomogeneities such as noise, motion artefacts, and missing/confusing structures are inevitable in patient studies. The ability of the algorithm in dealing with such inconsistencies is therefore important to the wider applicability of the method.

Finally, in practical situations, a degree of user interaction is often required to assist the computational techniques and overcome some of the problems described above. This is typically achieved by providing some expert knowledge about the subject-specific variability, by initialising the computational task with a rough starting estimate of the final output, or to correct eventually for errors introduced by the automated methods. Difficulties of automated techniques to localise abnormality call for additional visual and detailed examination of the image data and the anatomical structures. Given the high amount of image data, the frequency of acquisition and demand for interactive tools, user input in practice is not only time consuming but also subject to significant operator bias which can affect the statistical significance of the obtained results, particularly for longitudinal studies. Ideally, the method developed therefore needs to ensure the amount of user input is kept to the minimum.

The three issues described above represent the core technical motivation of this thesis, *i.e.*, developing an automatic framework for shape-based image analysis which can effectively incorporate prior knowledge, is resistant to image artefacts and involves minimal user interaction. In order to illustrate the technical details associated with the proposed techniques and demonstrate their potential clinical value, we will use cardiovascular shape analysis with MRI as the exemplar throughout this thesis. Due to the prevalence of cardiovascular diseases and the increasing clinical utility of MRI for

screening and early diagnosis, the use of shape analysis for cardiovascular MRI is of great importance and there is abundant literature addressing this topic. This generally requires serial examination of dynamic 3D models, which currently is still limited to labour intensive manual delineation. This has become one of the major bottlenecks of realising the full clinical potential of MRI, despite recent advances in hardware design and imaging sequence development. In practice, inherent anatomical and imaging difficulties associated with cardiovascular MRI still make the task a challenging one.

In terms of appearance, the outer wall borders of cardiac and arterial structures are generally displayed with weak/faint edges that are surrounded by fat. The presence of confusing neighbouring features, respiratory and cardiac motion, as well as blood flow, introduces additional difficulties. The quest for identifying early image biomarkers means the shape variation involved is usually subtle and local, which requires the automatic methods to be accurate and to take into account the available wealth of geometrical information. Furthermore, the evolving MRI sequence design means the quality of image features and their associated artefact are often site-, subject-, and sequence-specific.

This thesis is aimed at challenging medical image applications similar to cardiovascular MR. The work presented is based on the well-established approach for studying anatomical shapes based on landmark data. Several shape variables can be derived and while landmark coordinates are extensively used in the existing literature, this thesis represents a first extensive exploration of Inter-Landmark Descriptors (ILDs) in shape-based analysis of medical images. Unlike point coordinates which describe absolute position, these shape variables represent relative configuration of landmarks in the shape. Through explicit invariance to pose parameters and decomposition of the global shape constraints, the aim of this work is to propose a new framework that addresses some of the key limitations of existing methods such that the three challenges mentioned above are tackled to allow for more robust and detailed analysis of cardiovascular morphology.

1.2 Technical Motivations

A detailed study of anatomical morphology requires effective methods for shape description, modelling, extraction and analysis. Amongst existing techniques, the use of landmark data is a well established approach due to its ability to simplify the geometry of interest through a collection of landmark points defined at biologically or geometrically meaningful locations [1]. Shape descriptors and statistical modelling techniques are then used to study relative landmark configurations and incorporate suitable prior knowledge into the computational framework.

For general purpose modelling, the use of landmark coordinates as shape variables is a commonly adopted approach. Their use in biological shape analysis was originally complicated by lack of invariance to pose parameters. The emergence of shape superimposition methods [2], which attempt to eliminate the effect of similarity transformations, opened a range of new alternatives. In medical image analysis, coordinates enable easy manipulation of the shape vectors in the image space. They also facilitate statistical analysis for capturing intrinsic shape variabilities. However, the application of such methods to cardiac image analysis is faced with two difficulties.

First, the performance of such techniques depends heavily on the quality of the initial shape superimposition which is known to vary depending on the configuration of the landmarks involved [3]. The estimation of pose parameters can be easily affected when a small number of landmarks carry a significant proportion of the shape variation. These deviations can be caused by misplaced landmarks in the image (*e.g.*, due to image artefact or adjacent image features that are not associated with target anatomy), as well as genuine localised shape variations (*e.g.*, regional contractile abnormality of the ventricle).

The second issue is related to the nature of the prior knowledge that can be captured by conventional methods. One of the early motivations behind the direct use of landmark coordinates is their ability to describe the complete spatial arrangement of the landmarks within a unified model [4]. To this end, the application of superimposition and multivariate statistics can produce a reduced set of variables that summarises the variability induced by the larger number of landmarks. The global nature of the derived shape

parameters is beneficial for imposing constraints on unseen shapes as well as for detecting shape abnormalities. This, however, does not bode well for tasks that require constraints on individual landmarks as opposed to the entire shape, *e.g.*, for landmark search in new images or for local abnormality analysis.

Amongst existing techniques based on landmark coordinates and multivariate statistics, the Active Shape Model (ASM) [5] is widely used in medical image analysis and it represents the basic framework for the work presented in this thesis. The technique is well established for its ability to capture morphological variations across subjects and over time. The derived model can be used as a deformable template and fitted iteratively to new image data. The global nature of the model, however, prohibits its reliable initialisation and as a result, user interaction is often required. Furthermore, the geometrical constraints cannot be used to influence each individual landmark during edge point search. Instead, they are imposed at the end of each ASM iteration to obtain a valid instance from the identified features.

The sensitivity of shape alignment is even more problematic in the case of ASM. In the presence of missing, confusing or noisy image structures, the feature point search often results in misplaced points (outliers). This can violate the Gaussian distribution of the residuals (a common assumption used in ASM), thus affecting the subsequent pose and shape parameter estimation. The same problem arises when ASM parameters are used for regional abnormality analysis, as local variation can significantly affect the shape alignment process and subsequent statistical analysis.

In this thesis, we aim to use ILDs for addressing some of the key limitations of current techniques based on landmark coordinates and multivariate statistics. The use of ILDs has many advantages. First of all, unlike normal coordinates, they are invariant to a group of similarity transformations, which is beneficial when pose parameters are either unknown or difficult to be estimated accurately. Secondly, they provide a practical means of decomposing global shape alignment from local shape analysis, thus enhancing the overall consistency and robustness of shape analysis. Finally, by effective modelling of suitable inter-landmark relationships, relevant correlations between different parts of the shape can be captured and subsequently used for identifying shape inconsistencies.

1.3 Overview of the Thesis

Following a brief introduction of the key technical motivation of the thesis in this chapter, a detailed survey of statistical shape modelling techniques based on landmark coordinates and multivariate statistics will be provided in Chapter 2. The main part of the chapter is focussed on the ASM technique and issues concerning the training set, shape alignment, model construction, point correspondence and feature point search are discussed. The main purpose of this chapter is to highlight the relative merit and potential pitfalls of existing techniques, and therefore justifies the use of ILDs as the basis for shape-based image analysis.

In Chapter 3, the most common ILDs including linear distances, ratios, angular measurements and barycentic coordinates are introduced. This is then followed by describing the key properties of ILDs and the statistical tools used for modelling normal inter-landmark variables. This includes a description of univariate tolerance intervals, as well as multivariate tolerance regions. Examples results are provided to illustrate the practical use of ILDs, their statistical properties and their main attributes.

After the introductory chapters, Chapter 4 formulates the first methodology of the thesis, which is aimed at building relaxed yet robust geometrical constraints by using inter-landmark relationships. For this purpose, inter-landmark conditional probabilities are introduced and landmark prediction regions are derived. Furthermore, statistical-based search regions are proposed to replace the conventional normal search profiles in ASM during feature point search. An optimal feature point search based on inter-landmark constraints and the A* algorithm is developed for identifying the optimal set of target boundary points. The prediction regions are also used for automatic initialisation of ASMs. The validation of the proposed algorithm is carried out with both 2D and 3D MR segmentation of left ventricular epi-cardial borders of varying complexities.

The second part of the methodological development of the thesis is described in Chapter 5. The aim of this chapter is to localise inconsistent landmarks or outliers based on the analysis of ILDs. To this end, a global alignment invariant outlier detection algorithm is proposed. Considering the fact that ILDs are associated with more than one point, an

iterative procedure is used to identify inconsistent feature points. The proposed method involves the use of inter-landmark distance ratio as an invariant shape metric. Statistical tolerance intervals are estimated from the training set for identifying extreme ILDs. The technique also involves the propagation of geometrical knowledge gathered from the invariant descriptors during successive iterations for robust feature point detection. This limits the presence of outliers and improves the convergence of the segmentation process. The method is applied to carotid bifurcation and left ventricular datasets with detailed performance comparison to existing ASM approaches. A detailed simulation study for outlier identification is an important part of the chapter.

In Chapter 6, the landmark localisation scheme is extended for regional contractile analysis based on cardiac MRI. Specifically, an analysis framework is described for globally invariant identification of myocardial wall motion abnormality. To this end, a multi-dimensional ILD is introduced for representing spatio-temporal changes of the landmarks over the entire cardiac cycle. This is then followed by estimating normal contractility properties of the myocardium, from which both geometrical and dynamic anomalies are used to highlight localised lesions. The method is validated with a relatively large population of cardiac cine datasets that include both normal subjects and patients with varying levels of regional contractile abnormalities.

Finally, Chapter 7 concludes the dissertation by providing a detailed discussion of the techniques presented, their technical merits and potential drawbacks. It also lists potential future directions based on ILDs. Figure 1.1 provides a schematic diagram summarising the main steps involved in the traditional ASM methods and the proposed framework based on ILDs, in which key improvements to the analysis workflow are highlighted.

In summary, the main contributions of the thesis include:

- Theoretical investigation and algorithm development of ILDs for shape-based medical image analysis;
- Formulation of partial and invariant geometrical constraints for landmark search;

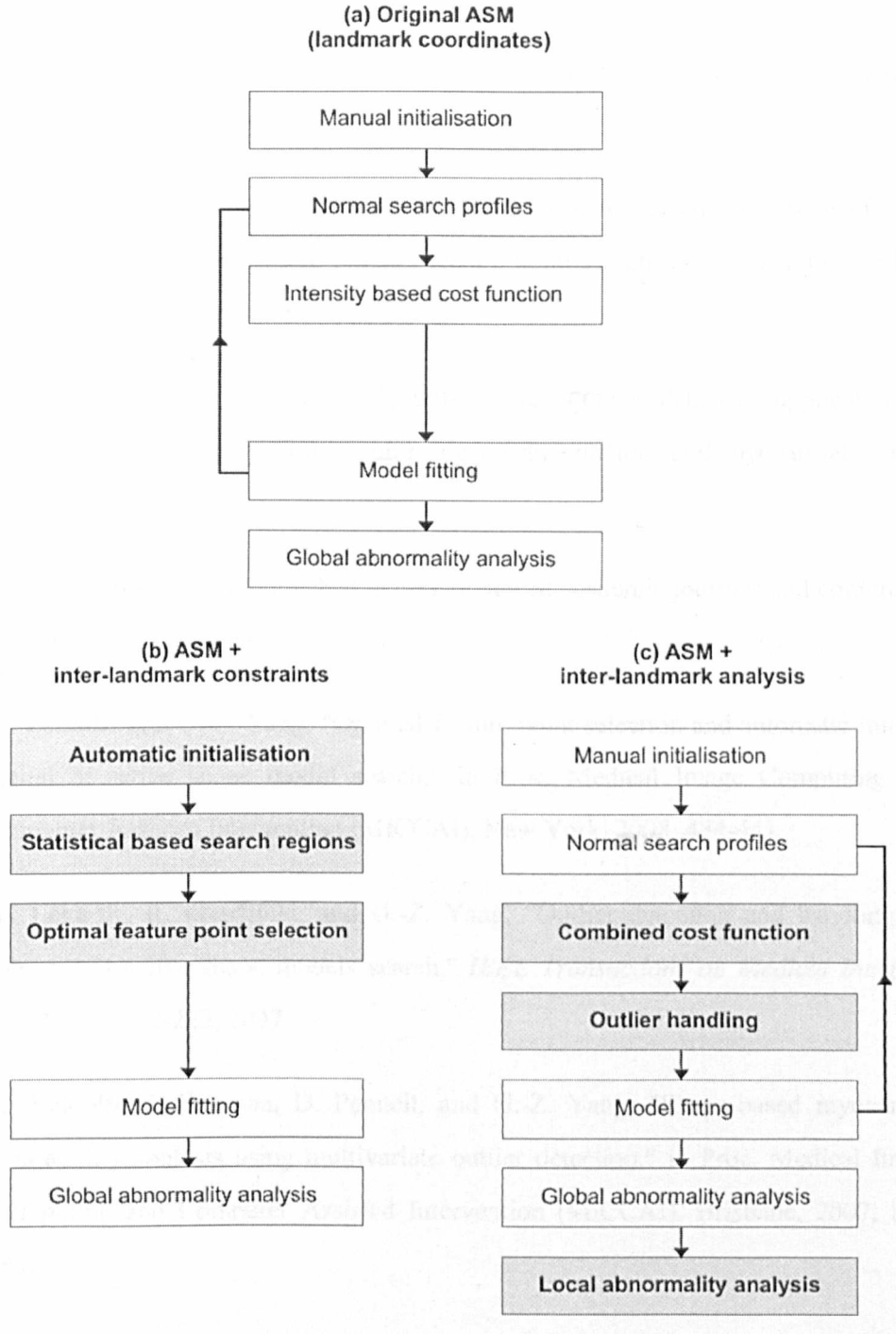

Figure 1.1 Schematic diagram summarising the key steps involved in the traditional ASM methods and the proposed framework based on ILDs. The landmark constraints permit a non iterative search due to the automatic initialisation and optimal feature point search introduced. By using inter-landmark analysis, outlier handling and local abnormality detection can be consistently performed.

- Development of an invariant landmark analysis algorithm for inconsistent landmark localisation;

- Incorporation of the above methodologies for addressing current limitations of ASM including shape initialisation, optimal feature point search, outlier handling and localisation of shape and motion anomalies;

- Validation of the proposed methods with concrete clinical data with applications to left ventricular segmentation, carotid artery segmentation, and myocardial motion analysis.

Most parts of this thesis are published in peer-reviewed academic journals and conference proceedings, which include:

- **K. Lekadir** and G.-Z. Yang, "Optimal feature point selection and automatic initialisation in active shape model search," in Proc. Medical Image Computing and Computer Assisted Intervention (MICCAI), New York, 2008, 434-441.

- **K. Lekadir,** R. Merrifield, and G.-Z. Yang, "Outlier detection and handling for robust 3-D active shape models search," *IEEE Transactions on Medical Imaging*, vol. 26, pp. 212-222, 2007.

- **K. Lekadir,** N. Keenan, D. Pennell, and G.-Z. Yang, "Shape-based myocardial contractility analysis using multivariate outlier detection," in Proc. Medical Image Computing and Computer Assisted Intervention (MICCAI), Brisbane, 2007, 834-841.

- **K. Lekadir**, R. Merrifield, and G.-Z. Yang, "Robust MR segmentation of the left ventricle using an outlier handling based active shape models," in Proc. Society for Cardiovascular Magnetic Resonance (SCMR), Roma, 2007.

- **K. Lekadir** and G.-Z. Yang, "Carotid artery segmentation using an outlier immune 3D active shape models framework," in Proc. Medical Image Computing and Computer Assisted Intervention (MICCAI), Copenhagen, 2006, 620-627.

- **K. Lekadir**, R. Merrifield, N. Keenan, D. Pennell, and G.-Z. Yang, "Robust image segmentation through outlier handling: application to automatic plaque burden assessment," in International Society of Magnetic Resonance in Medicine (ISMRM), Seattle, 2006.

- **K. Lekadir**, D. Elson *et al.*, "Tissue characterisation using dimensionality reduction and fluorescence imaging," in Proc. Medical Image Computing and Computer Assisted Intervention (MICCAI), Copenhagen, 2006, 586-593.

2

Statistical Shape Modelling

2.1 Introduction

For medical image computing, shape segmentation and modelling with incorporation of prior knowledge is a well developed research topic. Many techniques exist in the literature, including intensity-based [6-10] and atlas-guided [11-14] techniques. For the study of anatomical shapes, deformable models have enjoyed considerable interest since their original introduction by Kass *et al.* [15]. The method requires a pre-defined mechanism to model and control the shapes of interest, with the aim of recovering the anatomical structures of interest by iteratively deforming a shape instance under combined appearance and geometric criteria.

Generally, the geometry of the deformable models is formulated in a way such that it permits broad shape coverage with many degrees of freedom. Therefore, the approach is particularly suitable for biological shapes with large variabilities. The main strength of the technique is that it incorporates intuitive *physical* constraints such as continuity and bending energy of the contour and presents the problem in a mathematically sound formulation. The optimisation process attempts to minimise an energy function that balances the internal and external forces. In this model, external forces are usually derived from the image to drive the curve or surface towards the desired boundaries of interest, whereas internal forces are computed from within the curve or surface to keep it properly regularised throughout the deformation.

Early deformable models were defined using parametric curves such as splines. More elaborated formulations have been derived over the years. Deformable M-reps [16,17], for example, is a technique through which geometrical information is described by a collection of elements defined in medial terms. Parametric models, on the other hand, use outline-based representation of the shape [18] to constraint the image search. The idea is to subdivide the boundary into a set of elements, each represented by a limited number of measurable coefficients calculated by fitting a curve model based on Fourier decomposition [19], spherical harmonics [20] or spherical wavelets [21]. Another method that can be considered as implicit deformable models are level sets [22], which represent the shape of interest as a level set of scalar functions.

Shape-based segmentation based on deformable models offers a natural paradigm to impose high-level geometrical constraints. Early approaches used physically motivated constraints to ensure generality and robustness. However, its flexibility often leads to solutions that are unrestricted to specific applications. To address this problem, statistically motivated constraints were introduced which incorporate statistical geometrical priors about the class of shapes of interest. Among these techniques, the Active Shape Model (ASM), developed by Cootes *et al.* [5] is based on landmark representation of the shapes. The derived statistical model of shape is applied as prior knowledge to guide and reinforce the segmentation process. It can also be used for describing normal shape distribution and detecting outliers.

Shape representation through landmarks, such as adopted by the ASM framework, is now a well established approach for the study of biological shapes. It aims to approximate essential elements of the shape by using individual measurements. In this case, a finite set of points are defined along the boundaries of interest at biologically or geometrically meaningful locations. The landmark generation is usually subjective and domain specific, but some general rules and automatic methods can help optimising the procedure. First, the landmarks are chosen such that they correspond to the position of particular local features based on biological or geometrical criteria. The landmarks need to be homologous, *i.e.*, they are comparable within all instances of the shapes. Also, they must be topologically consistent and therefore should not alter their positions relative to other

landmarks. In this regard, establishing satisfactory point correspondence between datasets is critical to the application of ASM.

Once the landmarks are suitably defined around the boundaries, a shape descriptor vector that numerically characterises the configuration of the landmarks is required to allow further manipulation of the model. Several possible shape variables exist for landmark data, such as coordinates and Inter-Landmark Descriptors (ILDs), each with its own attributes and limitations. Ideally, the shape variables should be easy to manipulate and allow faithful reconstruction of the original morphology, *i.e.*, a reverse mapping exists between the descriptor vector and the shape.

Thus far, the use of point coordinates as variables for statistical shape modelling is the most popular choice, since they enable natural characterisation of the landmarks in the image space. The ASM is based on this approach and in this chapter, we will present a review of techniques related to statistical shape modelling. First, the construction of the statistical model of shape is described, including shape alignment and point correspondence. Emphasis is then placed on the image search procedure and the main steps involved. Finally, the main theoretical and practical limitations of the technique that have motivated this thesis are discussed at the end of the chapter.

2.2 Statistical Shape Models

The Point Distribution Model (PDM) [23] developed by Cootes *et al.* is well recognised for its ability to capture variation of landmarks across individuals and time, making it particularly suitable for the study of anatomical structures. Based on landmark coordinates and multivariate statistics, the technique builds a parametric model which approximates the multidimensional shape space using a multivariate Gaussian distribution. This is achieved through the extraction of a mean shape, main patterns of variation and their corresponding allowable limits. PDMs are widely used as a deformable template to fit the model to unseen shapes in new images through the Active Shape Model (ASM) [5]. Figure 2.1 provides a schematic diagram summarising the main steps involved in PDM construction, which are detailed in next sections.

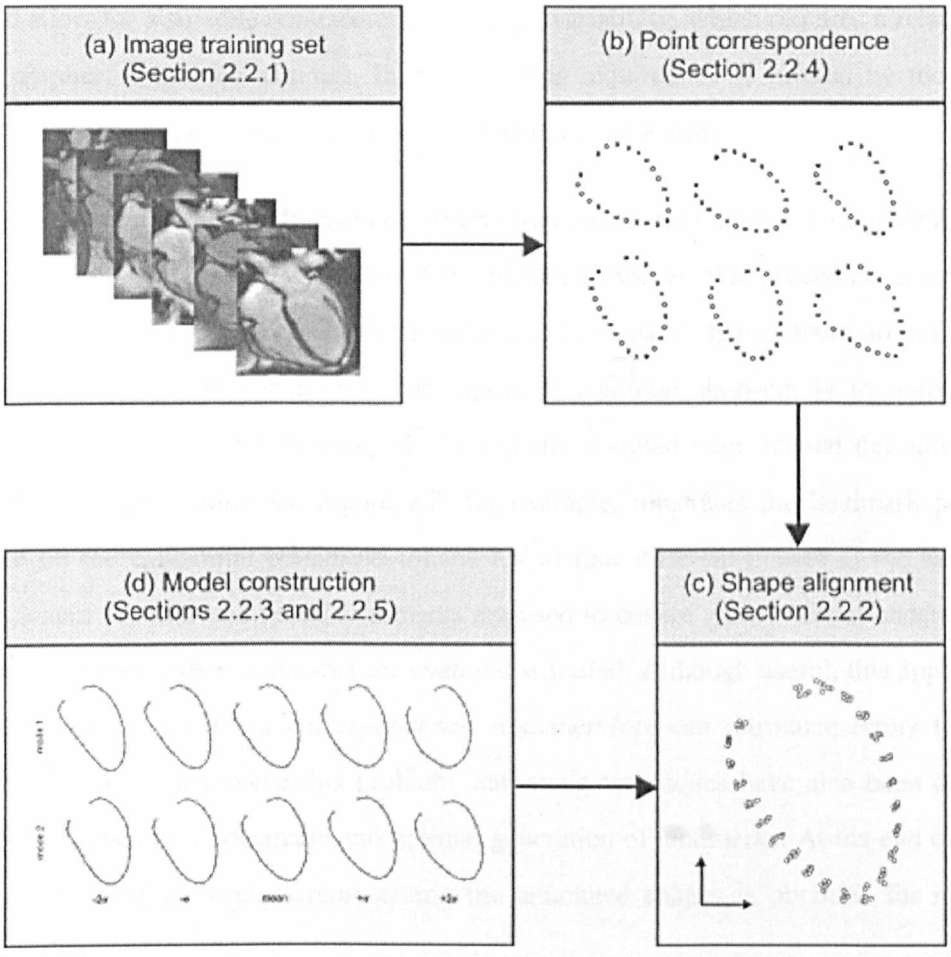

Figure 2.1 The main steps involved in PDM construction, including image training set collection (a), automatic landmark generation with correspondence (b), shape alignment within a common coordinate system (c), and extraction of main shape variations (d).

2.2.1 Training Set Preparation

In this thesis, the shapes are represented by n labelled landmarks and their coordinates by $(\mathrm{x}_i = (x_i, y_i, z_i)^T$ for $1 \le i \le n)$. The corresponding descriptor vector $\mathbf{x}$ therefore consists of a concatenation of the point coordinates represented as follows:

$$\mathrm{x} = (x_1, y_1, z_1, \ldots, x_i, y_i, z_i, \ldots, x_n, y_n, z_n)^T. \tag{2-1}$$

Preparation of the training sample is a critical stage for obtaining a statistical shape model with adequate quality. To this end, two fundamental issues need to be addressed, *i.e.*, training sample selection and boundary annotation. Firstly, the choice of training datasets

should allow for a suitable representation of shape variability, which requires a relatively large number of training samples. In practice, this requirement is limited by the data available and the time consuming process of boundary annotation.

In medical imaging, the involvement of expert observers in defining the training dataset is important for maintaining the quality of the model. However, this procedure is tedious due to the large number of landmarks involved and for many shapes, there are no clear geometrical features to consistently rely upon. A common short-cut is to uniformly distribute the landmark points along the boundaries coupled with manual definition of several distinctive landmarks. Figure 2.2, for example, illustrates the landmark points defined on the epi-cardial boundaries of the LV at four different phases of the cardiac cycle, where valvular and apical landmarks are used to ensure global correspondence of the shape whereas other landmarks are evenly distributed. Although useful, this approach cannot guarantee landmark correspondence, and therefore can introduce errors to the model created. To overcome this problem, automatic techniques have also been developed to achieve more systematic and optimal generation of landmarks. At the end of this process, a set of N vectors representing the annotated shapes is obtained for model construction.

2.2.2 Shape Alignment

In medical imaging, since shapes are generally recorded in separate and arbitrary coordinate systems, it is necessary to align all these shapes to a common frame of reference before subsequent modelling can be performed. To this end, a process called shape superimposition needs to be applied [2]. It essentially moves the available shapes until the best possible alignment is obtained within a common coordinate system. To achieve this, several approaches exist, each minimising a particular measure of shape similarity. The subsequent shape analysis results depend on the choice of the method and its performance with the given landmark configurations. The most popular shape superimposition technique is the Procrustes analysis [2].

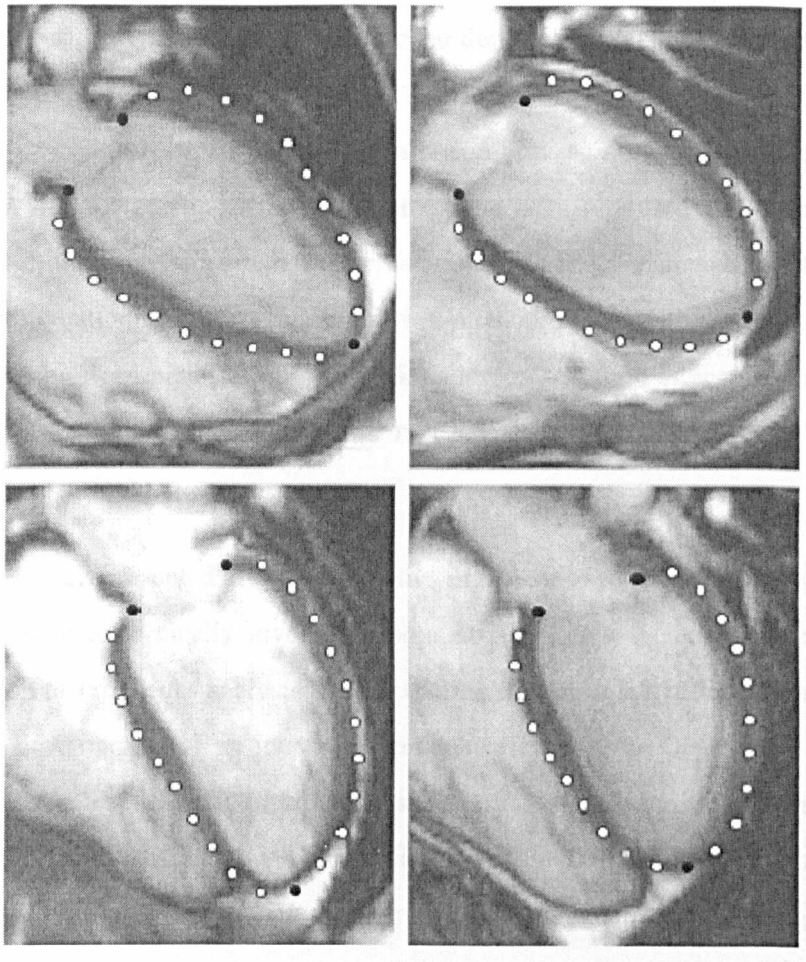

Figure 2.2 Four images from a cardiac MR cine sequence showing the epi-cardial borders and their associated landmark annotations. The black dots correspond to the valvular and apical landmarks, which are used as the reference for global correspondence.

Given two shape vectors $\mathbf{x}^{(1)}$ and $\mathbf{x}^{(2)}$, superimposition is carried out by fixing the first shape and applying translation, rotation and scaling to the second such that the two shapes are fully matched according to some predefined alignment criteria. The remaining landmark differences between the fitted and observed vectors of coordinates indicate the magnitude of shape dissimilarity. For Procrustes analysis, this is minimised in the least squares sense, *i.e.*, for similarity transformation T (incorporating translation, rotation and scaling parameters) applied to $\mathbf{x}^{(2)}$, the sum of landmark differences between $\mathbf{x}^{(1)}$ and $\mathbf{x}^{(2)}$ is minimised by:

$$\left(\mathbf{x}^{(1)} - T\left[\mathbf{x}^{(2)}\right]\right)^{T}\left(\mathbf{x}^{(1)} - T\left[\mathbf{x}^{(2)}\right]\right). \tag{2-2}$$

Thus far, several analytical solutions have been derived to enable efficient shape alignment based on the Procrustes method [24-27]. This is the basis for several shape-based image analysis methods, since it is generic and conforms to normality assumptions used in statistical shape modelling. Other measures have been proposed as an alternative to Equation (2-2) by using nonparametric formulations ([28,29]) for improved robustness. It is also worth mentioning other superimposition methods, such as the two-point registration approach by Bookstein [30], through which a representation of shape is obtained by fixing the position of the same baseline in each shape and adjusting the remaining coordinates accordingly.

Procrustes analysis presented above enables the alignment of two shapes. Statistical shape modelling, however, typically involves a population of $N > 2$ shapes. The analytical generalisation of Procrustes analysis to a population of shapes is a difficult problem. This has led the development of an iterative approach referred to as Generalised Procrustes Analysis (GPA). With this algorithm, the estimation of translation, rotation and scaling parameters is achieved through successive iterations until the sum of landmark differences from all examples to the mean shape is minimised, indicating a good alignment.

To initialise the algorithm, it is required to choose one of the available shapes as the starting mean shape. Each shape is then aligned to the current estimation of the mean shape based on a solution of Equation (2-2). The mean shape is then updated and the procedure continues until convergence. To eliminate poorly defined solutions, constraints are imposed on the mean shape, for example by moving its centroid to the origin of the common coordinate system and by normalising its size to a unit scale. Figure 2.3 shows an example of shape alignment achieved through least squares Procrustes analysis based on six epi-cardial contours. After superimposition, the landmark differences between different shape instances are minimised, as evident from the clusters forming around the landmarks.

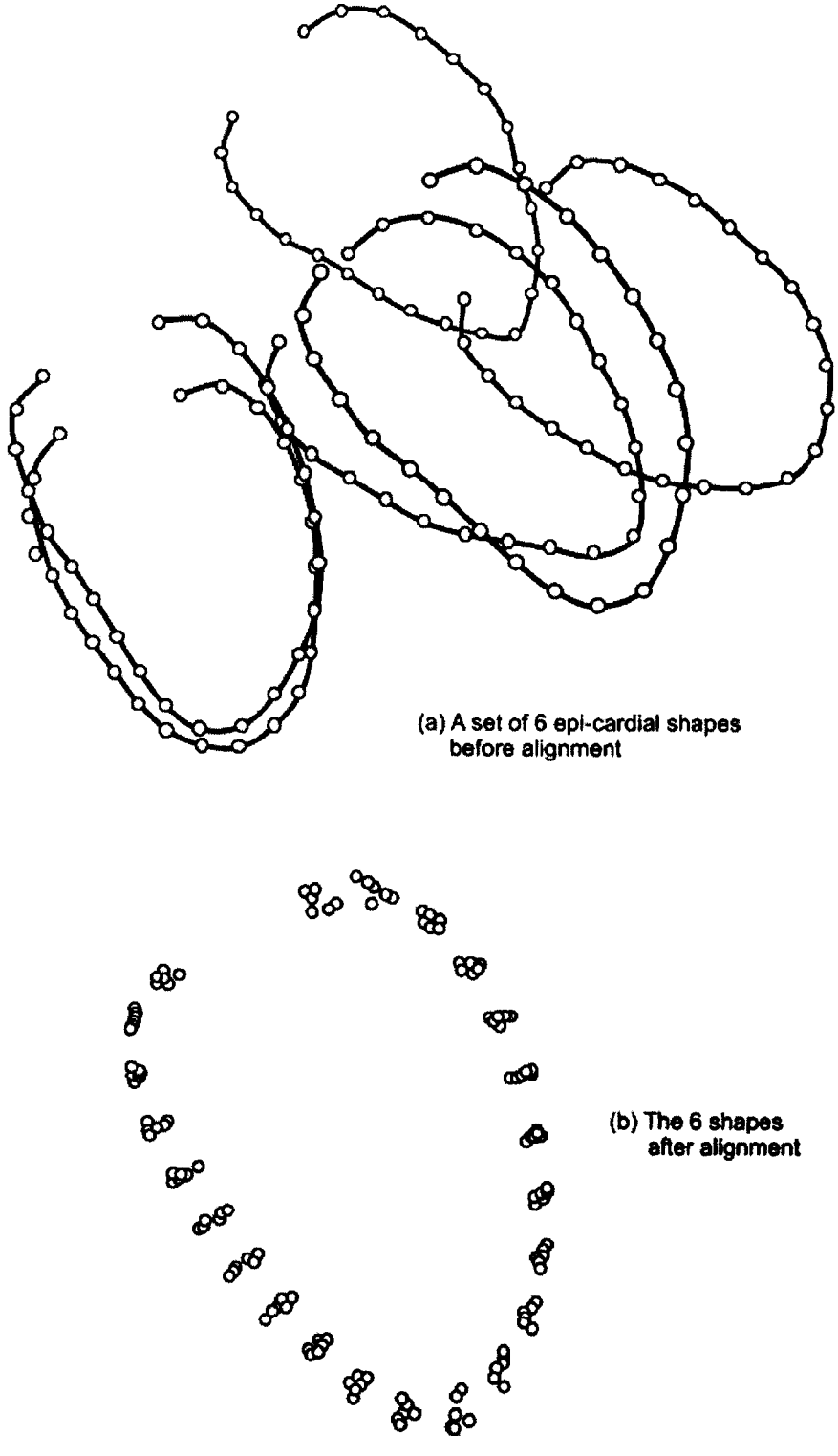

Figure 2.3 Shape superimposition of six epi-cardial contours by using the general Procrustes analysis. The shape vectors of all instances are expressed within the same coordinate system, by minimising differences in size, orientation and position.

2.2.3 Model Construction

Once the N training shapes are collected, annotated and aligned, statistical analysis on the landmark locations is performed in order to build a statistical model of the shapes. Specifically, the PDM method extracts an average shape, principal modes of variations and the limits of allowable instances. Mathematically, the average shape is obtained by simply calculating a mean shape vector, *i.e.*,

$$\bar{\mathbf{x}} = \frac{1}{N}\sum_{j=1}^{N}\mathbf{x}^{(j)} \tag{2-3}$$

where $\mathbf{x}^{(j)}$ denotes the j^{th} shape vector in the training sample. The main axes of variation, denoted by the matrix $\mathbf{P}$, are the basis vectors of a new coordinate system obtained through Principal Component Analysis (PCA), which identifies a linear orthogonal transformation highlighting the directions of maximal variance. To achieve this, the covariance matrix is calculated as follows:

$$\mathbf{S}_{\mathbf{x}} = \frac{1}{N}\sum_{j=1}^{N}\left(\mathbf{x}^{(j)} - \bar{\mathbf{x}}\right)\left(\mathbf{x}^{(j)} - \bar{\mathbf{x}}\right)^{T} \tag{2-4}$$

The extracted eigenvalues are sorted in a descending order and only the eigenvectors corresponding to the t most significant eigenvalues are selected ($t < N$). The value of t is defined so that the chosen principal modes can explain a given proportion (*e.g.* 99%) of the variance exhibited in the training set. At this stage, a linear model which can generate new instances of the shape can be obtained as follows:

$$\mathbf{x} = \bar{\mathbf{x}} + \mathbf{P}\mathbf{b} \tag{2-5}$$

where $\mathbf{b}$ is the vector of shape parameter, which weights the contribution of each mode of variation. It is important to ensure that each new shape generated by the PDM using Equation (2-5) is a valid instance, *i.e.*, it belongs to the same class of shapes as the training set. This is achieved by constraining the shape parameters $\mathbf{b}$ to vary only within suitable limits (the allowable shape domain, denoted here as D). Under the assumption of multivariate Gaussian distribution, D can be obtained by imposing hard limits on each of the weights within a number of standard deviations (*e.g.* $|b_j| < 3\sqrt{\lambda_j}$ for $1 \le j \le t$). More

accurate limits can be imposed such that the Mahalanobis distance of the new shape to the mean is less than a predefined threshold U_D, *i.e.*,

$$D = \left\{ \mathbf{b} \in \mathbb{R}^t \mid \sum_{j=1}^{t} \frac{b_j^2}{\lambda_j} \leq U_D \right\}. \tag{2-6}$$

Figure 2.4 illustrates the principal modes of variation obtained from the 2D epi-cardial datasets shown in Figure 2.2. It can be seen that the first mode describes the shortening of the LV whereas the second corresponds to axial rotation.

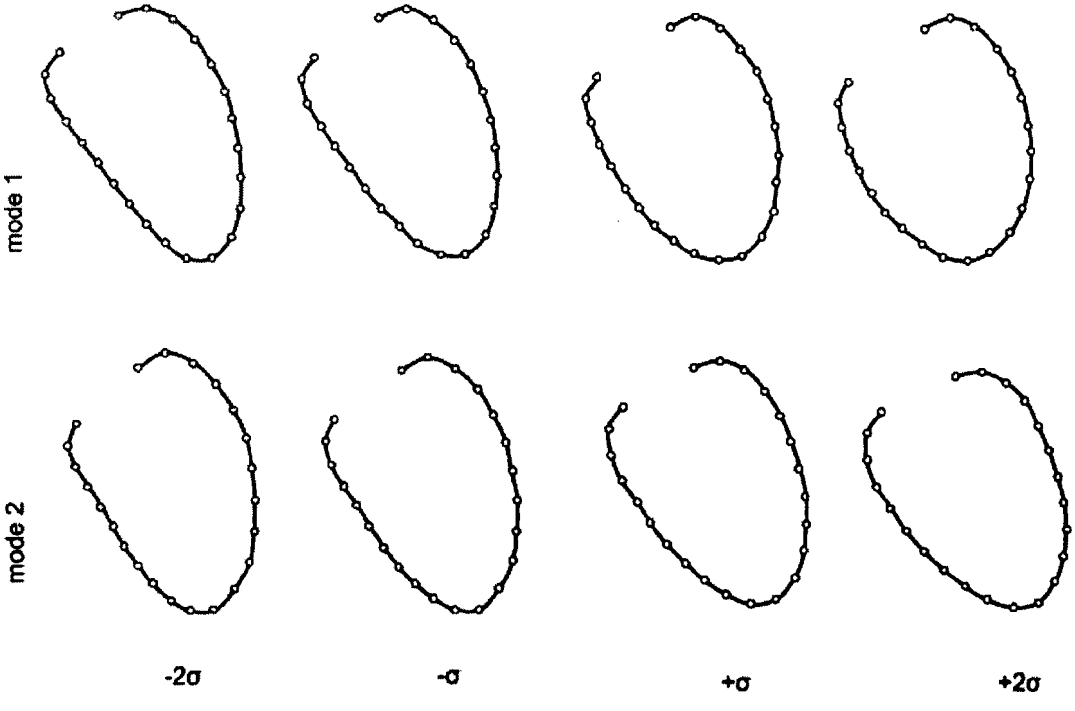

Figure 2.4 Global shape variations as captured by application of PCA to a training set of aligned epi-cardial boundaries. It can be seen that the first mode describes a change in diameter while the second corresponds to axial variation.

2.2.4 Point Correspondence

The quality of the statistical shape model constructed through PDMs can be evaluated through three main properties, *i.e.*, model compactness (ability to represent shape variability using as few parameters as possible), model generalisation (ability to represent

new shapes of the same class), and model specificity (ability to represent only valid instances of the class). One of the key issues for obtaining satisfactory PDM properties is the establishment of point correspondences to ensure meaningful associations exist between equivalent points in all training shapes. Careful manual annotation of each individual landmark is a difficult and time consuming task. In practice, even expert annotation often involves significant intra- and inter-observer variabilities, as not all landmark points correspond to clearly identifiable geometrical features, especially in 3D and 4D cases.

For these reasons, many techniques have been developed for establishing optimal point correspondence. The most popular approach is to find a parameterisation that optimises a predefined function, for example, the use of total variance [31] or an objective function based on the determinant of the covariance matrix [32]. The use of Minimum Description Length (MDL) of the training set was proposed by Davies *et al.* [33]. It has been shown that the method can derive statistical models with good compactness, generalisation and specificity. Curvature information was also incorporated into the MDL optimisation by Thodberg and Olafsdottir [34].

A more recent approach by Horkaew and Yang [35] based on harmonic embedding and the MDL criterion was developed to model shapes with more complex topologies. A conformal harmonic map and tensor product B-splines were used to create a multi-resolution representation of the surfaces. Re-parameterisation was then achieved by using hierarchical piecewise bilinear maps in a coarse-to-fine manner. Criteria based on surface conformality were used to simultaneously identify the intrinsic global correspondence of the training data. Figure 2.5 demonstrates the result achieved by the method in capturing intrinsic shape variability of the LV. With accurate point correspondence, the first mode of variation captures the contraction of the ventricle, corresponding well to physiological behaviour of the normal heart.

Thus far, several alternative approaches to optimisation-based point correspondence have also been developed. Non-rigid shape matching has been proposed to identify homologous landmarks between shapes [36,37]. Other techniques are based on an analysis of local geometry [38,39] for localising a set of geometrical features that can be used for

pair-wise point correspondence. Image-based techniques relying on non-rigid registration have also been proposed [40,41]. Instead of finding optimal positions of the landmarks, the method uses the B-spline deformation control grid of the image volumes as a means of establishing point correspondence and extracting principle modes of variation.

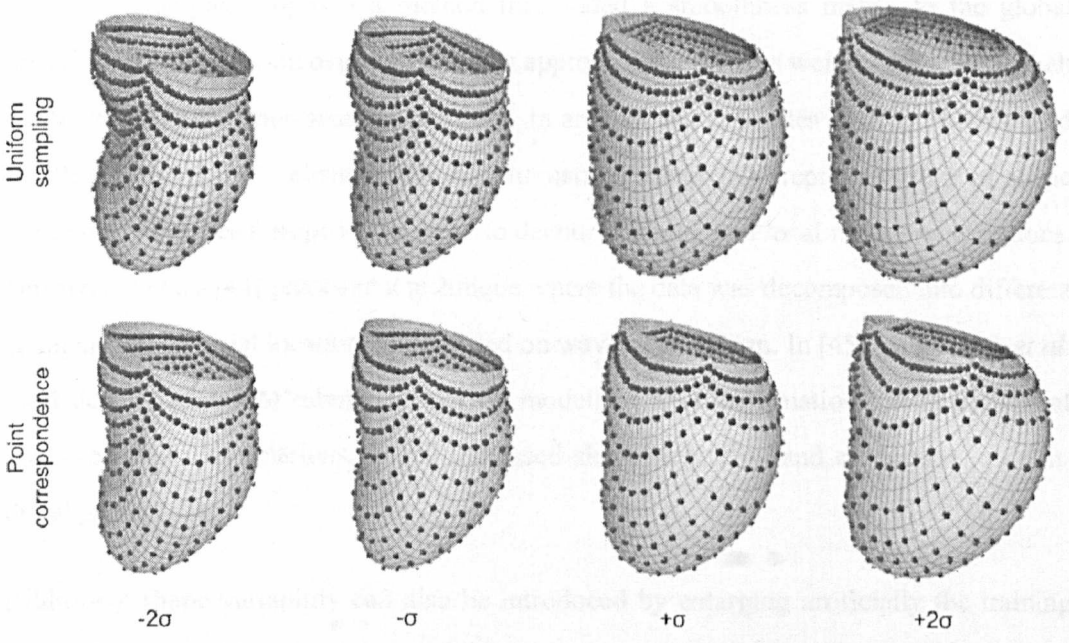

Figure 2.5 Comparison of the variation captured by PDMs constructed through conformal harmonic embedding [35]. With optimal point correspondence, the first mode captures the contraction of the ventricle corresponding closely to the physical behaviour of the human heart.

2.2.5 Alternative Constructions

For statistical shape modelling, the quality of the model also depends on the availability of training samples, which in practice may be only limited to a small subset of shapes. Increasing the size of the training set is not always possible due to practical constraints on data collection and manual annotation. Since the maximum number of eigenvectors that can be used to represent any shape is at most equal to the number of training samples minus one, the PDM may not be able to describe all fine details of the shapes with limited training data. As a result, the statistical model may be restrictive in terms of capturing

intrinsic shape variabilities. To address this problem, several methods have been proposed to introduce additional modes of variation to the model.

The first approach is to use combined models, where the statistical model of shape is coupled with a physical-based model to allow for smooth local variation. Wang and Staib [42], for example, proposed a method that added a smoothness matrix to the global covariance eigen-decomposition. With this approach, the relative weight assigned to each model needs to be determined empirically. In another work, Cootes *et al.* [43] combined the PDM with a finite element model. Alternative hierarchical representations of shape variability have been proposed in order to decouple global and local modes of variations. Davatzikos *et al.* [44] proposed a technique where the data was decomposed into different frequency and spatial location bands based on wavelet transform. In [45], de Bruijne *et al.* used decomposition of tubular shapes by modelling axel deformation independently of cross-sectional deformations, which increased shape flexibility and adaptation to cylindrical geometries.

Additional shape variability can also be introduced by enlarging artificially the training set. In the work of Loetjoenen *et al.* [46], each shape from the training set was deformed at several randomly selected point locations by applying non-rigid spherical scaling and movement. It is unclear, however, whether the resultant variations with this approach are realistic for practical applications. Shen and Davatzikos [47] proposed an alternative method for training set enlargement. It identifies shapes with low spatial variability or high confidence, which are then spatially scaled to increase the variance. Finally, several techniques have been developed to handle more complex types of variability. To account for non-linearity, Romdhani *et al.* [48] constructed a PDM based on kernel PCA, while Sozou *et al.* developed a technique based on polynomial regression [49]. In another work by Cootes *et al.* [50], shape variation was modelled using a Gaussian mixture model.

2.3 Active Shape Models (ASM)

In the above sections, we have presented PDM construction for statistical shape modelling, which provides a linear representation of the average shape, main variation and

allowable domain. The aim of the ASM is to use the model derived to guide and reinforce the image search process for shape segmentation.

Given a new image $\mathbf{I}$, the aim of ASM search is to find a shape $\mathbf{x}$ that is valid according to the variability captured by PDM and its boundary points conform to some predefined appearance properties, *e.g.*, strong edge gradients or high curvature points such as corners. More specifically, the technique attempts to estimate the pose transformation T (position of the mean shape in the image domain) and shape parameter $\mathbf{b}$ (specific geometry of the target structure) that minimise cost function d_1 describing the degree of fit to the underlying image features, *i.e.*,

$$\mathbf{x} = \underset{\mathbf{x} \in \mathbf{I}}{\operatorname{argmin}} \sum_{i=1}^{n} d_1(\mathbf{x}_i) \tag{2-7}$$

$$\text{where } \mathbf{x} = T[\bar{\mathbf{x}} + \mathbf{P}\mathbf{b}] \text{ and } \mathbf{b} \in D. \tag{2-8}$$

Equation (2-7) describes an appearance-based cost function to minimise (sum of grey-level matches $d_1(\mathbf{x}_i)$ for each individual landmark point p_i), whereas Equation (2-8) corresponds to the optimisation constraint from the statistical model. Given the size of the image, as well as the number of pose and shape parameters to estimate, concurrent optimisation of the objective function can be computationally prohibitive. The solution adopted by Cootes *et al.* in their ASM formulation is to decouple the intensity-based objective function in Equation (2-7) and the global geometric constraints in Equation (2-8) in an iterative procedure by alternating between feature point search and model fitting. The method starts with an estimated starting pose and shape (*initialisation*) and at each iteration, feature points located close to the contours are identified (*feature point search*), a valid shape is then instantiated (*model fitting*).

Figure 2.6 shows a detailed illustration of the key stages involved in the ASM framework for shape extraction. In this example, a long MR image is used to localise the epi-cardial boundary. To this end, a manual initialisation is first carried out by placing the mean epi-cardial shape near the target boundary (a). Subsequently, the search for feature points is performed by using profiles perpendicular to the current contour, as shown in (b). In (c), the identified set of feature points is displayed, including a number of outliers due to the presence of image inhomogeneities in the vicinity of the epi-cardial border. Finally, the

model fitting stage is applied in (d) to ensure consistency of the output with respect to the statistical model of shape. It can be seen that the resulted instance at first iteration (displayed in (d)) is an improvement to the initial shape. Further improvements in boundary localisation can be achieved by application of additional search iterations. Figures (e) and (f) show intermediate results for the iterations 10 and 20, respectively.

2.3.1 Feature Point Search

Feature point search is critical to the success of ASM. At each iteration, the aim of the procedure is to find for each model point a better position in a local neighbourhood. For this purpose, adequate modelling of intensity distribution near the boundary is required. A method suggested by Cootes *et al.* [51] is to model statistically during the training stage the intensity or gradient distribution along profiles that are perpendicular to the shape boundary. An average intensity profile $\bar{\mathbf{g}}$ and a covariance matrix $\mathbf{S}_{\mathbf{g}}$ describing the appearance variation can then calculated. At the segmentation stage, a localised search perpendicular to each landmark is carried out. Under the normality assumption, a suitable cost function to evaluate is the Mahalanobis distance to the mean profile described as follows:

$$d_1(\hat{\mathbf{x}}_i) = \left(\mathbf{g}(\hat{\mathbf{x}}_i) - \bar{\mathbf{g}}\right)^T \mathbf{S}_{\mathbf{g}}^{-1} \left(\mathbf{g}(\hat{\mathbf{x}}_i) - \bar{\mathbf{g}}\right). \tag{2-9}$$

The best candidate within each normal search profile is chosen and the set of detected feature points that optimise the objective function in Equation (2-7) are used at the current iteration. The geometric constraint in (2-8) is generally not satisfied at this stage, and this is the aim of model fitting to be described in the next section.

In recent years, more robust local boundary modelling and evaluation techniques have been proposed in order to improve its resistance to noise and handle non-linearity. One possible approach developed by Van Ginneken consists of calculating local image features combined with classification of false and true positives using a k nearest neighbours procedure [52]. Jiao *et al.* [53] suggested the use of Gabor wavelet features based on the hypothesis that the magnitude and phase of Gabor features contained rich information about local geometries. The well-known Haar wavelet features were used in the ASM search by Cristinacce and Cootes [54].

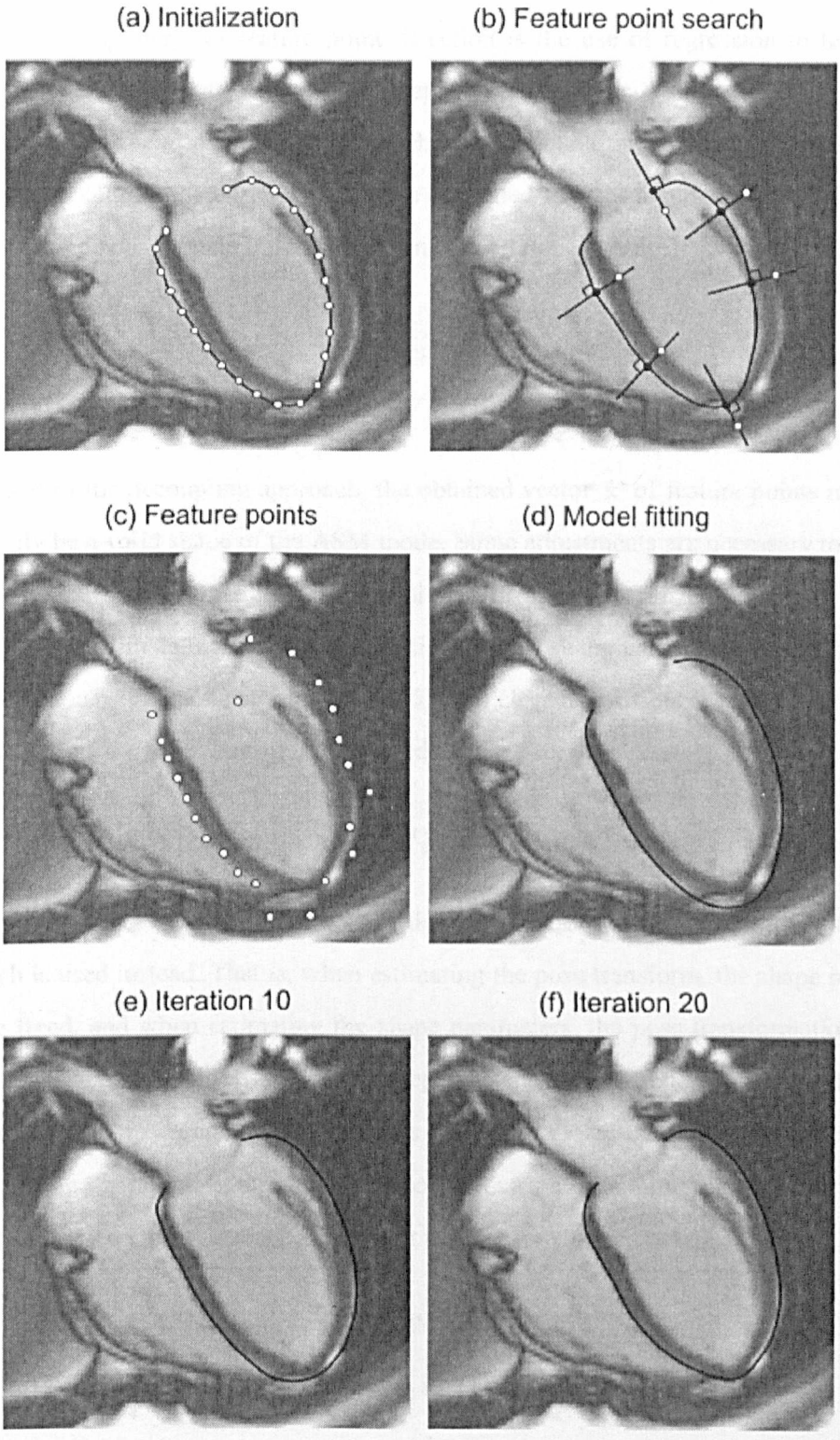

Figure 2.6 Illustration of the main stages of the ASM search for a long-axis cardiac MR dataset. The mean shape is placed near the target structure for initialisation (a). Normal search profiles are used for feature point search as shown in (b). The iterative procedure ((d)-(f)) enables continuous improvement of the boundary until convergence.

An alternative strategy for feature point detection is the use of regression to learn the relationship between local neighbourhood appearance and the displacement to the true feature location. With this method, no search profile around the current point is required as only the profile at the current position is evaluated to infer a suitable point displacement. Such methods include the use of canonical correlation analysis [54] or GentleBoost [55] as the basis regression predictors.

2.3.2 Model Fitting

As a result of the decoupling approach, the obtained vector $\hat{\mathbf{x}}$ of feature points may not necessarily be a valid shape of the ASM mode. Some adjustments are necessary to obtain a shape $\mathbf{x}$ that satisfies the global constraint in (2-8). Specifically, the aim of model fitting is to re-estimate the pose transformation T and shape parameter $\mathbf{b}$ such that the obtained shape using the linear model in (2-5) is as close as possible to the feature points. To achieve this, the following sum of squared distances can be minimised:

$$\left(T^{-1}[\hat{\mathbf{x}}] - (\bar{\mathbf{x}} + \mathbf{P}\mathbf{b})\right)^T \left(T^{-1}[\hat{\mathbf{x}}] - (\bar{\mathbf{x}} + \mathbf{P}\mathbf{b})\right). \tag{2-10}$$

In general, a direct analytical solution to this equation is not feasible and an iterative approach is used instead. That is, when estimating the pose transform, the shape parameters are fixed, and when estimating the shape parameters, the pose transformation from the previous iteration is used. This process repeats iteratively until no change is noticed in the values of the pose and shape parameters. It can be shown that the amount of adjustment on shape parameters $d\mathbf{b}(t)$ at iteration t can be determined by minimising the difference between the suggested adjustment and the constrained parameter update, *i.e.*,:

$$\begin{aligned} d\mathbf{b} &= \arg\min_{d\mathbf{b}}[(d\mathbf{x} - \mathbf{P}\,d\mathbf{b})\,\mathbf{W}\,(d\mathbf{x} - \mathbf{P}\,d\mathbf{b})^T] \\ \text{where } d\mathbf{x}(t+1) &= T(t)^{-1}[\hat{\mathbf{x}}] - (\bar{\mathbf{x}} + \mathbf{P}\mathbf{b}(t)) \end{aligned} \tag{2-11}$$

and $\mathbf{W}$ is a diagonal weighting matrix which defines the amount of contribution from different control points. Using linear algebra, the minimisation is equivalent to:

$$\begin{aligned}\left(\mathbf{P}^T\mathbf{W}\mathbf{P}\right)d\mathbf{b} &= \mathbf{P}^T\mathbf{W}d\mathbf{x} \\ \text{or } d\mathbf{b} &= \mathbf{P}^T d\mathbf{x} \text{ if } \mathbf{W} = \mathbf{I}_{3n}.\end{aligned} \tag{2-12}$$

The resulting shape is then used as the initialisation for the next iteration. The ASM search procedure terminates when no significant change is produced between successive iterations, suggesting an optimal shape is found given the available image features and prior knowledge.

2.3.3 Alternative ASMs

Over the years, several modifications to the standard ASM formulation have been developed. One popular alternative is the multi-resolution approach introduced by Cootes *et al.* [56]. One of the issues associated with ASM search is the choice of the size of the normal search profiles. A small normal search profile may not have enough coverage to capture valid image features depending on the initialisation. A large search profile, on the other hand, may result in many undesirable features, thus causing the search to be trapped in suboptimal local minima. To overcome this difficulty, a coarse-to-fine multi-resolution representation of the image data is obtained through convolution with Gaussian kernels of different scales. The step size of the search and intensity profiles is doubled from one resolution to the next. At coarse resolutions, the relatively long search profiles allow for a suitable range capture, while the large Gaussian kernels ensure the removal of noise and small confusing structures in the image. This allows the model to identify a good approximate location of the target shape based on consistent image structures. At finer resolutions, the search resorts to small search profiles for more detailed boundary localisation. Generally, this approach increases the accuracy, as well as the speed of search.

Other methods developed use geometric constraints to limit the presence of outliers. Behiels *et al.* [57], for example, added a smoothness constraint during feature point search to ensure the consistency of neighbouring points. In their spatio-temporal ASM extension, Hamarneh and Gustavsson [58] used dynamic programming to minimise a cost function such that large temporal changes in landmark position are prohibited. In [59], Cootes and Taylor considered more than one feature point for each landmark and selected

the combination that was most consistent with the shape model based on a set of intermediate PDMs.

Another popular modification to the ASM search is the introduction of an intermediate stage between feature point search and model fitting, during which outliers are identified and removed. For example, Duta and Sonka used variance induced by each landmark for outlier detection but acknowledged difficulties when handling multiple outliers [60]. Li and Chutatape used thresholding of the landmark residuals by relying on satisfactory superimposition [61], which could in practice be affected by increasing number of outliers. The method by Rogers and Graham, on the other hand, is based on robust estimators to assign varying weights to the feature points using a weighted least squares approach [62] and improvement is reported for up-to 20% misplaced features. For all these techniques, the handling of clustered outliers (*i.e.*, localised within the same region of the boundary) can be problematic. Alternatively, interactive user input can be used during the process to correct for potential errors [63].

For practical applications, it may be desirable to adapt ASMs to specific applications and to take into account domain-specific geometrical and appearance information. De Bruijne *et al.* [45], for example, developed an ASM formulation for tubular-like structures and applied the method to aortic aneurysm segmentation. Heinmann *et al.* [64] combined the ASM and a deformable mesh approach for liver segmentation. Zhao *et al.* [65] used a 3D partitioned active shape model for brain segmentation by subdividing the meshes into a group of titles each modelled independently. The global shape consistency is controlled by curves connecting the title hyperspaces. Seise *et al.* [66] proposed a method that catered for inconsistent bifurcations and loops appeared in bone and knee segmentation. Van Assen *et al.* developed a 3D ASM technique for cardiac segmentation using sparse long-axis MRI [67] and an improved ASM search based on fuzzy inference [68]. More recently, Casero and Noble [69] proposed to adapt ASMs for structures with cyclic dynamics, such as the heart.

2.4 Current ASM Issues

Despite its several merits, the capabilities of the ASM in challenging applications to reach the requirements described in Chapter 1 of this thesis, *i.e.*, minimisation of user interaction, incorporation of effective prior knowledge, and resistance to imaging artefacts, are complicated by inherent limitations of methods based on coordinates and multivariate statistics. In the follow sections, we will detail some of these problems and explain how they affect the overall performance of the algorithm.

2.4.1 Shape Alignment and Global Constraints

Procrustes analysis opened a wide range of opportunities for biological shape analysis, It is widely used since the cost function is generic, suitable for the study of variation within a family of shapes and can be efficiently solved analytically. In image analysis, shape alignment enables easy manipulation of coordinates in the image space and provides well-recognised statistical properties [70]. Despite considerable results, the application of landmark coordinates to medical image analysis is faced with two limitations in challenging applications.

First, the performance of existing techniques based on coordinates depends heavily on the quality of the shape alignment, which is known to vary depending on the configuration of the landmarks involved [3]. The estimation of pose parameters can be particularly affected when a small number of landmarks carry a significant proportion of the shape difference, causing landmark residuals to deviate from normality. Such a situation, however, is common in medical imaging due to the inevitable presence of image inhomogeneities (noisy, confusing or missing structures), as well as to local shape inconsistencies (regional abnormality). The use of invariant ILDs would be more desirable when the pose parameters are unknown or otherwise difficult to estimate accurately.

The second issue is related to the nature of the prior knowledge captured by conventional methods. One of the early motivations behind the use of coordinates is their ability to describe the complete spatial arrangement of landmarks within a unified model [4]. To this end, the application of superimposition and multivariate statistics (*e.g.*, PCA) can

produce a reduced set of variables that summarise the variability induced by the larger number of landmarks. The global nature of the shape parameters derived is beneficial in image analysis to constrain unseen shapes as well as to detect diseased patients. However, their use is complicated in computational tasks that require constraints on the individual landmarks, such as for feature point search and local abnormality detection. In this thesis, the proposed solution is to use a set of individual ILDs to model partial geometrical constraints and achieve an implicit decomposition of the global shape model.

2.4.2 Implications to ASMs

The application of the global constraints in ASMs is essentially concerned with the position of the instance in the shape space, rather than the position of each individual landmark in the image. As a result, feature point search in its current formulation is entirely unconstrained, based on simple normal profiles which do not incorporate any prior knowledge about the landmark positions. As a consequence, outliers may be generated under challenging imaging conditions, affecting the subsequent shape alignment due to the non-Gaussian residual distribution introduced [3]. Furthermore, the model fitting in such a situation may generate a shape that is geometrically plausible but is not supported by the underlying image evidence.

The application of the global shape constraints is also problematic for ASM initialisation due to the high-dimensionality of the task and the size of the search space. In practice, however, an ASM requires suitable starting estimates to ensure that the search process does not get trapped in an undesirable local minimum. Generally, this is achieved based on manual interaction, through which the user places the mean shape close to the target structures. Although this is often satisfactory, the setting can be limited for shapes with complex variability or geometry and becomes impractical for volumetric or spatio-temporal initialisation. Some exhaustive search methods can be adapted for ASM initialisation, such as based on genetic algorithms [71], modified Hough transform [72], and particle filtering [73]. These approaches, however, are inherently time consuming, with typical computational times in minutes in the 3D case (*e.g.* [64]). Consequently,

manual initialisation remains the standard approach despite its subjective and tedious nature.

In addition to their segmentation purpose, PDMs are widely used for abnormality analysis based on the shape instantiation. In the presence of regional abnormality, however, the shape alignment is by definition affected and therefore the obtained shape parameters may not be accurate. Furthermore, each shape coefficient relates a large number of landmarks, which makes the method only applicable for the identification of diseased subjects, rather than the localisation of abnormality in the shape. Recently, this limitation of PCA-based methods for identifying localised abnormality has received considerable research interest. For example, sparse-PCA methods have been developed to enable the extraction of more localised shape parameters [74]. Independent component analysis has also been investigated for more localised cardiac motion analysis [75]. Furthermore, PCA coupled with orthomax rotations has been proposed for classification of wall motion abnormalities [76]. All these methods use coordinates as shape variables and remain affected by the varying performance of shape alignment. In this thesis, the use of inter-landmark descriptors is proposed for invariant and localised abnormality analysis.

2.5 Discussion and Conclusions

In this chapter, statistical shape modelling based on landmark coordinates and multivariate statistics is presented. A summary of some of the main technical approaches involved in each step of the modelling process is provided in Table 2.1. The essence of the statistical shape modelling scheme is to build statistically-motivated constraints to ensure more accurate and biologically meaningful results. In general, the framework is based on landmark coordinates since they allow simple characterisation and manipulation of the shapes in Euclidean space. For this method to work effectively, adequate shape alignment of the shape vectors is required due to a lack of invariance of the shape to the pose of the model. This is traditionally carried out using Procrustes analysis, which is well suited to normally distributed shapes. The PDM construction, on the other hand, is typically carried out through the application of PCA, which defines the principal modes of variation of all the shapes considered. PDMs are widely used as deformable models for shape

instantiation and segmentation. In this chapter, we have reviewed different ASM approaches developed over the years for improving the quality of the original ASM in terms of model construction and feature localisation.

Despite its wide range of applications, current ASM methods are not without limitations. This is mainly due to their reliance on landmark coordinates and multivariate statistics. Firstly, the sensitivity of the shape alignment is problematic in the presence of image artefacts and confusing anatomical features. The same problem arises for regional abnormality analysis. Secondly, the global nature of the PDM shape parameters prohibits the use of landmark constraints to help with initialisation and improve feature point identification.

To address the limitations highlighted above, we will introduce in the next chapters a new approach based on ILDs for the study of anatomic shapes. The major motivation behind this approach is to achieve invariance to pose parameter estimation and to make sure the proposed method is suitable for both global and regional shape analysis. Both theoretical analysis and detailed algorithm development are provided, which address specific issues related to it integration with the current ASM framework. Key issues considered include automatic initialisation, optimal feature point search, outlier handling and local abnormality analysis.

Table 2.1 A summary of the major developments in statistical shape modelling.

PDMs	Developments
First model based on inter-landmark distances and PCA	Cootes *et al.* [77]
PDMs based on coordinates	Cootes *et al.* [23]
Combined models	FEM/PDM [43], elastic model/PDM [42]
Hierarchical PDMs	Wavelets coefficients [44], axial/radial [45]
Artificial enlargement of training set	Adaptive focus PDM [47], local deformation [46]
Non-linear PDMs	Kernel PCA [48], mixture models [50]
Specific PDM extensions	Tubular structures [45], cyclic dynamics [69]
ASMs	**Developments**
Standard ASM formulation	Cootes *et al.* [5]
Multi-resolution ASMs	Cootes *et al.* [56]
Use of neighbouring constraints	Smoothness constraint [57], dynamic programming [78]
Outlier detection	Variance analysis [60], Robust estimators [62]
Automatic initialisation	Genetic algorithm [71], Hough transform [72]
Specific ASM extensions	Partitioned-ASM [65], sparse-ASM [67]
PCA-based grey-level profiles	Mahalanobis distance [51], cross correlation [57]
Non-linear optimal local features	Moments of histograms [52]
Wavelet-based feature point search	[53], Haar wavelet [54]
Regression-based feature point search	Canonical correlation [55], GentleBoost [54]

3

Inter-Landmark Descriptors

3.1 Introduction

In the previous chapter, statistical shape modelling based on landmark coordinates and multivariate statistics is introduced. The statistical models derived can capture intrinsic shape variabilities from a family of similar anatomical structures. From the review in the last chapter, it is evident that although major research effort for statistical shape modelling has been directed to its practical applications, limited work has been conducted for the construction of invariant landmark descriptors.

The choice of landmark descriptors for biological shape analysis has seen many important developments and debates over the years. In particular, three main approaches for the study of landmark data have received significant attention. They include coordinate-based landmark definition, deformation grids and Inter-Landmark Descriptors (ILDs). In the last chapter, we have provided a detailed overview of the coordinate-based approach. Although simple to manipulate, the use of landmark coordinates for biological shape analysis is made possible by the introduction of superimposition techniques that minimise the effect of pose estimation. An earlier approach developed by Thompson [79] describes shapes implicitly in terms of deformation fields required to transform one to the other. In practice, there are many ways in which the warping operation can be achieved between shapes. The well-known Thin Plate Spline (TPS) introduced by Bookstein [80], for example, attempts to minimise the bending energy required to match the floating shape to

the template shape. With this approach, unless the material properties are specifically incorporated, the output is dependent on the choice of the deformation model used.

Unlike coordinates and deformation grids, ILDs can achieve invariance of the model to non-shape based parameters such as the initial pose of the model. As a result, the shape analysis is independent of pre-processing procedures. This unique feature makes the technique particularly useful for a range of applications including shape analysis in zoology and archaeology [81,82], particularly for shape classification. Due to the large number of shape variables involved, however, the method is difficult to manipulate and it is also lack of an explicit one-to-one mapping between the shape and descriptors. For these reasons, ILDs have so far not been used in image analysis applications.

In this chapter, we will present some of the key features of ILD and propose several algorithms and statistical implementations that enable the effective use of the ILDs. In particular, issues related to invariance to non-shape parameters, implicit encoding of correlations between different parts of the shape, and shape parameter decomposition will be addressed. Before presenting the proposed methodologies and algorithms, we will first introduce in this chapter the basic features of ILDs for shape analysis. These include linear distances, ratios, angular measurements and barycentric coordinates. The statistical tools used in this work to model normal inter-landmark variables and decompose the global shape constraints are then presented. In particular, statistical intervals that permit the differentiation between valid and extreme ILDs are discussed in detail. At the end of the chapter, example results by applying the ILD-based shape analysis are illustrated to help demonstrate the main features of ILDs and their ability for morphological modelling and dynamic analysis.

3.2 Inter-Landmark Descriptors

Unlike landmark coordinates which encode absolute positions, ILDs are numerical variables that represent relative landmark configuration of the shape. Historically, this approach pre-dates the use of landmark coordinates as shape variables mainly due to their invariance properties, and therefore are often referred to as traditional methods [1]. They

have been used extensively in shape comparison and classification [1], as well as for measuring physical properties of shapes (*e.g.*, length, width, relative size of structures) [82]. To this end, the basic assumption made is that corresponding measures between two similar shapes have close values. Similarly, for a population of shapes that are normally distributed, it is assumed that each ILD follows approximately a univariate Gaussian distribution.

The calculation of ILDs typically involves a small number of landmarks. Popular examples include distances between two landmarks, ratios of inter-landmark distances, and angular measurements. Figure 3.1 illustrates how these measures are represented for an example MR dataset of the carotid artery and ventricles.

3.2.1 Linear Distances

Inter-landmark distances are the most popular choice amongst ILDs. They are invariant to translation and rotation, and therefore are particularly suited for studying biological development processes where scale is an important factor. When applied to cardiac assessment, this can be used to quantify ventricular dilatation associated with chronic hear failure for example. When absolute scale is not important, appropriate methods for correction for size differences are required.

Amongst notable works based on linear distances, a well known statistician called C.R. Rao formalised the use of linear distances for shape comparison. In [83], Lele *et al.* developed a method named Euclidean Distance Matrix Analysis through which average shape and covariance are estimated. Additionally, the first version of the PDM by Cootes *et al.* was developed using inter-landmark distances [77], but it required an expensive iterative scheme to map the set of distances to the image space. This technique, unlike the work presented in this thesis, was not applied for a segmentation or diagnosis purpose and was later replaced by the current ASM formulation based on landmark coordinates incorporating shape alignment. In all these methods, standard multivariate statistical methods are used, resulting in a global based approach.

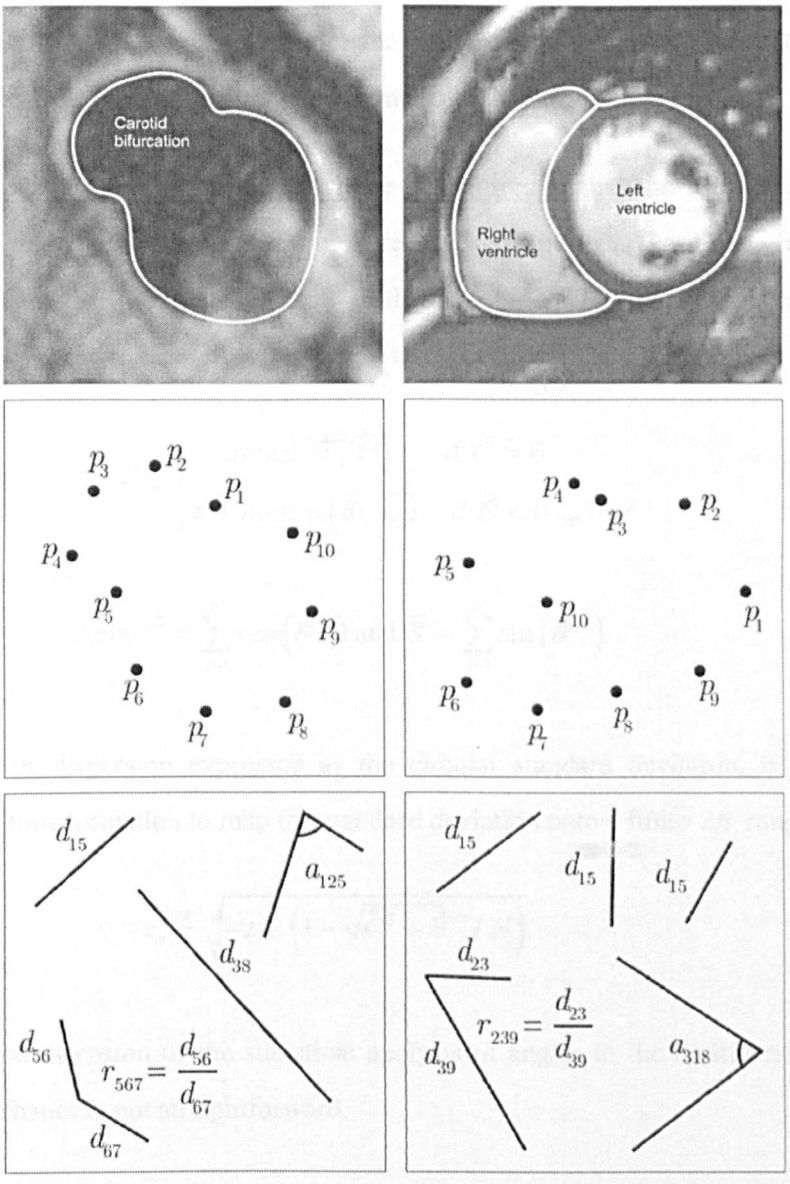

Figure 3.1 Illustrations of ILDs (distances, ratios and angles) as extracted from carotid and ventricular datasets.

3.2.2 Angular Measurements

Angles are shape variables that provide complete invariance to scaling, rotation and translation. As shape descriptors, they have been used extensively for shape similarity and in planar geometrical analysis, particularly for anatomical shape classification. For example, Rao and Suryawanshi [84] compared skulls from hominid fossils using angles

from a triangulation of landmarks. Since the three interior angles of a triangle sum to π, only two selected angles are used as shape variables.

The consequence of using angles as shape descriptors is that the use of conventional statistics is deficient since angular measurements are periodic variables. In this case, directional statistics [85] can be used as the basis for subsequent statistical analysis. Given N angular variables $\theta_1,\ldots,\theta_N$, a measure of the average value is given by:

$$\bar{\theta} = \begin{cases} \arctan\left(\bar{S}/\bar{C}\right) & \text{if } \bar{C} > 0 \\ \pi + \arctan\left(\bar{S}/\bar{C}\right) & \text{if } \bar{C} < 0 \end{cases} \tag{3-1}$$

$$\text{where } \bar{C} = \sum_{j=1}^{N} \cos\left(\theta^{(j)}\right) \text{ and } \bar{S} = \sum_{j=1}^{N} \sin\left(\theta^{(j)}\right). \tag{3-2}$$

A measure of dispersion expressed as the circular standard deviation, is given by a logarithmic transformation to map the standard deviation onto a finite 2π range, *i.e.*,

$$v_\theta = \sqrt{-2\ln\left(1 - \sqrt{\bar{C}^2 + \bar{S}^2}/N\right)}. \tag{3-3}$$

However, the extension of the statistical analysis of angles to the multivariate case and volumetric shapes is not straightforward.

3.2.3 Ratios of Distances

Ratios of inter-landmark distances are also fully invariant descriptors and have the advantage over angles in that they can be used in all dimensions and are easier to calculate and manipulate. The calculation involves Euclidean distances related to three landmarks, *i.e.*, for a triplet of points p_i, p_j, p_k:

$$r_{ijk} = \frac{\|p_i - p_j\|}{\|p_j - p_k\|}. \tag{3-4}$$

Working with ratios is therefore equivalent to manipulating a set of triangles. Because the similarity or dissimilarity between two triangles can be assessed by testing equality between all corresponding ratios, such ILD is appropriate for shape comparison and dissimilarity analysis. From a theoretical point of view, it is shown that it would be more preferable to consider the logarithm of the ratios as shape variables [86] because this simplifies to a linear combination of the distance measures whilst maintaining the normality assumption ($\log(x/y) = \log(x) - \log(y)$). For this reason, ratios of inter-landmark distances are used in Chapter 5 to develop a fully invariant method for outlier detection and correction in ASMs.

3.2.4 Barycentric Coordinates

Barycentric coordinates can be considered as a type of ILD, since they are related to a small number of points and provide information about the relative rather than absolute position of the points [87]. More specifically, they describe the position of a point within a local coordinate system formed by a set of three landmarks by using an affine combination of their coordinates. Given three points p_i, p_j, p_k with their coordinates $\mathbf{x}_i, \mathbf{x}_j, \mathbf{x}_k$, and an arbitrary point p with coordinates $\mathbf{x}$, the scalars a_j, a_j, a_k are the barycentric coordinates of p with respect to p_i, p_j, p_k if:

$$\mathbf{x} = a_i\mathbf{x}_j + a_i\mathbf{x}_j + a_k\mathbf{x}_k \tag{3-5}$$

$$\text{and } a_i + a_j + a_k = 1. \tag{3-6}$$

The constraint in Equation (3-6) is imposed on the coefficients to allow for suitable invariance to a group of similarity transformations. Figure 3.2 provides a simple illustration of the barycentric coordinates. In (a) and (b), four points are plotted with respect to two distinct triangles using the same barycentric coordinates, showing relative as opposed to absolute description of the landmark positions. In (c), the sign of the coordinates with respect to the reference triangle is shown.

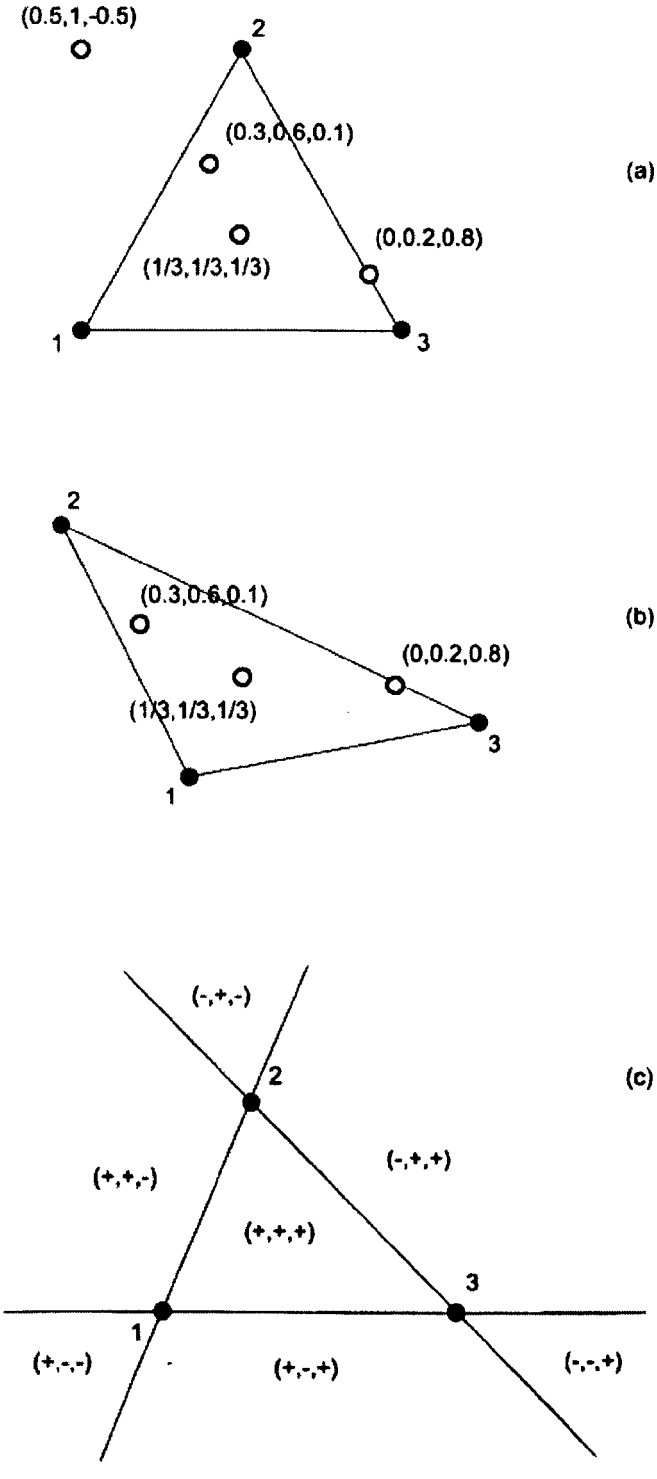

Figure 3.2 Example showing the properties of barycentric coordinates. In (a) and (b), four points are plotted with respect to two distinct triangles but with the same barycentric coordinates, showing a relative as opposed to an absolute description of landmark positions. In (c), only the sign of the coordinates with respect to the reference triangle is displayed.

Barycentric coordinates have attracted a range of applications in computational geometry and graphics. They include surface parameterisation [88] and interpolation [89], as well as dimensionality reduction [90]. Several methods also exist to generalise the barycentric coordinates to more than three landmarks and irregular polygons, such as in [91,92]. In Chapter 4, generalisation of the Barycentric coordinates based on a statistical formulation will be introduced for constructing partial geometrical constraints to enable prediction of landmark positions in the image space.

3.2.5 Properties of ILDs

According to the definition by Kendall [93], shape is all the geometrical information that remains when the effect of location, scale and rotational is removed. In medical imaging, for example, the position of the patient in the scanner should not affect the morphological and functional analysis of the images. With landmark coordinates and superimposition, the effects of translation, rotation and scaling are minimised but not completely removed. In statistics, the pose parameters can be referred to as nuisance variables, since they do not enter in the analysis and yet its effect must be accounted for.

In contrast, ILDs ensure explicit invariance to a group of similarity transformations. This is independent of any pre-processing procedure of the landmark data. In practice, several types of invariance can be obtained by adequate choice of the inter-landmark variables. For example, ratios are appropriate for fully invariant analysis, whereas inter-landmark distances incorporate scaling information, allowing both size- and shape-related analysis. The generalisation of barycentric coordinates to model partial geometrical constraints is invariant to translation, and therefore to the location of the anatomical structure within the image. As a result, ILDs can be applied when the pose parameters are unknown or difficult to be estimated. These properties of invariance of ILDs are essential in the work presented in this thesis.

In addition to shape invariance, two important benefits of shape-based image analysis can be derived by using ILDs. Firstly, unlike coordinates which characterise the position of a single point, relationships between different parts of the shape can be encoded by the inter-landmark variables. As a result, a single ILD can implicitly model correlations and

patterns of variation within a shape. This can be beneficial, for example, for identification of potential inconsistencies from individual variables, which is one of the goals of this thesis. This property is used in Chapter 6 for the assessment of myocardial motion abnormality. The correlation in contractility between different segments of the ventricle is modelled using spatio-temporal ILDs, enabling morphological and dynamic inconsistencies to be localised.

Furthermore, ILDs only involve a small number of landmarks and therefore can be used to decompose global shape constraints by appropriate modelling of individual variables. The aim is to gain some flexibility in the use of prior knowledge for shape analysis. While PDMs cannot support missing points since all landmarks need to be included in the shape parameters, the use of multiple ILDs independently can overcome such difficulties. More importantly, in the presence of geometrical inconsistencies associated with a few landmarks, not all global shape parameters are affected, which is not the case for coordinate based schemes. As a result, ILDs can have a good performance for the search and identification of individual landmarks. The cost of this flexibility due to decomposition is that high-level correlations between ILDs are not considered, which can cause some relaxation of the constraints on the landmarks. In practice, however, suitable analysis of multiple intersections between the ILD constraints can result in a reasonably good approximation of landmark constraints.

It should be noted, however, ILDs are not without their limitations. First, the lack of a direct one-to-one mapping between the descriptor vector and the original shape can complicate the manipulation of such variables in the image space. As a result, specific statistical and algorithmic implementation is required to select ILDs that are relevant to the analysis task. Another limitation is a significant increase in the number of variables involved in the computations (from $3n$ in the case of coordinates to $n(n-1)/2$ for two-point ILDs such as linear distances in 3D). This, however, is not an issue for this thesis since only ILDs of some statistical significance and geometrical interest are used. The selection of suitable sets of ILDs is reviewed in Section 3.3.4. There have been much debate regarding the statistical power for the estimation of mean shape and global covariance [70,83], which is considered as lower for ILDs compared to that of coordi-

nates. However, ILDs are used in this thesis for decomposing the global shape constraints and the statistical analysis is carried out on individual variables as shown in subsequent chapters of this thesis.

In summary, ILDs have interesting properties including global invariance and the ability to model inter-landmark correlations and decompose global shape constraints. The traditional limitations are overcome in this thesis by appropriate selection of inter-landmark variables, as well as by using novel algorithm design and statistical implementations developed in this thesis.

3.3 Statistical Analysis of ILDs

Traditionally, the point distribution model is based on a parametric model that relates all landmarks in the shape. In this thesis, the use of invariant ILDs calls for an alternative statistical implementation in order to enable the decomposition of global constraints. To this end, statistical intervals are presented in this section for describing individual descriptors and normal inter-landmark patterns at the training stage. Incorporated as prior knowledge, they enable effective statistical inference on new landmarks in input images, such as testing for consistency or performing prediction.

3.3.1 Univariate Tolerance Intervals

A tolerance interval for a measured quantity is a statistical interval within which, with some confidence, a specified proportion of a population falls [94] based on a representative sample S. In other words, the tolerance interval corresponds to the limits of acceptability within which a certain percentage of each individual measurement in the population is contained. Any value outside the tolerance intervals can be considered as extreme or invalid, suggesting some associated anomaly regarding the statistical process under investigation. Tolerance intervals have been widely used in statistical process control and manufacturing [95].

Because tolerance intervals are based on only a sample of the entire population, we cannot be 100% confident that the interval will contain the specified proportion. Thus there are two different proportions associated with the tolerance interval: a degree of confidence, and a percent coverage or content. Let F be the cumulative distribution function of a variable r, the corresponding statistical tolerance interval $T(S) = [r_L, r_U]$ is a two-sided tolerance interval with β-content and γ-confidence if:

$$P[F(r_U) - F(r_L) \geq \beta] = \gamma \tag{3-7}$$

This equation indicates that at least a proportion of the population β will lie within interval $[r_L, r_U]$ with confidence coefficient γ.

For this thesis, each variable is assumed to follow a Gaussian distribution, in which case it can be shown [96] that the statistical tolerance interval, *i.e.* the solution of Equation (3-7), can be calculated from the mean $\bar{r}$ and standard deviation s in the following form:

$$T(S) = [\bar{r} - k_2 s, \bar{r} + k_2 s] \tag{3-8}$$

where k_2 is the two-sided tolerance factor, which can be approximated by [97]:

$$k_2 = z_{(1-\beta)/2}\sqrt{\left(1 + \frac{1}{N}\right)\frac{N-1}{\chi^2_{\gamma,N-1}}} \tag{3-9}$$

where N is the sample size, $z_{(1-\beta)/2}$ is the upper $(1-\beta)/2$ quantile of the standard normal distribution and $\chi^2_{\gamma,N-1}$ is the lower γ quantile of the chi-squared distribution with $N-1$ degrees of freedom.

Alternatively, nonparametric tolerance intervals can be estimated, based on the smallest and largest observations [98], *i.e.*,

$$T(S) = [\min(S), \max(S)] \tag{3-10}$$

In this case, combinations of confidence and coverage coefficients that match the distribution-free tolerance interval can be calculated by using the following formula [99]:

$$\gamma = \sum_{k=0}^{N-2} \binom{N}{k} \beta^k (1-\beta)^{N-k} \tag{3-11}$$

3.3.2 Multivariate Tolerance Regions

A tolerance region is a generalisation of the tolerance interval for multivariate statistical processes. It is a region of the multidimensional space under investigation where there is a specified high probability (the confidence) that at least a specified proportion of the distribution (the coverage) is included. Mathematically, a tolerance region $R(S)$ for a given sample S of N observations $S = (\mathbf{v}_1, \ldots, \mathbf{v}_N)$ in the p dimensional space can be defined for given β-content and γ-confidence as follows [100]:

$$P\left[P\left[\mathbf{v} \in R(S) \mid S\right] \geq \beta\right] = \gamma \tag{3-12}$$

The requirement in Equation (3-12) is to guarantee with a confidence level γ that the proportion of population which $R(S)$ includes is greater than or equal to a predefined coverage coefficient β.

While the estimation for univariate tolerance intervals can be reduced to finding the lower and upper limits of acceptability, the multivariate case requires an alternative definition. Amongst existing approaches, the limits of the tolerance region can be defined in terms of a specified distance that depends on the multi-dimensional distribution from each observation to a reference value. Mathematically, given $\mathbf{v}$ a multivariate observation in a p dimensional space, a tolerance region R can be defined as follows:

$$R(S) = \{\mathbf{v} \in \mathbb{R}^p \mid d(\mathbf{v}, \mu, \Sigma) < L\} \tag{3-13}$$

where μ and Σ are the reference location and scale of the distribution, respectively, while d denotes the distance measure to the centre of the distribution and L a threshold that limits the size of the tolerance region, which depends on the confidence and coverage coefficients.

For a multivariate normal distribution, it was shown [101] that an appropriate distance measure for multivariate normal tolerance regions is the Mahalanobis distance, which measures a scaled distance to the centre of the distribution as follows:

$$d(\mathbf{v}) = (\mathbf{v} - \mu)^T \Sigma^{-1} (\mathbf{v} - \mu) \tag{3-14}$$

where the centre and scale can be approximated using the mean observation and the covariance matrix, respectively:

$$\bar{\mathbf{v}} = \frac{1}{N}\sum_{i=1}^{N} \mathbf{v}_i \text{ and } S_{\mathbf{v}} = \frac{1}{N-1}\sum_{i=1}^{N} (\mathbf{v}_i - \bar{\mathbf{v}})(\mathbf{v}_i - \bar{\mathbf{v}})^T. \tag{3-15}$$

With this definition, the tolerance region $R(S)$ is a hyper-ellipsoid (since the equi-probability hyper-surface of the multivariate normal distribution is a hyper-ellipsoid) which has the smallest volume amongst regions which include a proportion β of the population [100]. For the corresponding tolerance region limit L in Equation (3-13), it is shown that it can be estimated from the critical values of the chi-square distribution as [102]:

$$L = \chi^2_{p,(1-\beta)^{1/N}}. \tag{3-16}$$

Generally, in order to consider only the directions of meaningful variations, an eigen-decomposition of the covariance matrix can be applied as in PCA. By rejecting the $p - t$ noisy directions, the distance measure can be simplified to:

$$d(\mathbf{v}) = \sum_{i=1}^{t} \frac{[U_i(\mathbf{v} - \bar{\mathbf{v}})_i]^2}{E_i} \text{ and } S = U^T E U. \tag{3-17}$$

Methods have also been developed for nonparametric multivariate tolerance regions, such as by Di Bucchianico based on the notion of equivalents blocks [103].

3.3.3 Prediction Regions

The goal of prediction is to determine future values of the response variable that are associated with a specific combination of predictor variable values. Generally, a predic-

tion model can be associated with the process by using regression analysis. The accuracy of the prediction, however, is subject to fluctuations due to uncertainties or statistical variability present in the sample. The prediction interval (or prediction region in the multivariate case) consists of the limits within which a predicted value is expected to lie with a prescribed probability. Generally, the data used to fit the model to a process can also be used to compute the prediction uncertainty range within which any predicted value is considered plausible.

While a tolerance interval provides acceptability ranges for a specified percentage of all future measurements, prediction intervals define limits for the value of a single measurement for a given set of predictor variable values. As a result, the estimation differs in that prediction intervals are based on central and variance parameters that are conditioned on the values of the predictors. Prediction regions are used in Chapter 4 to help the localisation of new landmarks based on known positions of other points in the shape.

3.3.4 Selection of Variables

In this thesis, each defined ILD is associated with a single statistical interval (*i.e.*, tolerance or prediction). The aim is to approximate the shape constraints, in particular regarding each individual landmark, by implicit analysis of the sum of the multiple statistical intervals associated with the ILDs. A sufficient number of intersections between the statistical intervals need to be considered to enable adequate approximation of the shape constraints. To this end, the exhaustive use of all the ILDs can be time consuming if the number of landmarks n is large (*e.g.*, a total of $n(n-1)/2$ and $n(n-1)(n-2)/6$ variables for two-point and three-point ILDs, respectively). Moreover, due to a potential lack of correlation between landmarks, some of the ILDs can have large statistical intervals, and thus are not useful for, or even detrimental to, the shape analysis. It is therefore more efficient to select a subset of the ILDs in practical situations, depending on the nature of the shape analysis task.

To achieve this, mainly geometry-based solutions have been suggested thus far. Trauss and Bookstein [104], for example, proposed a method to uniquely characterise biological shapes using a non-redundant number of inter-landmark distances based on triangulation.

Rohlf and Archie [105] developed a method to select inter-landmark distances based on their topological position on the shape boundary. In this thesis, since we are mainly interested in statistical-based image interpretation, two possible approaches based on statistical criteria are proposed instead. One is to group the landmarks into segments of smaller number of points with naturally high correlation. This approach was used in [106] to decompose a statistical model of shape into a set of smaller but statistically meaningful models. In this case, the ILDs used for shape modelling and analysis are all within the selected groups. An alternative approach is to select for each landmark a minimal number of ILDs with low variance, since they provide greater constraints on the landmark. Examples of varying ILD selection strategies are illustrated in Figure 3.3 on a left ventricular boundary, where (a) shows all possible inter-landmark connections from one single point and (b) displays the triangulation achieved with the method by Trauss and Bookstein. In (c), three groups of points are defined depending on their position on the LV (basal, mid-ventricular, apical regions) and all ILDs within are selected. Figure 3.3(d) displays a set of inter-landmark connections for each point in the shape selected based on low covariance criterion. It is worth noting that for highly dense meshes, the consistency of ILDs involving neighbouring landmarks can be affected. The proposed variable selection procedure , however, eliminates such penalizing ILDs since they generally induce a large tolerance interval.

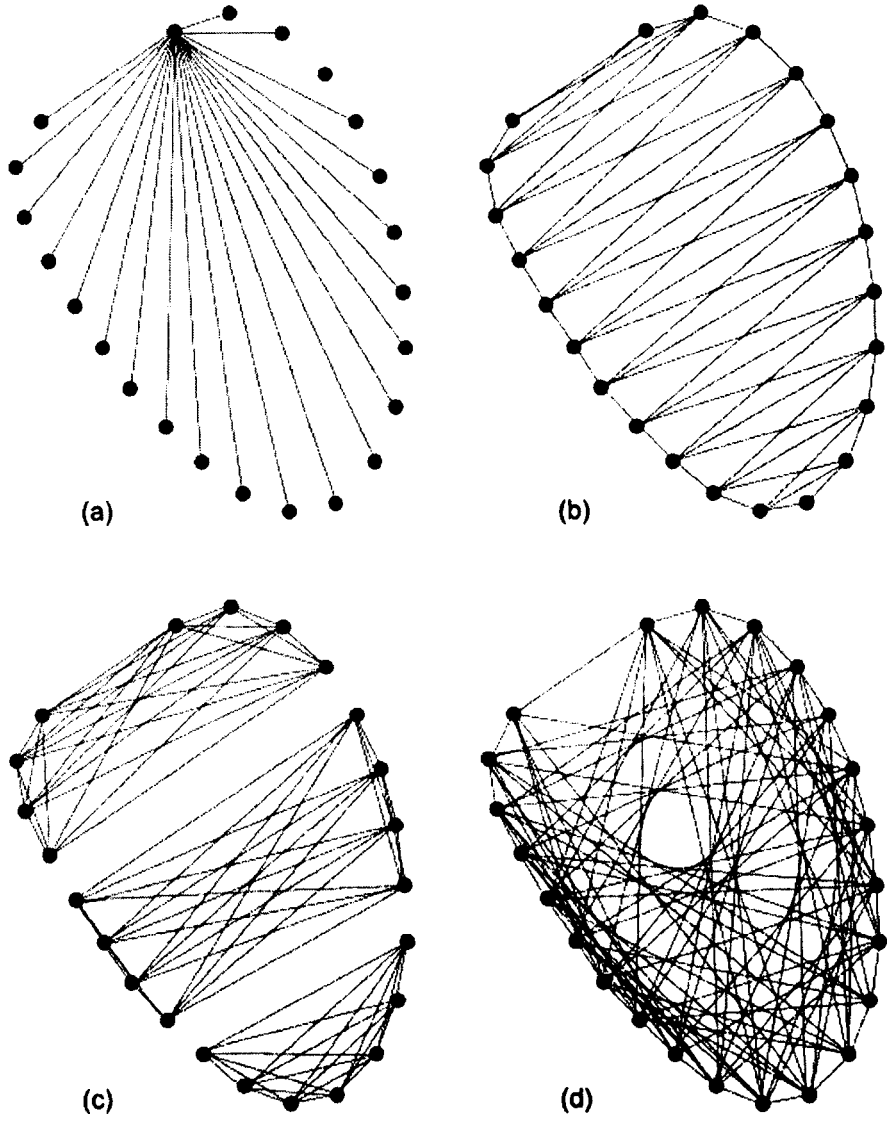

Figure 3.3 Illustration of the selection of a set of ILDs for shape representation. (a) shows all possible inter-landmark connections from a single point. In (b), a set of inter-landmark connections are selected using the triangulation proposed by Strauss and Bookstein [104]. In (c), three groups of points are defined depending on their position on the LV (basal, mid-ventricular, apical regions) and all ILDs within are selected. (d) displays a set of inter-landmark connections for each point in the shape selected based on a low covariance criterion.

3.4 Example ILD-based Shape Analysis

To illustrate the geometrical and statistical properties of the ILDs described in this chapter, a number of examples are given in this section to help understand the key concepts presented in this thesis. To this end, 50 long-axis cine MR images of the LV are extracted from a set of subjects aged between 18 and 76. The datasets were acquired using a 1.5T MR scanner (Sonata, Siemens, Erlangen Germany) and a TrueFISP sequence (TE = 1.5 ms, TR = 3 ms, slice thickness = 10mm and pixel size from 1.5 to 2mm) within a single breath-hold. Retrospective cardiac gating was used to ensure an even coverage of the entire cardiac cycle and for each subject 25 cine frames were acquired. The epi-cardial boundaries for all datasets are delineated by using a set of 23 landmarks, where point correspondence is established throughout the datasets by using the apex and mitral valve as the reference landmarks (similarly to Figure 2.1). For all the examples given in this chapter, no shape alignment or pre-processing of the shapes is carried out prior to the calculations of the ILDs. A set of univariate and multivariate ILDs are then calculated, including inter-landmark distances, ratios of distances, angles and barycentric coordinates.

3.4.1 Univariate ILDs

As mentioned earlier, inter-landmark distances and ratios of distances are amongst the most important ILDs. They are calculated for the training sample described above by considering all possible landmark combinations. For all these variables, normality tests are performed to show the ability of such ILDs to model normally distributed datasets. For this purpose, the nonparametric Lilliefors test for normality is used [107]. The method estimates the maximum discrepancy between the cumulative distribution function of the normal distribution and the empirical distribution function from the population. The test is known to perform well in the case of unknown mean and variance as well as for small sample sizes. The Lilliefors test uses a table of critical values computed from Monte Carlo simulation for sample sizes less than 1000. In this section, a critical value of 0.1457 is derived for the 50 datasets with a significance level of 1%.

Figure 3.4 illustrates the normality tests with respect to the critical value for inter-landmark distances (a) and ratios of distances (b). It is evident from the results that nearly all tests are below the critical value, with a percentage of accepted hypotheses of 96% for ILD distances and 98% for ILD ratios. This shows that the normality assumption is valid for these variables. The rejections during the normality test are mainly due to low correlation between some landmarks in the shape. For example, the level of correlation between the two valve points is evidently greater than the one between a valve point and the apex. Additionally, higher value associated with ILD ratio is due to scale invariant properties of the descriptor, which effectively eliminates potential size-related bias.

Figure 3.5 illustrates the ability of single univariate ILDs for describing key anatomical properties as well as geometrical correlations within the shape. In this example, the aim is to statistically characterise the relative positions of the valvular and apical points with the LV. To this end, the log ratio of distances is used as the basis for inter-landmark variable. Example results are shown in Figure 3.5(a) and the values obtained from the 50 datasets are plotted in Figure 3.5(b), along with the corresponding tolerance interval estimated by using Equations (3-8) and (3-9) (the tolerance factor k_2 is found equal to 2.37). Furthermore, the histogram derived from the population is plotted in Figure 3.5(c), where it can be seen that the univariate statistical distribution is well approximated by a Gaussian distribution.

This example illustrates the use of single ILD to implicitly encode geometrical properties (*e.g.*, length of the LV and size of the valves by using the triangle in Figure 3.5(a)). Furthermore, such variables have the potential to carry out statistical inference on landmark positions in an invariant fashion (*e.g.*, predict valve positions, identify abnormal apical regions). These properties will be shown in more detail in subsequent chapters.

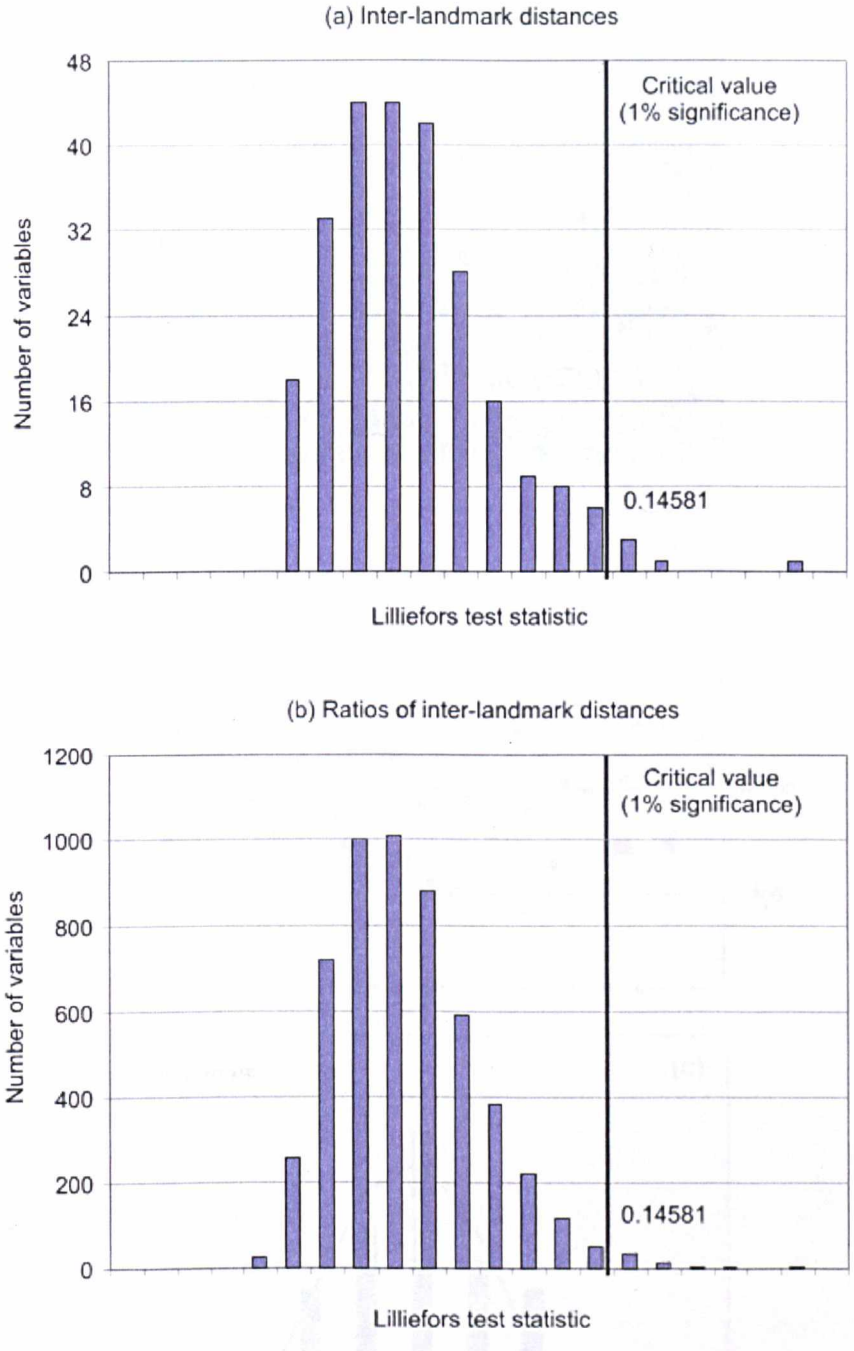

Figure 3.4 Lilliefors normality tests for inter-landmark distances (a) and ratios (b), as extracted from the epi-cardial datasets. It can be seen that nearly all tests are below the critical value, demonstrating normality (or near normality) distribution of the inter-landmark variables. The few cases where the normality hypothesis is rejected are due to a lack of correlation between the landmarks involved.

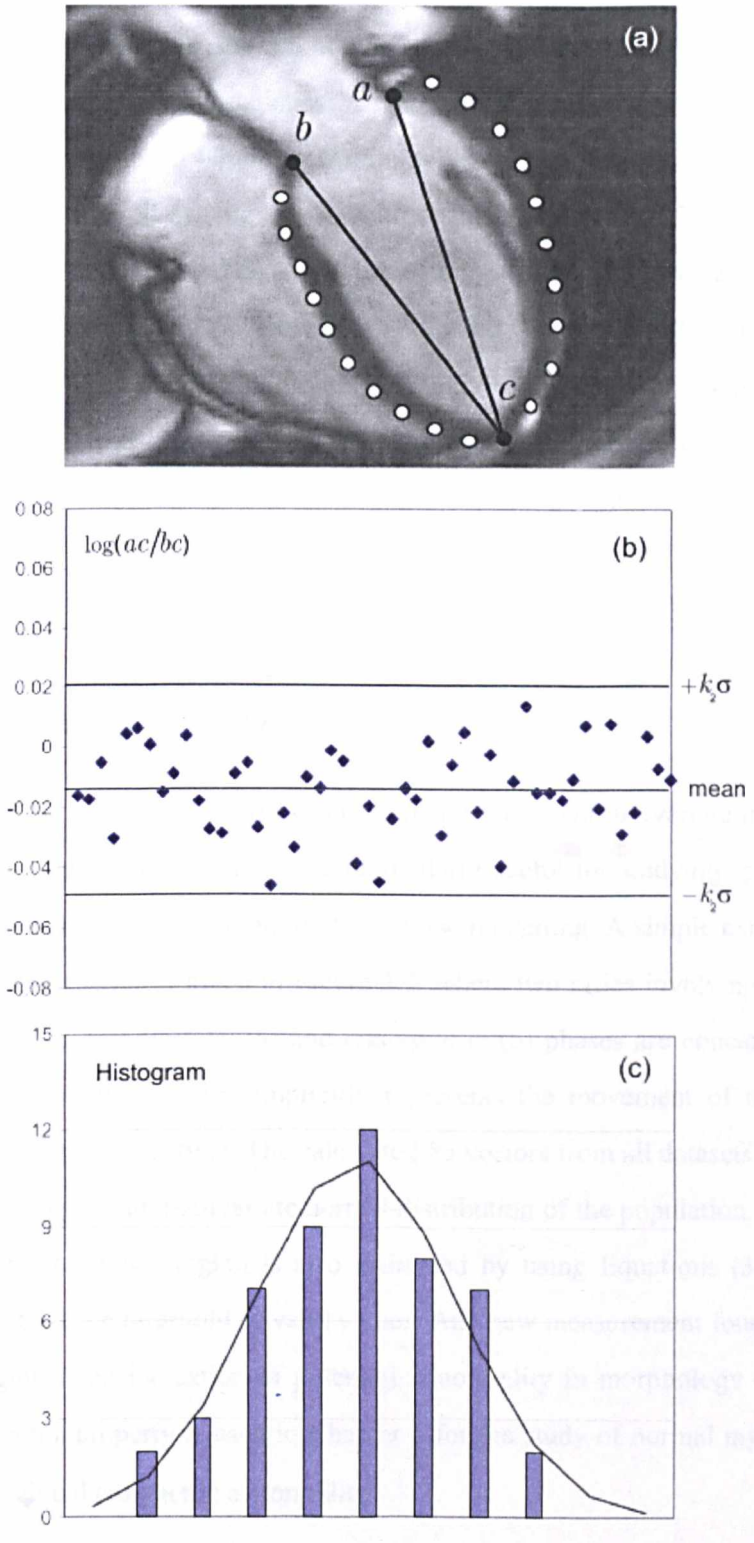

Figure 3.5 Illustration of a univariate ILD. The log of the ratio of inter-landmark distances is used to describe the invariant configuration of three landmarks. These variables, for example, can be used to constrain the lateral movement of the apical point during model instantiation.

Although it is not the main subject of this thesis, an example of the use of angular measurements and directional statistics in shape description is included in this section. The three selected angles in Figure 3.6(a) implicitly describe the position of the valvular and apical points, as well as length and width of the ventricle. The 50 angles calculated from the training set are plotted on a unit circle in Figure 3.6(b), showing clusters formed for each of the angular measures. The mean values and one circular standard deviation are also displayed for each case by taking into account the periodicity of angular ILDs based on Equations (3-1) and (3-3). Because angular descriptors have similar capabilities for studying triangles compared to ILD ratios but are more difficult to handle numerically particularly in 3D cases, they are not considered in the subsequent chapters for invariant shape description.

3.4.2 Multivariate ILDs

Multivariate ILDs can be obtained by concatenation of several univariate inter-landmark variables into a unique vector. They are particularly useful for studying spatio-temporal shape properties, such as those required for cardiac modelling. A simple example of such multivariate construction is given in Figure 3.7, where two ratios involving valvular and apical points from end-diastolic (a) and end-systolic (b) phases are concatenated into a single vector. The derived ILD implicitly represents the movement of the valve and ventricular shortening over time. The calculated 50 vectors from all datasets are plotted in Figure 3.7(c), suggesting multivariate normal distribution of the population. Furthermore, the multivariate tolerance region is also estimated by using Equations (3-14) and displayed to illustrate the threshold of valid values. Any new measurement found outside the tolerance region is an indication of potential abnormality in morphology or contractile behaviour. Such a property is used in Chapter 6 for the study of normal myocardial wall motion and regional contractile abnormality.

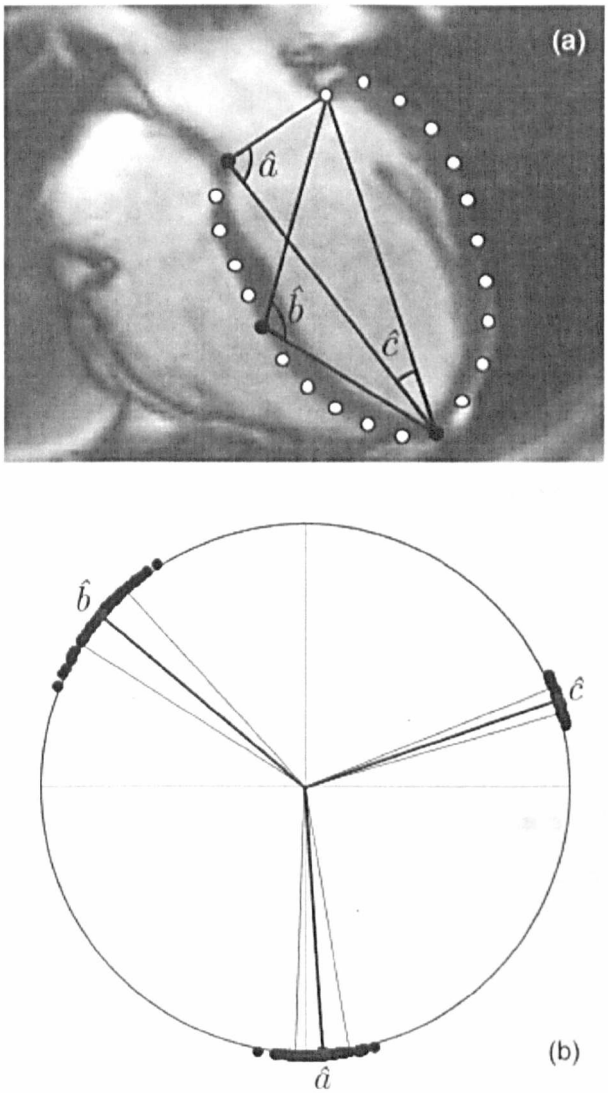

Figure 3.6 Illustration of the statistical analysis of angular measurements based on landmark data. The three selected angles describe implicitly the position of the valvular and apical points, as well as the length and width of the ventricle and the mitral valve. The 50 angles calculated from the training set are plotted on a unit circle, along with the mean values and one circular standard deviation calculated from Equation (3-6), by taking into account the periodicity of angular ILDs. It can be seen that the values calculated from the normal training datasets are well clustered for each angle.

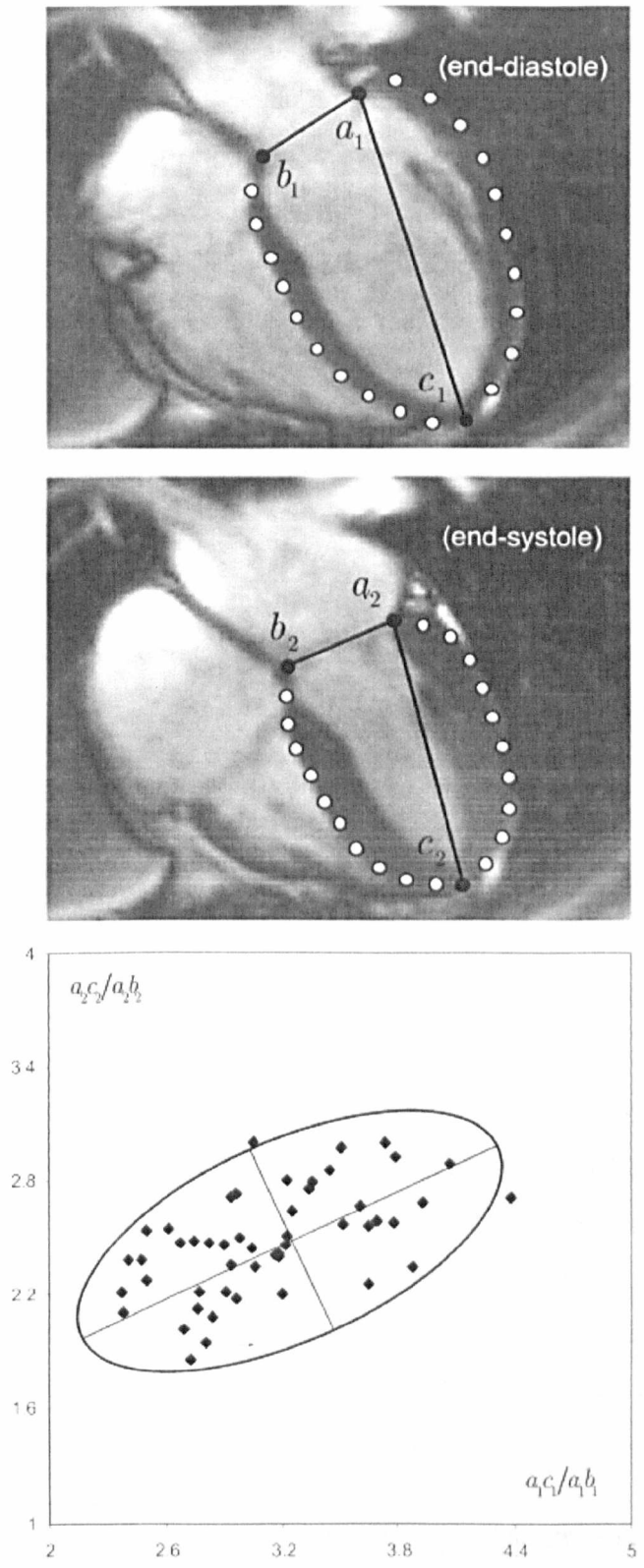

Figure 3.7 Illustration of a two-dimensional ILD. The variable describes the change in ratio of inter-landmark distances involving valvular and apical points at end-diastole and end-systole, therefore describing invariant movement of the valve.

Barycentric coordinates as introduced in Section 3.2.4 and their existing generalisations [91,92] can be considered as multivariate ILDs since they consist of a number of coefficients equal to the number of reference landmarks. Their standard formulation using a single triangle as the reference coordinate system is used in this section to model invariant landmark constraints. To this end, two different reference triangles (shown in Figures 3.8(a) and 3.8(b)) are first chosen to calculate the barycentric coordinates for all landmarks on the epi-cardial border of the training set. The obtained triplets of coefficients are then projected back onto the mean shape and displayed on the figures to illustrate the spatial distribution of these landmarks. It can be seen that a cluster is formed for each landmark, which can be modelled by using multivariate statistical regions. Furthermore, it can be observed that the landmark distributions, particularly in terms of variance, differ when changing the reference triangle. This is due to the varying inter-landmark correlations involved. The landmarks can be further constrained by using multiple reference triangles (and thus multivariate ILDs), as illustrated in Figure 3.8(c). The analysis of intersections between multiple tolerance regions is a central element of this thesis in order to approximate the global shape patterns in terms of individual landmark constraints.

3.5 Conclusions

In this chapter, we have introduced the basic concept involved in ILDs for shape analysis. The main motivation behind use of ILDs in this thesis is the inherent limitations of existing techniques to account for potential errors in shape alignment. As a result, essential tasks such as automatic initialisation, constrained feature point search, outlier handling and localisation of abnormality are difficult to achieve with these traditional approaches. In this thesis, ILDs are used to address these issues and enable more effective, robust yet sensitive shape-based image analysis.

Despite their early applications in some areas of biological shape analysis, ILDs have not been widely considered in medical image computing, mainly due to its difficulty in statistical manipulation. In this chapter, three main attributes of ILDs that can be used for shape analysis are considered. First, ILDs explicitly incorporate shape invariance and therefore can be applied when the pose parameters are unknown or difficult to be esti-

mated accurately. Furthermore, ILDs involve a small number of landmarks, thus enabling decomposition of global geometric constraints for more flexible shape analysis. Finally, by effective modelling of suitable inter-landmark relationships, the relevant correlations between different parts of the shape can captured, which is beneficial for both landmark prediction and analysis.

In this chapter, a number of ILD examples are provided to illustrate the basic feature of these descriptors. Multivariate ILDs have also been discussed, which include barycentric coordinates and spatio-temporal ILD vectors. Their properties for modelling normal anatomy, particularly through the use of statistical intervals, are illustrated. The intersection of multiple tolerance intervals is used in this thesis as the basis for imposing constraints on individual landmarks. It is important to note that the inter-landmark variables detailed in this chapter are only some examples of ILDs. Other variables describing inter-landmark patterns can also be constructed depending on the type of invariance, variability and applications of interest.

Since each ILD is associated with more than one point, it is not straightforward to make statistical inference on individual landmarks by simple analysis of the ILD values. The same problem arises in terms of landmark prediction, which also depends on the position of other landmarks of the shape. New algorithms and statistical modelling are required in order to effectively manipulate these ILDs for shape-based image analysis. This is the subject of subsequent chapters which will present a number of new methods based on ILDs. They include the use of ILD for shape invariant ASM initialisation and landmark constraints (Chapter 4), outlier handling (Chapter 5) and localised contractile abnormality detection (Chapter 6).

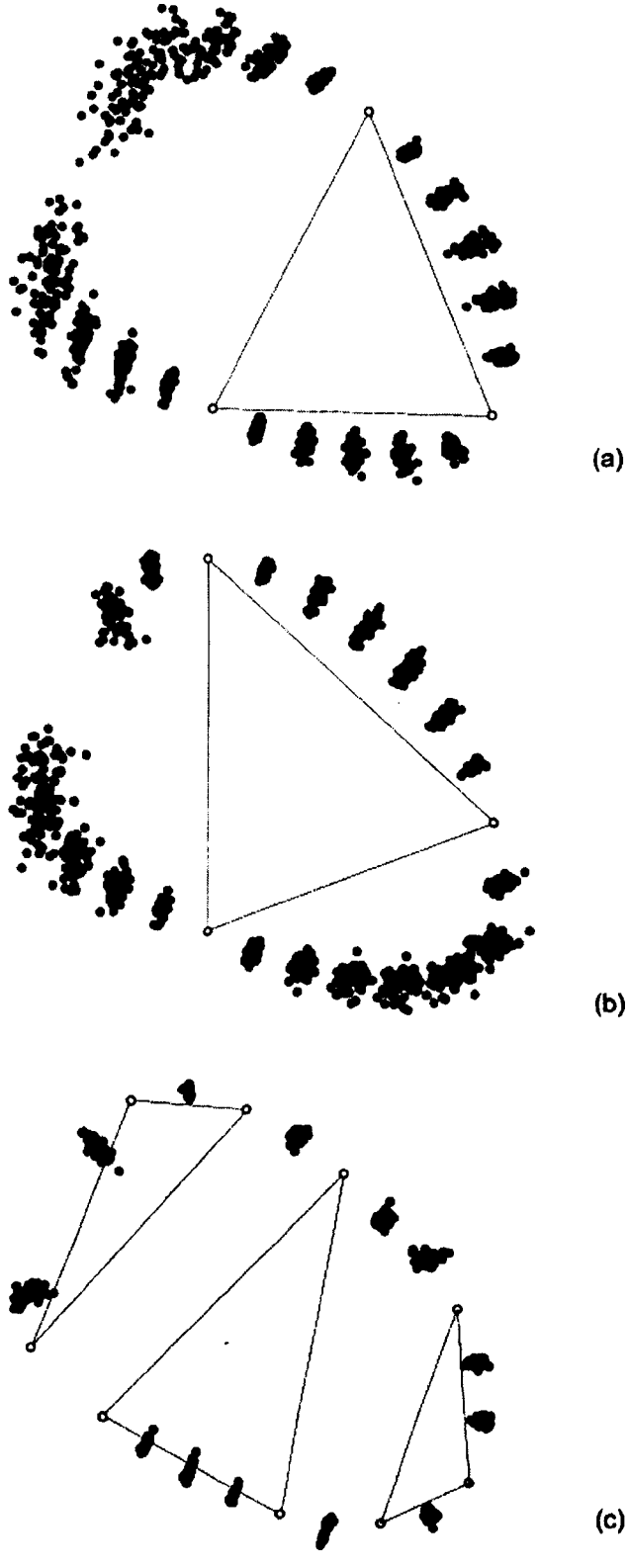

Figure 3.8 Illustration of barycentric coordinates of the landmarks. In (a) and (b), they are calculated for two distinct triangles, showing the invariant distribution of landmarks. In (c), three triangles are used, resulting in stronger constraints of the landmarks.

4

Inter-Landmark Constraints

4.1 Introduction

In the previous chapter, we have introduced Inter-Landmark Descriptors (ILDs) along with their key attributes for shape-based image analysis. The use of ILDs in this work is aimed at addressing the difficulties of conventional techniques based on landmark coordinates, *i.e.*, sensitivity to initial shape alignment and a global nature of the shape constraints. As a result, it is difficult to introduce suitable constraints to Active Shape Models (ASMs) for automatic shape initialisation and robust feature point search. To address these problems and enhance the accuracy of ASMs for complex segmentation tasks, this chapter will introduce a statistical formulation for incorporating effective landmark constraints based on ILDs*.

In ASMs, the application of global shape constraints during automatic initialisation is difficult due to the high-dimensionality of the problem and the size of the search space. In practice, however, an ASM requires suitable starting estimates to ensure that the search process does not get trapped in an undesirable local minimum. To illustrate its sensitivity to initialisation, Figure 4.1 shows a long-axis cardiac MR dataset with two different manual initialisation positions of the epi-cardial border of the Left Ventricle (LV). Significantly different results are obtained by using the same shape model and the

* Results first presented at 11th MICCAI Conference, New-York, 2008.

subsequent ASM fitting process. To rectify this problem, some exhaustive search methods can be adapted for automatic ASM initialisation including genetic algorithms [71], modified Hough Transform [72], and particle filtering [73]. These approaches, however, are inherently time consuming particularly for 3D cases. In this chapter, we will demonstrate how reliable and effective initialisation can be achieved by adequate decomposition of the global shape into a set of inter-landmark constraints.

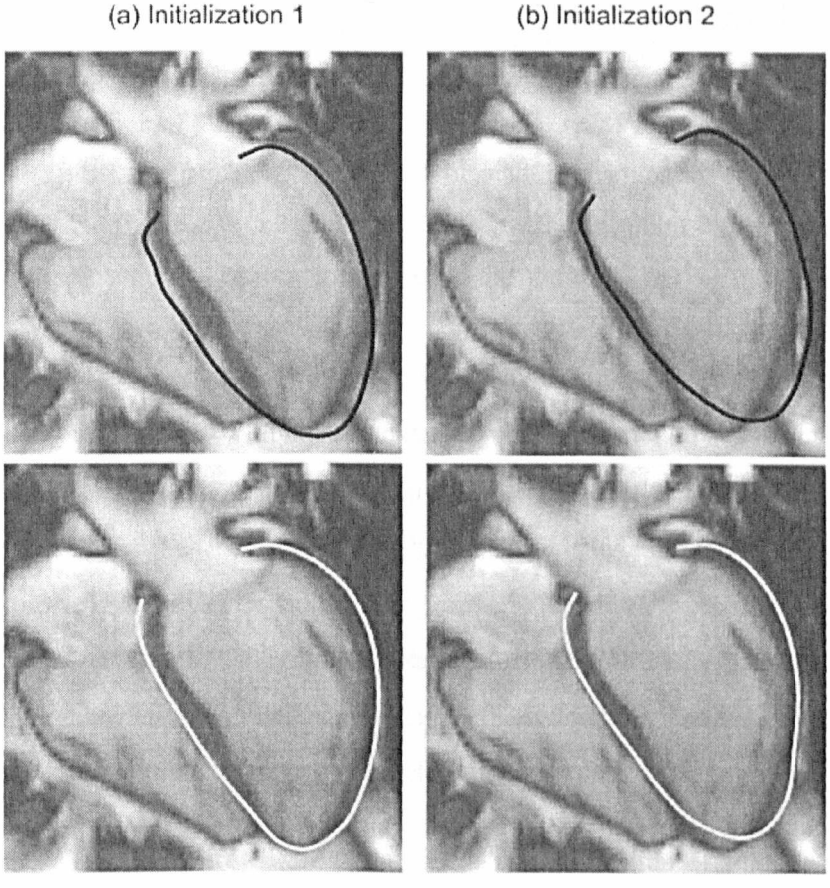

Figure 4.1 The effect of different ASM shape initialisations on the final results for a 2D epi-cardial dataset. Marked differences can be observed where in (a) it results in poor definition of the valvular points and in (b) it fails to localise the apex.

Furthermore, the global shape constraints of ASM prohibit imposing suitable search regions for each landmark. The common use of normal shape profiles can only cover a limited image space for each landmark but not in the tangential direction where potentially better candidates may be located. In practice, salient features such as high curvature

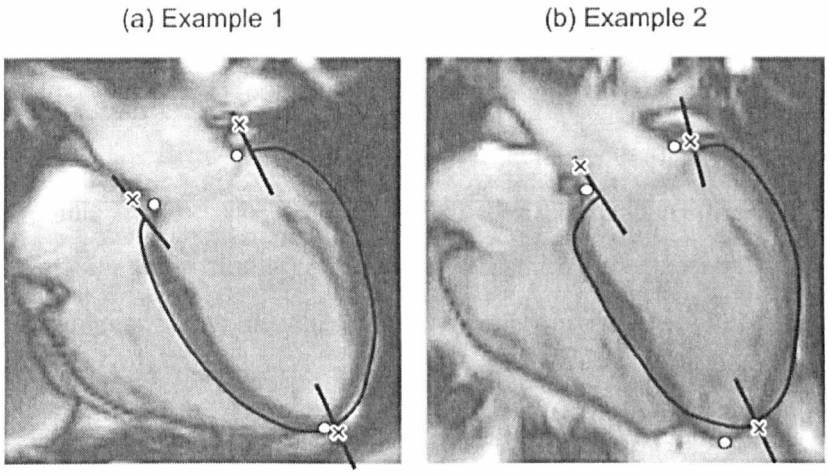

Figure 4.2 Illustration of the limitations of conventional ASM search using normal search profiles. In (a), the true positions for the valvular points are not covered by the normal search profiles. In (b), due to a poor definition of the apical point by the normal search profiles, a large localisation error is introduced at the apex.

points, corners, or end points may not be covered by the normal search profiles. Figure 4.2 illustrates this difficulty with another example of left-ventricular segmentation, where it can be seen that key landmarks corresponding to the valvular and apical regions are missed by using normal shape profiles. The limitation of using normal search profiles was in fact acknowledged by Cootes *et al.* many years ago [59] but the problem has so far not been specifically addressed. The trivial solution of using multidimensional search regions instead of the conventional radial search is not effective as this can lead to overlapping search regions, thus introducing large geometrical errors.

Another difficulty related to feature point search is the selection of suitable size of the search region. To address this problem, Cootes *et al.* [56] proposed a multi-resolution ASM strategy. At coarse resolutions, longer search profiles allow for better capture of salient features, whereas at finer resolutions, improved localisation is ensured. The technique, however, still depends on normal search profiles and in situations such as those encountered in Figure 4.2. Correct feature localisation is not guaranteed although the overall robustness of the algorithm does improve as a result. In this thesis, we will introduce a new concept of inter-landmark conditional probability which allows derivation of statistically sound search regions in terms of size, location and shape.

Another important consideration for increasing the robustness of feature point search is the use of partial geometrical constraints. To this end, Cootes *et al.* [59] simply used a set of PDMs using an increasing number of landmarks and proposed an algorithm to choose the feature points that are most consistent with the intermediate models. The method required the manipulation of a large number of PDMs and was biased towards the mean values. Other techniques involved the use of constraints between neighbouring points. For example, Behiels *et al.* [57] incorporated a smoothness term into the total cost function for feature point search. Hamarneh and Gustavsson [58] used dynamic programming for feature point selection to prevent temporal discontinuity. Although these methods do improve the quality of boundary localisation, the constraints are not statistically defined. Furthermore, many of these methods are still dependent on manual initialisation.

The main contribution of this chapter is to present a method for building inter-landmark constraints that can be used for decomposing the shape model into two independent processes. Specifically, a statistical formulation is introduced to enable prediction of the position of a single landmark based on the known positions of a set of points in the shape. The ILDs used for this purpose are translational invariant which is beneficial since the locations of the landmark points are unknown at initialisation and during feature point search. The immediate implication of the proposed approach is in its ability to derive statistically-based search regions with location and size automatically defined for each landmark, thus resulting in extended coverage of the target features and improved adaptation to complex structures. Subsequently, an optimal feature point selection algorithm is developed based on the A* graph search algorithm. Instead of selecting the feature candidates with the best grey-level properties within each search region independently, the proposed algorithm identifies in one single step the most salient and geometrically consistent feature candidates from all search regions. Finally, the inter-landmark constraints are used to permit reliable and efficient automatic initialisation of the ASM search without user interaction. The validation of the proposed algorithm is carried out with both 2D and 3D MR segmentation of left ventricular epi-cardial borders of varying complexities.

4.2 Methods

4.2.1 Inter-Landmark Conditional Probability

The modelling of the inter-landmark relationship between a single point and a set of m landmarks ($m < n$) within a family of shapes is to be explored in this section based on a statistical formulation that is translational invariant. Specifically, an inter-landmark conditional probability is introduced which describes the statistical distribution of a landmark $p_{s(i)}$ given the known positions of m points $p_{s(1)}$ to $p_{s(m)}$ within the same shape ($i > m$), *i.e.*,

$$P\left(p_{s(i)} \mid p_{s(1)}, \cdots, p_{s(m)}\right) = P\left(\mathbf{x}_{s(i)} \mid \mathbf{x}_{s(1)}, \cdots, \mathbf{x}_{s(m)}\right) \tag{4-1}$$

where s is an indexing function. Under the normality assumption of the ASM for training shapes of the same family of anatomical structures, the relationship between $p_{s(i)}$ and points $p_{s(1)}$ to $p_{s(m)}$ follows a pattern that can be modelled by using a multivariate Gaussian distribution according to the following p.d.f.:

$$\begin{aligned} &P\left(\mathbf{x}_{s(i)} \mid \mathbf{x}_{s(1)}, \cdots, \mathbf{x}_{s(m)}\right) \sim \\ &\exp\left(-\frac{1}{2}\left(\mathbf{x}_{s(i)} - \mathbf{x}^*\right)^T \mathbf{S}^{*-1}\left(\mathbf{x}_{s(i)} - \mathbf{x}^*\right)\right) \end{aligned} \tag{4-2}$$

where $\mathbf{x}^*$ and $\mathbf{S}^*$ are, respectively, the corresponding mean location and covariance of $p_{s(i)}$ conditioned on the location of the points $p_{s(1)}$ to $p_{s(m)}$. The mean vector can be regarded as the predicted location of landmark $p_{s(i)}$ when feature points $p_{s(1)}$, ..., $p_{s(m)}$ are known, whereas the covariance describes the associated multivariate prediction interval.

In order to estimate these parameters, a landmark-based parametric model is required to establish the relationship between $p_{s(i)}$ and $p_{s(1)}$ to $p_{s(m)}$. To this end, the proposed formulation is based on a generalisation of barycentric coordinates [87] introduced in Chapter 3. In the proposed method, an arbitrary polygon can be used as a basis coordinate system to uniquely describe any point in the underlying space. The vector of coordinates $\mathbf{x}_{s(i)}$ within each training sample is an affine combination of the vectors $\mathbf{x}_{s(1)}$, ..., $\mathbf{x}_{s(m)}$, *i.e.*,

$$\mathbf{x}_{s(i)}^{(j)} = \sum_{k=1}^{m} a_{s(k)} \mathbf{x}_{s(k)}^{(j)} + \mathbf{t} + \mathbf{e}^{(j)}$$
$$\text{for } 1 \le j \le N, \text{ where } \sum_{k=1}^{m} a_{s(k)} = 1. \tag{4-3}$$

The coefficients $a_{s(k)}$ are the weights associated with each landmark vector $\mathbf{x}_{s(k)}$ and they sum to 1 to ensure translational invariance. The vectors $\mathbf{t}$ and $\mathbf{e}^{(j)}$ are translation and residual descriptors, respectively. The formulation in Equation (4-3) has some connections to multivariate regression analysis, except that the proposed landmark-based parametric model assigns one single coefficient for each vector of coordinates (the same coefficient for all coordinates of the same point) and more importantly it is invariant to translation of all landmarks in the image space. The coefficients $a_{s(k)}$ and vector $\mathbf{t}$ are calculated by minimising the sum of squared distances between the coordinates from the training samples and the predicted values, *i.e.*,

$$a_{s(k)}, \mathbf{t} \sim \underset{a_{s(k)}, \mathbf{t}}{\operatorname{argmin}} \sum_{j=1}^{N} \mathbf{e}_j^T \mathbf{e}_j \tag{4-4}$$

which can be solved under the constraints by using Lagrange multipliers.

Given the known locations of $\mathbf{x}_{s(1)}, ..., \mathbf{x}_{s(m)}$ of a set of landmarks in an image, the conditional mean location and covariance of landmark $\mathbf{x}_{s(i)}$ can be calculated as follows:

$$\mathbf{x}_{s(i)}^{*} = \sum_{k=1}^{m} a_{s(k)} \mathbf{x}_{s(k)} + \mathbf{t},$$
$$\mathbf{S}_{s(i)}^{*} = \frac{1}{N} \sum_{j=1}^{N} \mathbf{e}_j \mathbf{e}_j^T. \tag{4-5}$$

It can be seen that the conditional covariance matrix is constant while the conditional mean location depends on the specific values of $\mathbf{x}_{s(1)}, ..., \mathbf{x}_{s(m)}$. This result is consistent with basic conditional probability theory for normal distributions.

The inter-landmark relationship described in this chapter enables the prediction of the location of a new point within a certain region. The conditional prediction region A is a 3D ellipsoid centred at the conditional mean with axes defined by the conditional covariance matrix:

$$A\left(\mathbf{x}_{s(i)} \mid \mathbf{x}_{s(1)},\cdots,\mathbf{x}_{s(m)}\right) = \left\{\mathbf{x} \in \mathbb{R}^3 \mid \left(\mathbf{x}_{s(i)} - \mathbf{x}^*\right)^T \mathbf{S}^{*-1} \left(\mathbf{x}_{s(i)} - \mathbf{x}^*\right) < U_A\right\}. \quad (4\text{-}6)$$

where U_A controls the size of the prediction region A, which in practice can be specified based on the chi-squared distribution [102].

By using the inter-landmark prediction regions, it becomes possible to run a constrained search algorithm for all landmarks in the image. In the following sections, two algorithms based on partial geometrical constraints are presented. The first algorithm allows the extraction of optimal feature points in the ASM and the second algorithm provides an automatic method for ASM initialisation.

4.2.2 Optimal Feature Point Search

As mentioned in the introduction, the feature point search which is central to the ASM is traditionally carried out using normal search profiles with limited coverage of the image without use of geometrical information. To alleviate some of the problems introduced, an optimal feature point search algorithm is developed in this chapter based on inter-landmark conditional probabilities. The goal of the method is to derive suitable search regions that are statistically defined by introducing geometric constraints during the search, as well as to find the optimal set of feature points according to the pre-defined grey-level cost function d_1 (Section 2.3.1).

Instead of searching for feature points independently for all landmarks, the proposed algorithm uses a sequential approach through which feature points are successively investigated from $p_{s(1)}$ to $p_{s(n)}$, where s is an indexing function that describes the order in which points are visited during the search. For each landmark $p_{s(m)}$ $(1 < m \leq n)$, the locations of previously selected feature points $(p_{s(1)}, ..., p_{s(m-1)})$ are taken into account. This is achieved through the introduction of prediction regions $A\left(\mathbf{x}_{s(i)} \mid \mathbf{x}_{s(1)},\cdots,\mathbf{x}_{s(m-1)}\right)$ calculated from (14) in the previous section. This ensures the ASM to consider a region of suitable location and size based on statistical criteria instead of the conventional normal search profiles. A number of candidates are evaluated within each prediction

region A and several paths can be constructed in this manner from $p_{s(1)}$ to $p_{s(n)}$. The optimal path is extracted efficiently by using a combinatorial approach based on the A* algorithm [108].

The A* algorithm is a graph search algorithm, based on a best-first and heuristic approach, that can find efficiently solutions to least-cost path problems. It incrementally explores the routes leading from the starting point by considering first the routes that appear to be most likely to lead towards the goal. This is achieved by considering for each path the actual cost of the pat (referred to as the cost function g) and an estimation of the remaining cost to the goal (the heuristic function h). This allows efficient elimination of implausible paths and prioritisation of the remaining solutions. At each stage of the search, the path with the minimal sum of the cost and heuristic functions (*i.e.*, with the cheapest estimated cost to the final point) is further developed by exploring the candidates for the next node.

In the proposed algorithm, each path L is characterised by the parameters $\hat{\mathbf{x}}$, m, g and h, where $\hat{\mathbf{x}}$ defines the coordinates of the feature points in the path and m is the number of feature points identified by the sequential search. g and h are the A* functions defined above to localise the optimal path and subsequently best set of landmark locations for the ASM. It is evident that the quality of the search for the next point $p_{s(m+1)}$ depends on whether the prediction region $A\left(\hat{\mathbf{x}}_{s(m+1)} \mid \hat{\mathbf{x}}_{s(1)},\ldots,\hat{\mathbf{x}}_{s(m)}\right)$ intersects with the target feature on the boundary, which is more likely if points $\hat{\mathbf{x}}_{s(1)},\ldots,\hat{\mathbf{x}}_{s(m)}$ in the current path are correctly identified. Therefore, two properties of the path are simultaneously measured: the quality of the selected points in the path $(\hat{\mathbf{x}}_{s(1)},\ldots,\hat{\mathbf{x}}_{s(m)})$ (the cost function g) and the likelihood of intersection of the remaining prediction regions $A\left(p_{s(m+1)} \mid p_{s(1)},\ldots,p_{s(m)}\right)$ to $A\left(p_{s(n)} \mid p_{s(1)},\ldots,p_{s(m)}\right)$ with the target boundary (the heuristic function h).

The cost function g is calculated by summing all the individual grey-level costs in the actual path:

$$g(L)=\sum_{k=1}^{m} d_{\mathrm{I}}\left(\hat{\mathbf{x}}_{s(k)}\right), \tag{4-7}$$

while the heuristic function h calculates the minimal grey-level cost required to reach the final point by summing the minimum grey-level costs within the prediction regions for each remaining landmark ($p_{s(m+1)}$ to $p_{s(n)}$), *i.e.*,

$$h(L) = \sum_{k=m+1}^{n} \min_{A} \left[d_I \left(\hat{\mathbf{x}}_{s(k)} \in A\left(p_{s(k)} \mid p_{s(1)}, \ldots, p_{s(m)} \right) \right) \right]. \tag{4-8}$$

In other words, the cost function g favours paths with the most consistent and salient grey-level properties, whilst the heuristic function h penalises paths with unsuitable boundary intersection of the remaining prediction regions, which are therefore likely to lead to poor intensity characteristics.

All the generated paths are stored in a priority queue Q and at each iteration of the A* algorithm, the path L with the minimal sum of the cost and heuristic functions is selected from Q for further expansion, *i.e.*,

$$L = \arg\min_{L \in Q} \left[g(L) + h(L) \right]. \tag{4-9}$$

The search is continued until the first path in the queue reaches the final landmark $p_{s(n)}$, indicating that no better path (set of feature points) can be found. This is because the heuristic function in Eq. (4-8) is admissible, *i.e.*, it never overestimates the actual minimal cost of reaching the goal. This is a fundamental property of the A* algorithm which is complete and always returns the optimal solution [108].

To increase the efficiency of the method, a suitable definition of the indexing function s is required, which describes the order in which the feature points are visited during the A* algorithm. Ideally, the prediction region at each path expansion should be as small as possible to minimise the size of image region to be explored and the number of paths to be expand. Starting from an initial point $p_{s(1)}$ chosen as a potential landmark in the shape (*e.g.* corner, high curvature, particular image feature), a good strategy is to choose at the i^{th} position in s the landmark that correlates most with previous points $p_{s(1)}, \ldots, p_{s(i-1)}$ in the sequence. This is equivalent to choosing the point with the minimal determinant of the conditional covariance matrix, *i.e.*,

$$s(i) = \arg\min_{k}\left[\det\left(\mathbf{S}_k^* = \mathrm{cov}\left(p_k \mid p_{s(1)},\ldots,p_{s(i-1)}\right)\right)\right]$$
$$\text{where } k \in \{1,\ldots,n\} - \{s(1),\ldots,s(i-1)\}. \tag{4-10}$$

Finally, it is worth noting that the conditional probability $P\left(p_{s(m)} \mid p_{s(1)},\ldots,p_{s(m-1)}\right)$ can be approximated by using only a subset of the points $p_{s(1)}$, ..., $p_{s(m-1)}$ that best correlates with the point $p_{s(m)}$ to speed up the calculations.

Listing 4.1. The optimal feature point search algorithm

```
1   initialise priority queue with paths starting from each initial candidate
    Q = {L : x̂ ∈ H_s(1), with m(L) = 1, g(L) = d_1(p_s(1) = x̂), h(L) ~ (4-1)}
2   select first path in the queue: L_0 = arg min_{L∈Q} [g(L) + h(L)]
3   if m(L_0) = n then
4       return L_0 as the optimal path.
        x(L_0) is the set of feature points
5   Else
6       increment m
7       For each x̂ in A(p_s(m) | L_0)
8           create new path x(L, m) = x̂
9           update the cost and heuristic functions
10      end for
11      go to step 2
12  end if
```

4.2.3 Automatic Initialisation

Automatic initialisation of ASM is a difficult task since it involves the estimations of all landmark positions simultaneously. Exhaustive search requires excessive computation time and therefore is not practically feasible. The advantage of using inter-landmark relationships and the feature point search described in this chapter is that initialisation

only needs to be performed for the first point $p_{s(1)}$. A trivial solution is to select the entire image or a region of interest for the initial point, followed by optimal feature point search. Such a solution, while guaranteed to produce an optimal ASM solution, could be time consuming. The aim of this section is to propose a reliable and efficient method for the selection of the initial point.

The proposed method is based on the following two main features of the proposed conditional search regions. Firstly, unsuitable initial candidates are unlikely to generate inter-landmark prediction regions for other points that intersect the boundary of interest. The second is that the prediction region $A\left(p_{s(m+1)} \mid p_{s(1)}\right)$ is unlikely to intersect the target boundary if the prediction regions for points $p_{s(m)}$ to $p_{s(2)}$ do not. Based on these observations, the initialisation process associates parameters $\hat{\mathbf{x}}$, m, v with each candidate in the image. By defining $\hat{\mathbf{x}} = (\hat{x}, \hat{y}, \hat{z})^T$ as the coordinate vector describing its location in the image, m the number of prediction regions tested for intersection, and v a value that describes the quality of intersections of the m first remaining prediction regions with the target boundary, all candidate points are entered into a queue and initialised as follows:

$$\begin{cases} m = 1, \\ v = d_1\left(\mathbf{x}_{s(1)} = \hat{\mathbf{x}}\right). \end{cases} \tag{4-11}$$

The candidates are subsequently sorted according to the lowest value of v, which at the start is the degree of match of the initial point with its modelled local grey-level properties. At each stage, the first candidate in the queue is updated as follows:

$$\begin{cases} m = m + 1, \\ v = \dfrac{m-1}{m} v + \\ \quad \dfrac{1}{m} \min_{A} \left[d_1\left(\mathbf{x}_{s(m)} \in A\left(p_{s(m)} \mid \mathbf{x}_{s(1)} = \hat{\mathbf{x}}\right)\right)\right]. \end{cases} \tag{4-12}$$

The value v describes the average of the minimal grey-level costs within the first m prediction regions. For unsuitable candidates for $p_{s(1)}$, a high value of v is expected and therefore these will be pushed to the back of the queue. On the other hand, candidates located at, or close to, the true initial point are likely to intersect with the prediction

regions, and therefore are brought forward in the priority queue for further evaluation. At each iteration, the first candidate in the queue has the best boundary intersection and is further evaluated by updating m and v based on Equation (4-12). The algorithm terminates when the first few candidates reach a value of m that equals to n. With this approach, unlikely locations for the initial point are typically eliminated by a limited number of intersection tests, thus enabling efficient computation in practice.

Listing 4.2. The automatic initialisation algorithm

1 **initialise** priority queue by scanning the input image **I**

$Q = \left\{ \mathbf{x} \in \mathbf{I} \text{ with } m(\mathbf{x}) = 1, v(\mathbf{x}) = d_1\left(p_{s(1)} = \mathbf{x}\right) \right\}$

2 **initialise** output set $H_{s(1)} = \varnothing$

3 **select** first candidate in the queue: $\mathbf{x}_0 = \arg\min_{\mathbf{x} \in Q} [v(\mathbf{x})]$

4 **if** $m(\mathbf{x}_0) = n$ **then**

6 **add** $\mathbf{x}_0$ to initial candidates:

$H_{s(1)} = H_{s(1)} \cup \{\mathbf{x}_0\}$, $Q = Q - \{\mathbf{x}_0\}$

if size of $H_{s(1)} = K$ **then**

return

end if

5 **else**

7 **increment** m

8 **update** v value according to equation (4-13)

9 **go to** step 3

10 **end if**

In most medical imaging applications, initial values for rotation and scaling can be derived from the DICOM header. In cardiac MR, for example, the orientation of the short axis images is relatively well-defined for normal subject and most patients when scanned in supine or prone positions. Similarly, the initial rotation and scaling parameters can also be defined from the scan parameters. Nevertheless, the rotation and scaling parameters

can be efficiently estimated using the proposed initialisation, by copying all candidates in the image for varying values and application of the same procedure as above. Candidates with unsuitable rotation and scaling are pushed back in the priority queue due to a lack of intersection of the corresponding prediction regions with the target boundary.

Table 4.1 Values of the parameters used for the experiments.

Variable		2D	3D
n	Number of landmarks	23	133
N	Number of datasets	20	20
	Part of shape variation explained by the statistical models	0.99	0.99
	Bounds on eigenvalues	3	3
	Grey-level profile length on either side of the landmark point	7	7
	Local search size on either side of the current point	10	10
	Profiles step size (*mm*)	2.0	2.0
	Maximum number of iterations for the ASM search	100	100
	Variation around initial scaling (1.0)	0.2	0.2
	Variation in angle around initial value (degrees)	30	30
K	Number of initial candidates	8	8
U_A	Threshold for prediction regions	13.95	13.95

4.3 Validation

4.3.1 Experiments

The proposed method is validated with 2D and 3D segmentation of the epi-cardial border of the LV from both long and short-axis MR images. In cardiac MRI, reliable segmentation of the epi-cardial boundary with minimal user interaction is a difficult task because it is often surrounded by fat and confusing anatomical structures. Furthermore, the automatic definition of the valve and apex is difficult.

For the purpose of evaluating the proposed method, the LV datasets were collected from 20 subjects, including 13 normal, 5 locally abnormal (myocardial injury) and 2 severely abnormal (ventricular dilatation). To this end, a 1.5T MR scanner (Sonata, Siemens, Erlangen Germany) and a TrueFISP sequence (TE = 1.5 ms, TR = 3 ms, slice thickness = 10 mm, pixel size of 1.5 to 2 mm) within a single breath-hold were utilised. For providing the ground-truth data for evaluating the accuracy of the proposed algorithm, the long and short axis images were annotated by an expert observer. The estimation of the inter-landmark conditional probabilities was carried out on a leave-one-out basis. For automatic initialisation, the initial point $p_{s(1)}$ was chosen as the apex or the lower RV/LV junction of the mid-ventricular slice for 2D long axis or 3D multi-slice segmentation, respectively. For comparison, these datasets were also segmented using the original ASM [5] and its robust extension based on robust estimators [62]. These methods were initialised by placing the mean shapes for each long and short axis image at the centre of the corresponding manual segmentations. The same local intensity models and grey-level cost function were used for all methods based on the standard ASM search formulation [51].

4.3.2 Results

Table 4.2 provides a detailed error analysis for the segmentation results (mean, standard deviation, min and max) for both 2D and 3D datasets. To facilitate visualisation, the segmentation errors for the 20 datasets and comparisons to existing methods are also provided in Figures 4.3 (2D case) and 4.4 (3D case). In Figures 4.3(a) and 4.4(a), the

results of the proposed technique are compared with the original ASM, while they are compared with the robust ASM in Figures 4.3(b) and 4.4(b). The performance of the proposed automatic initialisation is detailed in Figures 4.3(c) and 4.4(c).

Table 4.2 Detailed error analysis of the ASM methods (in *mm*).

Method	2D				3D			
	Mean error	Std.	Min error	Max error	Mean error	Std.	Min error	Max error
Original ASM	2.01	1.12	0.87	4.98	2.13	1.01	0.98	4.94
Robust ASM	1.71	0.92	0.86	4.38	1.65	1.00	0.92	4.66
Auto. initialisation	1.23	0.32	0.82	1.88	1.60	0.41	0.96	2.67
Proposed method	1.13	0.32	0.64	1.82	1.11	0.25	0.79	1.84

It is evident from the obtained results that the robustness of the original ASM is relatively poor for epi-cardical segmentation. This is because the target structure, unlike the endo-cardial borders, is often poorly defined and coupled with considerable artefacts. The robust ASM has improved the original ASM results (14 % average improvement in 2D and 22 % in 3D), but its performance is inconsistent for all the datasets studied, as shown in Figures 4.3(b) and 4.4(b). It is also evident from the results that the proposed method outperforms the existing techniques used for comparison. In particular, it can be seen that on average the automatic initialisation alone performs better in shape localisation, which demonstrates the reliability of the algorithm. The entire framework using automatic initialisation and the optimal feature selection performs consistently well for all datasets as it can be seen in Figures 4.3 and 4.4. The maximal segmentation error is less than 2 mm and the average improvement as compared to ASM and robust ASM is 46 % and 33 %, respectively. The achieved performance gain is largely due to the geometrically constrained selection of feature points and the robustness of the initialisation process.

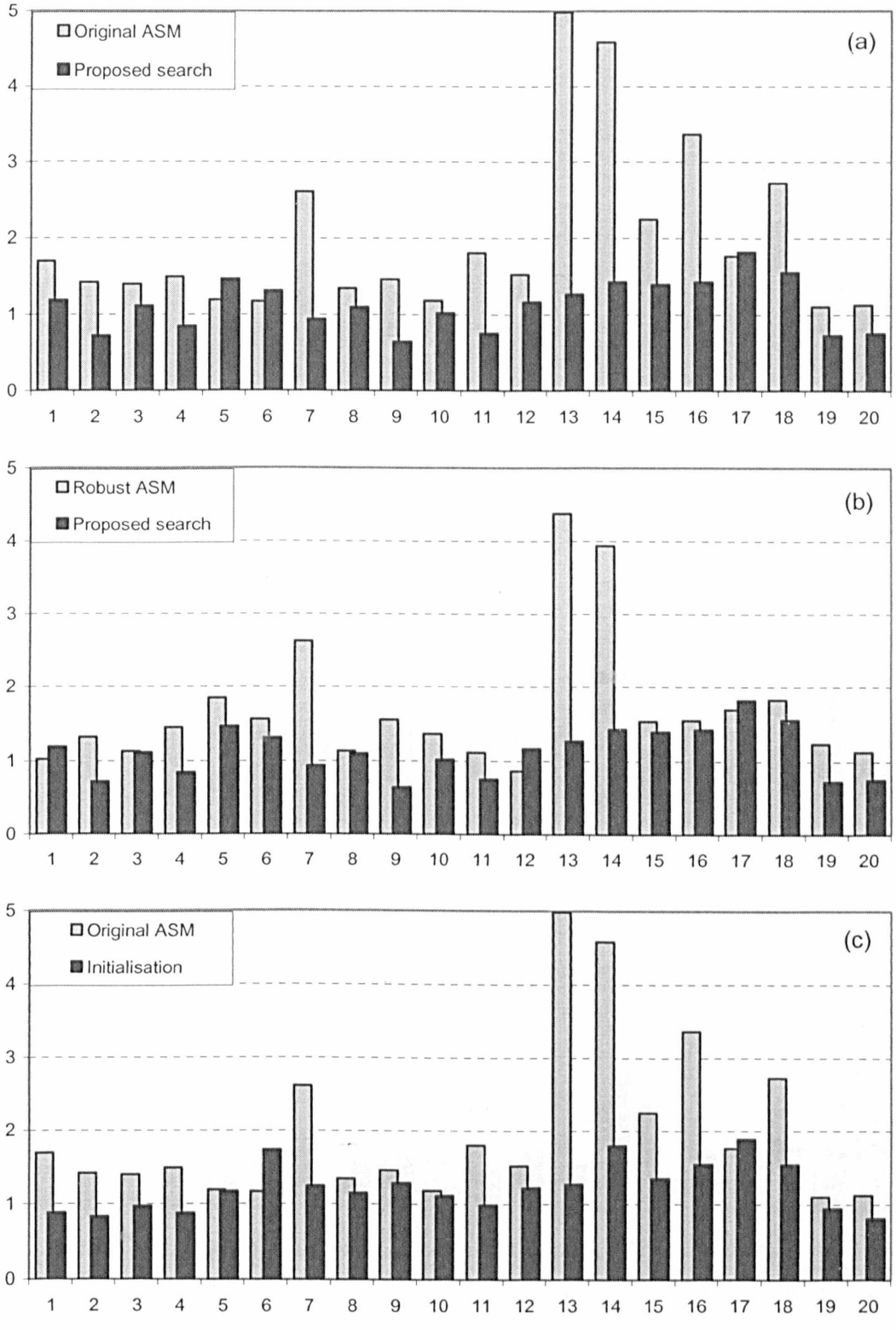

Figure 4.3 2D segmentation results for the 20 epi-cardial datasets. The proposed technique is compared to the original ASM in (a) and to the robust version [62] in (b). The initialisation results are shown in (c) in comparison with the ASM errors.

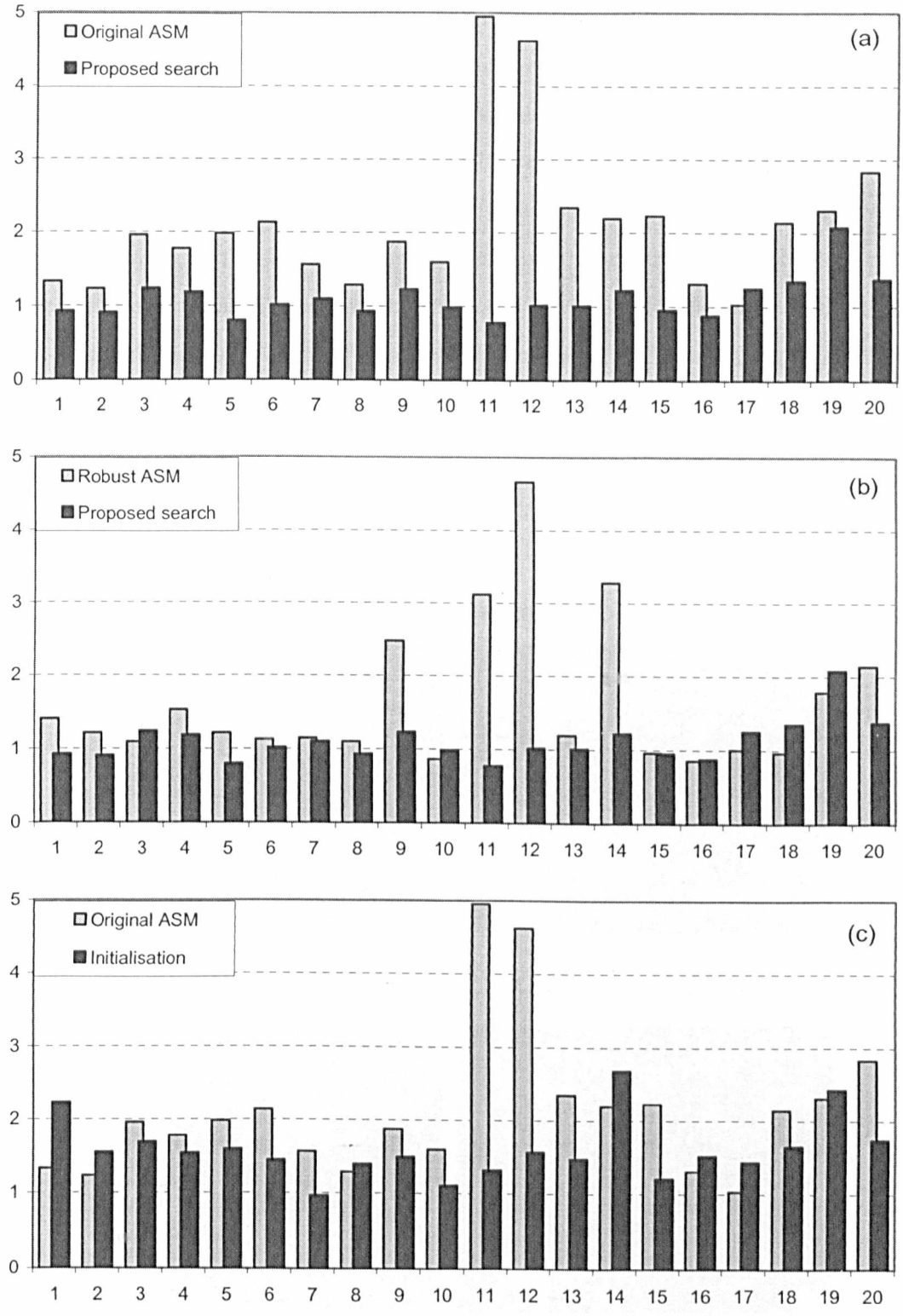

Figure 4.4 3D segmentation results for the 20 epi-cardial datasets. The proposed technique is compared to the original ASM in (a) and to the robust version [62] in (b). The initialisation results are shown in (c) in comparison with the ASM errors.

Figure 4.5 illustrates a 2D example demonstrating the strength of the proposed algorithm. The 2D long axis view shows a dilated LV with relatively poor delineation of the epicardial boundaries, especially at the apical and lateral apical regions. As a result, the original ASM fails to recover the boundary of interest (see (b)) with an average segmentation error of 4.58 mm. The optimal feature point selection in subsequent iterations is further illustrated in (a), where two intermediate stages of the procedure are shown. It can be seen that the statistical based search regions (white ellipses) as calculated from the inter-landmark conditional probabilities become smaller as the boundary approaches the underlying landmark features. This restricts the selection algorithm to true candidate positions on the boundary. The final segmentation result shown in (c) demonstrates the accuracy achieved for boundary localisation as well as for definition of salient landmarks (valve and apex points).

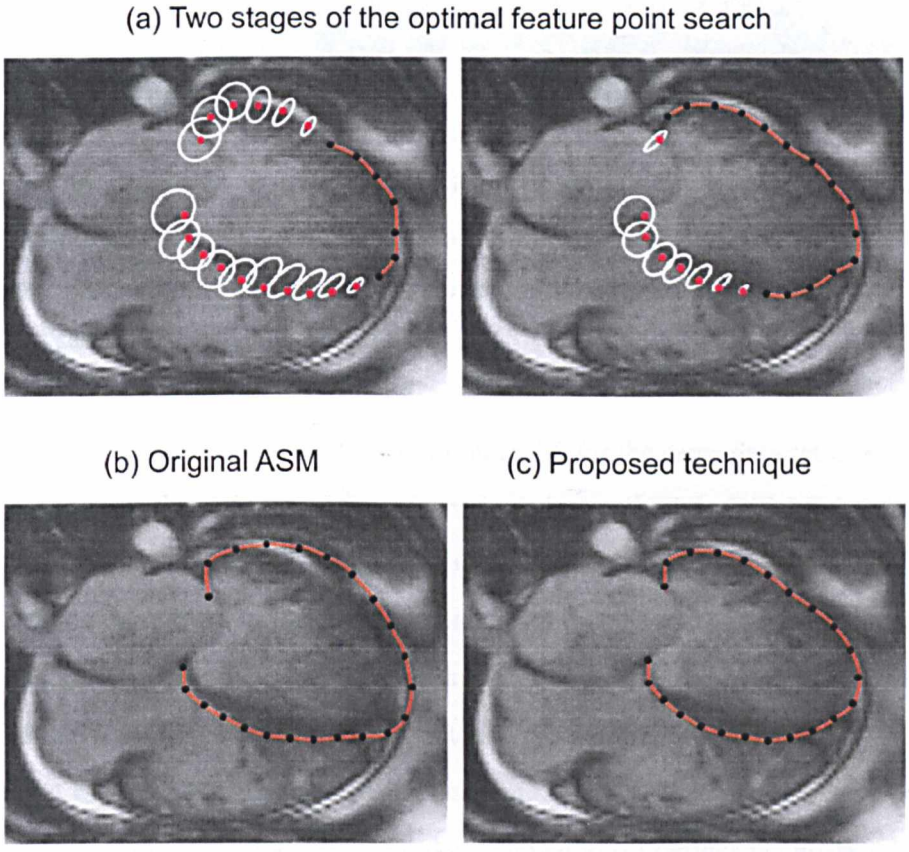

Figure 4.5 Example of the optimal feature point search (c) as applied to a difficult dataset with poor boundary contrast. Significant improvement is achieved over the original ASM method (b). Two intermediate stages and the corresponding statistical prediction regions are shown in (a).

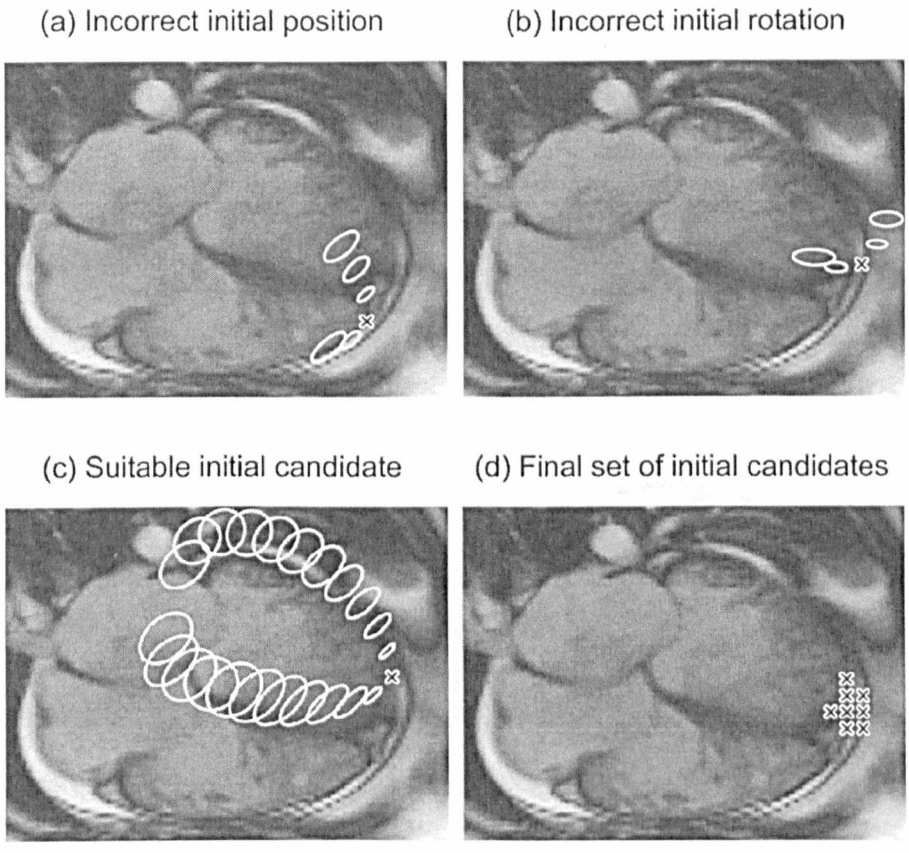

Figure 4.6 Illustration of the proposed automatic initialisation. In (a) and (b), incorrect initial position and rotation are eliminated after a few intersection tests. (c) displays the prediction regions corresponding to a suitable initial candidate. (d) shows the set of candidates selected for the initial point.

The automatic initialisation is illustrated in Figure 4.6 for the same data set in Figure 4.5. In (a), the apex of the right ventricle is investigated as a possible initial point due to its resemblance to that of the LV. This, however, is rejected only after a few conditional search regions considered in heuristic calculation. These landmark allowable domains do not intersect with the target image features, and therefore have large grey-level discrepancies. Similarly in (b), incorrect initial rotation is eliminated due to poor boundary intersection of the prediction regions. In contrast, although the LV apex is poorly displayed in the image, the initial candidate point shown in (c) defines landmark prediction regions located on the boundary of interest. The candidate point under investigation is therefore successfully selected as an initial point. The set of initial candidates selected for subsequent feature point search is shown in (d), which demonstrates that the method can

eliminate incorrect positions of the initial point despite the relatively poor appearance of the image. Similar performance can be seen in the 3D example in Figure 4.7. Unlike the original ASM, which is significantly affected at the basal region, the proposed method allows for accurate boundary localisation due to the use of inter-landmark constraints during initialisation and feature point search.

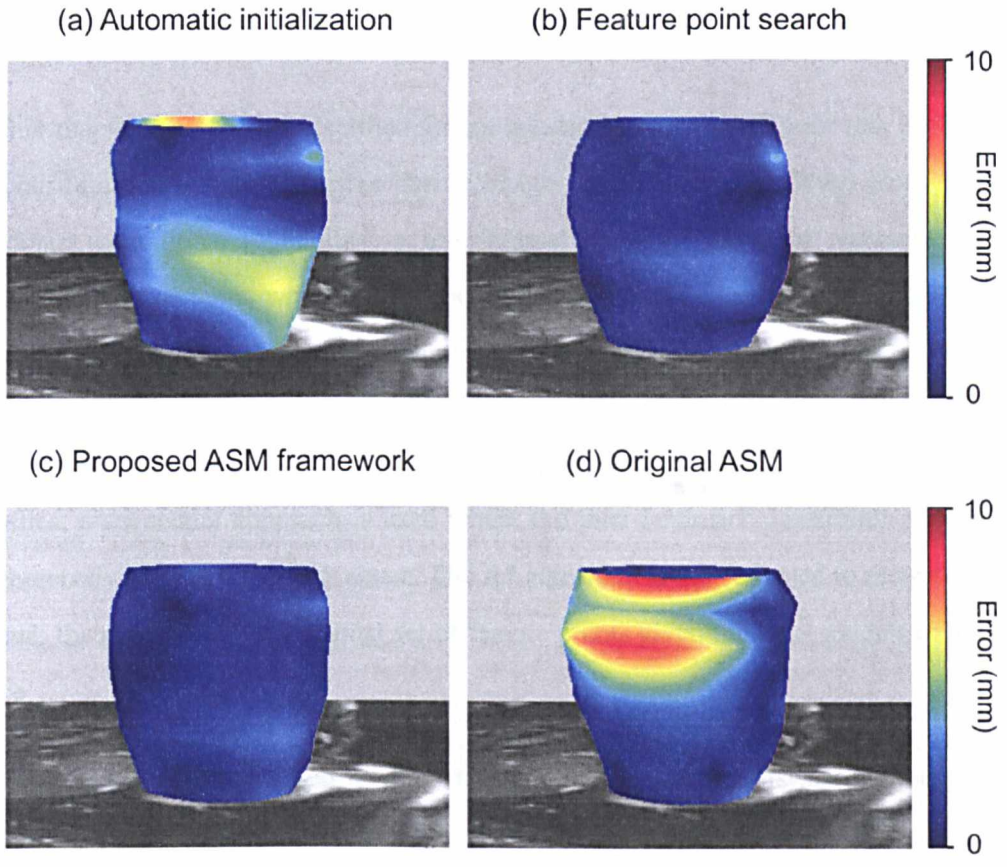

Figure 4.7 Illustration of volumetric segmentation results obtained with the proposed method. The surface localisation error shows satisfactory 3D initialisation (a), which is improved at the optimal feature search (b). The final result in (c) shows significant improvement when compared to the original ASM in (d).

Additional examples are shown in Figures 4.8 and 4.9, demonstrating the strength of the proposed approach for epi-cardial segmentation. In Figure 4.8, the original ASM is affected by difficulties in defining key anatomical features, thus introducing considerable errors. In Figure 4.9, it can be seen that the edge profiles are well defined at the septal region, resulting in a good performance of the original ASM in this region. At the lateral

region, however, the presence of large epi-cardial fat in Figure 4.9(a)) and the lack of strong edges (*e.g.*, Figure 4.9(c)) introduce many misplaced feature points for the original ASM. These problems are naturally avoided in the proposed algorithm, resulting in consistent epi-cardial borders irrespective of the quality of the datasets.

4.4 Discussion and Conclusions

In this chapter, a method is described for constructing a geometrical prior that can be used to constraint individual landmarks during image search. This is achieved through inter-landmark conditional probability, a translational invariant statistical representation of inter-landmark patterns, which assists the prediction of an unknown landmark by taking into account positions of other points in the shape. To improve the ASM output, a feature point search algorithm is introduced based on a combinatorial approach. With this method, instead of searching for feature points independently using conventional normal profiles, a sequential approach is used where the inter-landmark constraints are applied successively to limit the search space. The A* algorithm is then adapted to the problem to ensure the detection of the optimal set of feature points given the local models of appearance.

Automatic initialisation based on the inter-landmark constraints is also derived in this chapter. This is based on heuristics for estimating the degree of intersection of the landmark prediction regions with the boundary of interest. With the proposed method, unsuitable solutions are eliminated efficiently, allowing relatively fast and reliable initialisation of the ASM segmentation process. Initial values for scaling and rotations can also be efficiently extracted. Validation results for epi-cardial segmentation have shown considerable improvement of the proposed method compared to existing methods. The proposed method also eliminates the need for manual interaction, which for practical clinical applications improves the consistency and statistical significance of the segmentation results.

It should be noted, however, there are some limitations associated with the proposed approach. Firstly, despite the efficiency of the combinational approach used, the proposed

technique in its current implementation requires additional computation particularly during initialisation, which prohibits real-time and interactive shape localisation. On the other hand, the gain in robustness results in minimised user intervention, which reduces the overall analysis time in practical situations. Secondly, the inter-landmark conditional probabilities are translational invariant which permit landmark localisation without prior knowledge of their approximate locations within the image. The method, however, is not invariant to rotation and scaling. While initial values of these parameters can be estimated, it is important to note that any potential error can be propagated to the initialisation and feature point search, thus affecting the accuracy of the segmentation result.

In summary, this chapter illustrates the potential of ILDs for predicting landmark positions and imposing effective constraints for shape extraction. In the next chapter, a post-segmentation process will be introduced for analysing individual landmarks to evaluate their consistency with respect to the model. This enables the identification of segmentation errors and regional shape abnormality.

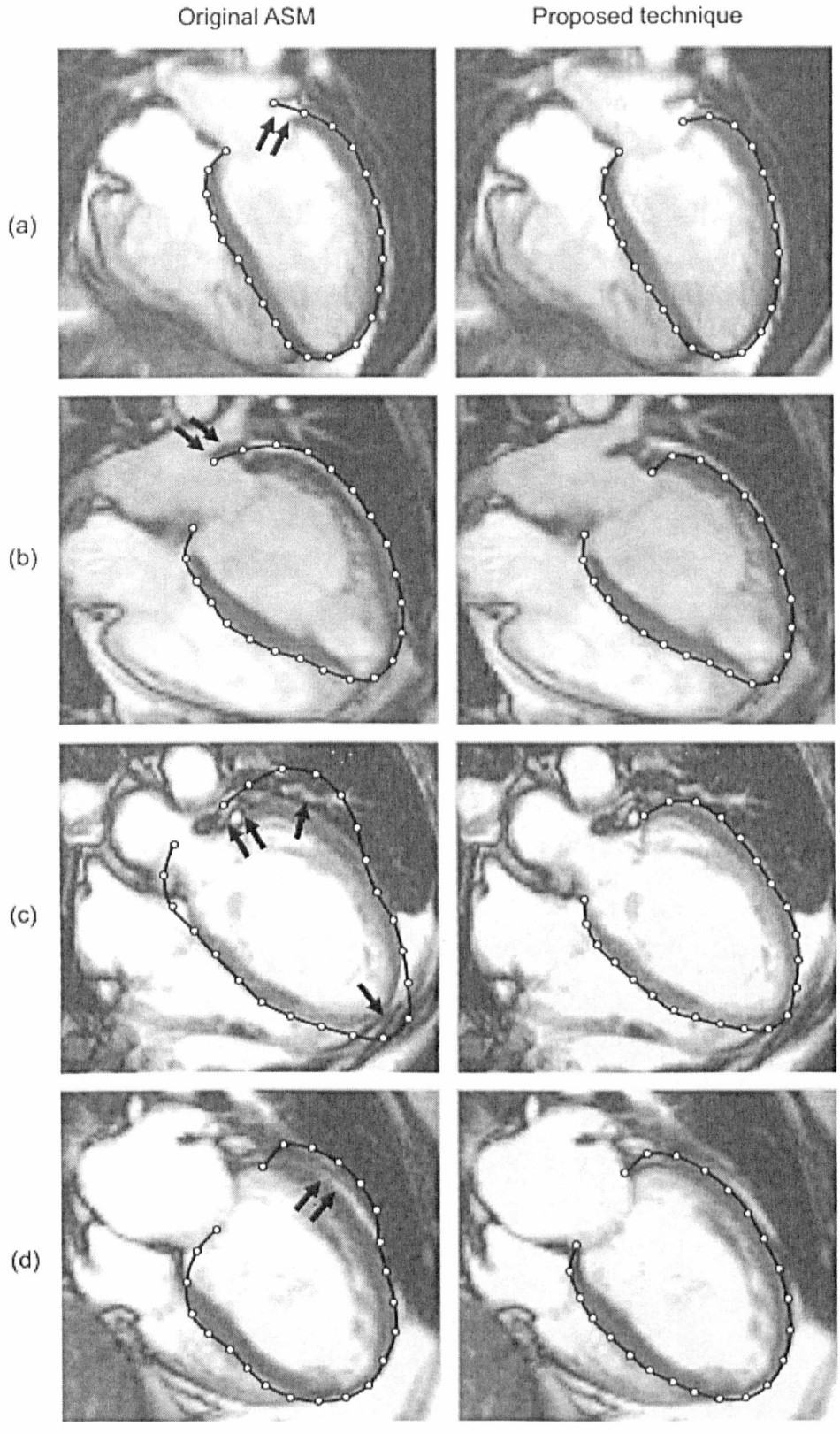

Figure 4.8 Examples of common errors in valve localisation by the original ASM, which are rectified by the use of the proposed automatic method and the statistical-based search regions.

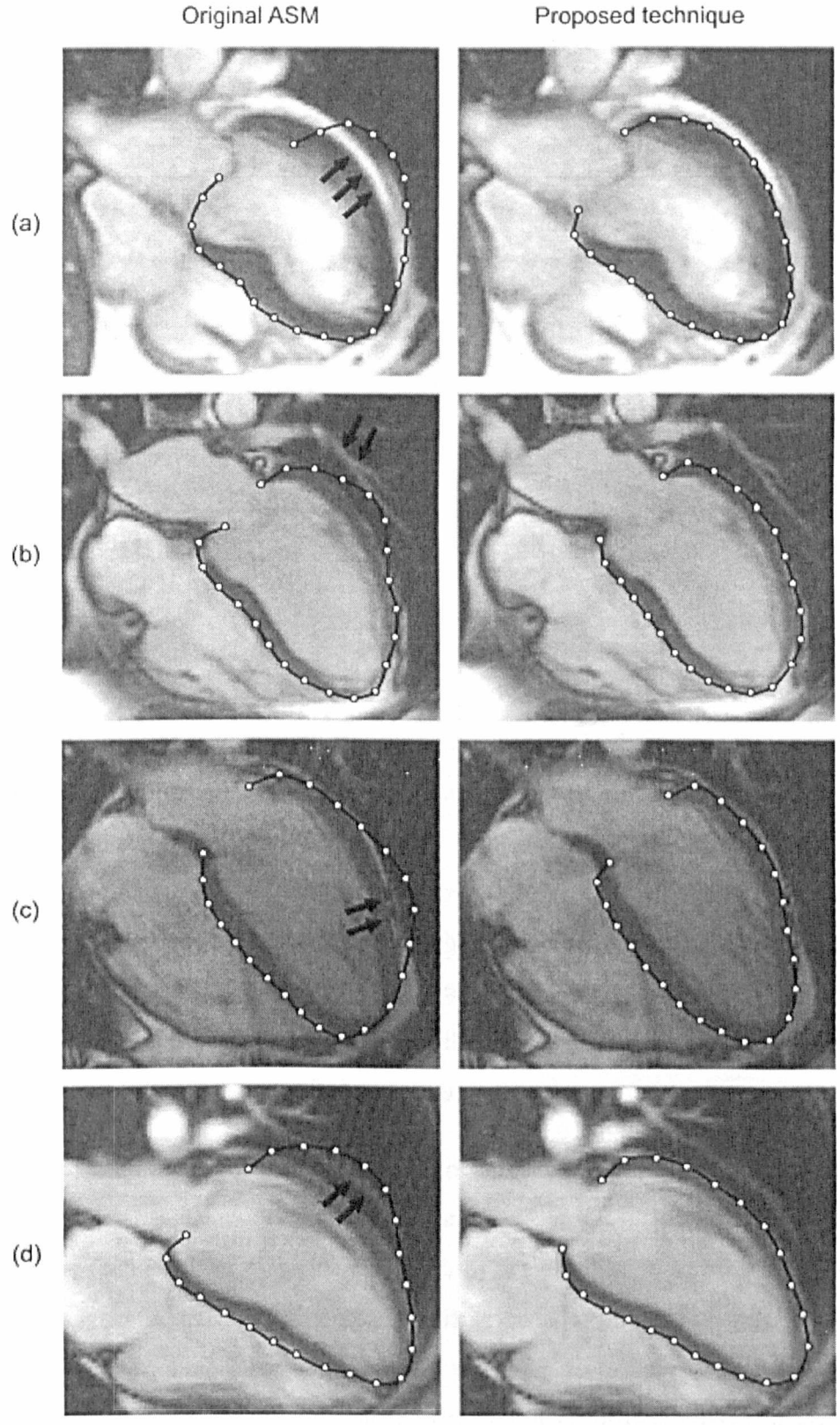

Figure 4.9 The effect of image inhomogeneities on shape localisation. In this case, the ASM is affected at the lateral region while the proposed technique due to the constrained feature point search allows for more accurate segmentation.

5

Inter-Landmark Analysis

5.1 Introduction

In the previous chapter, we have discussed the use of Inter-Landmark Descriptors (ILDs) for defining landmark constraints. Algorithms for shape initialisation and optimal feature point search in ASMs are derived, demonstrating increased robustness and reduced user interaction. In this chapter, a methodology based on ILDs is introduced for analysing the consistency of the landmarks and applied for outlier handling in ASMs*. In ASMs, for example, the presence of erroneous landmarks is inevitable. In cardiovascular imaging, image inhomogeneities can arise from a number of sources, including motion and flow induced structural noises. Generally, these artefacts are subject-specific and difficult to model. In normal ASM applications, these outliers can significantly influence the model fitting process if they are not handled adequately.

One of the solutions to outlier handling is to introduce an intermediate step between feature point search and model fitting. For example, Cootes *et al.* [109] have proposed to replace the traditional least squares approach by weighted least squares fitting where varying weights are assigned to each landmark to penalise points that are further away from the current model instantiation around the average. In the work of Rogers and Graham [62], the weights are calculated using robust estimators applied to the shape

* Results first published in IEEE Transactions on Medical Imaging, vol. 26(2), 2007.

residuals or by considering the inherent image information at the landmark points. Duta and Sonka [60] treat outliers as points that represent a large total shape variation and replace these points by the corresponding mean values of the shape model. In the work of Li and Chutatape [61], feature points located away from the current model beyond a predefined threshold are considered as outliers and subsequently rejected from the model fitting procedure.

The fundamental limitation shared by these methods are illustrated in Figure 5.1, in that they all rely on initial model fitting and shape superimposition before outlier detection. If the initial shape alignment is correct, the residuals can be analysed using a suitable method for outlier detection. It is evident from Figure 5.1 that the outliers also introduce a bias in the overall alignment of the model where large errors are minimised at a cost of increased residuals. In practice, it is more common to have clustered outliers, *i.e.*, errors that are localised within a group of neighbouring landmarks. In such situation, the superimposition results and overall performance of exiting techniques are further affected. The authors in [60] acknowledge difficulties with multiple outliers and improvement is reported in the method in [62] for only up-to 20% of outliers.

The examples shown in Figure 5.1 highlight the importance of effective decoupling of initial model alignment and outlier detection. To this end, a global alignment invariant outlier detection algorithm based on inter-landmark analysis is proposed in this chapter. The proposed method involves the use of inter-landmark distance ratio as an invariant shape metric. Statistical tolerance intervals are estimated from the training set for identifying extreme ILDs. Instead of rejecting or replacing the identified outliers by their corresponding mean values, the relative configuration of valid landmarks (inliers) is used with the tolerance model for suggesting replacement values. The proposed method also involves the propagation of geometrical prior gathered from the invariant descriptors during successive iterations for robust feature point detection. This limits the presence of outliers and improves the convergence of the segmentation process. The proposed technique is validated with 3D MR segmentation tasks involving contrastingly different image appearances, including the inner vessel lumen and outer vessel wall of the carotid artery, as well as the endo- and epi-cardial borders of the Left Ventricle (LV).

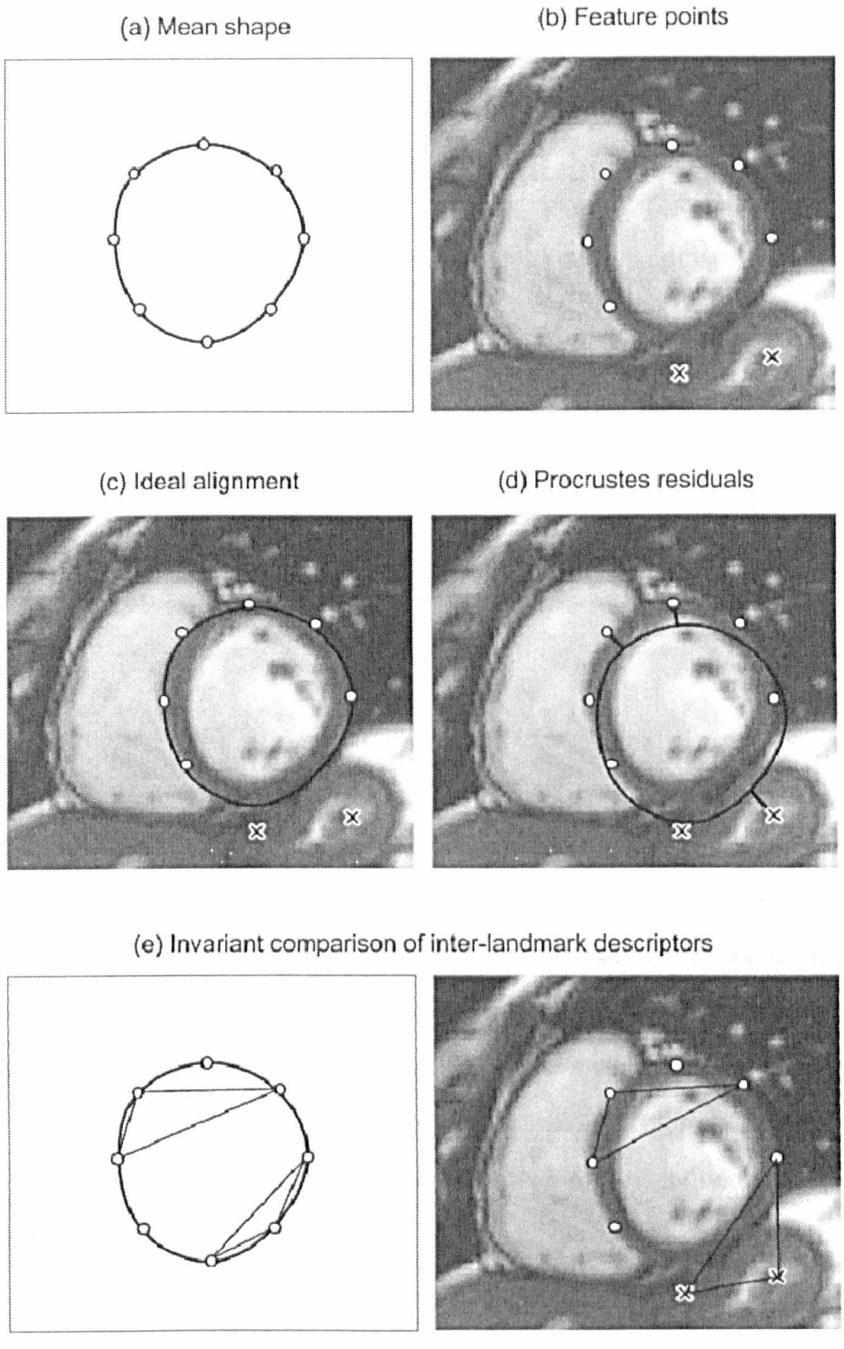

Figure 5.1 Outlier detection using residual analysis showing ideal shape alignment and Procrustes residuals caused by outliers. Through the use of invariant comparison of ILDs, these outliers can be reliably identified, and therefore removed from the shape fitting process.

5.2 Methods

5.2.1 Inconsistent Landmark Localisation

In this section, the generic formulation of the inconsistent landmark localisation algorithm is presented. Given an extracted set of n landmark points, two important ingredients need to be defined. First, an appropriate ILD needs to be selected depending on the application. Subsequently, a set of K_i ILDs can be associated with each point p_i and their values are analysed in order to detect potential inconsistencies. For each ILD r, an inter-landmark consistency measure f_d is defined as a Boolean function that describes consistency or inconsistency depending on the value of r, *i.e.*,

$$f_d(r) = \begin{cases} 1 & r \text{ is consistent} \\ 0 & \text{otherwise.} \end{cases} \tag{5-1}$$

The ultimate aim of the algorithm is to identify inconsistent landmarks, but this is not straightforward to infer from the inconsistency of a particular inter-landmark value. This is because by definition the ILD is associated with multiple landmarks, each potentially the source of the inter-landmark inconsistency. To address this difficulty, we therefore use the observation that inconsistent landmarks are typically associated with more inconsistent ILDs than any other points in the shape. Therefore, a point consistency measure f_p can be derived for each landmark by integrating all individual inter-landmark consistency costs as follows:

$$f_p(p_i) = \frac{1}{K_i} \sum_{k=1}^{K_i} f_d(r_k). \tag{5-2}$$

The calculated f_p measures for all landmarks are stored in a priority queue and an iterative algorithm is used to identify inconsistent points. At each step, the first point in the queue, *i.e.*, the point p_k with the lowest point consistency measure is identified as being inconsistent and removed:

$$p_k = \arg\min_{p_k} \left[f_p(p_k) \right]. \tag{5-3}$$

The f_p measures for the remaining points in the queue are updated by subtracting the contribution of the rejected point. The points are then reordered in the priority queue for identifying the next inconsistent point and the procedure is repeated until the first point in the queue has a point consistency measure that is equal or close to 1. This indicates the associated ILDs are valid, including those of the remaining points in the queue.

5.2.2 Outlier Detection

The proposed outlier handling method is based on the use of an invariant shape metric, and therefore does not depend on initial shape alignment which is difficult to achieve in the presence of outliers. The ratio of inter-landmark distances as introduced in Chapter 3 is used for this purpose. In addition to being fully invariant to scale, translation and rotation, the ratio of distances has other properties that make it ideal for outlier analysis. Firstly, it represents the relative geometrical configuration of landmark points, thus each point can be analysed with regard to the position of other points in the shape. Secondly, it allows a subdivision of the shape into subsets of points, with the aim of distinguishing the subset of erroneous points from the inliers. In each triplet of points, six different ratios can be derived, but by the use of symmetry only three are considered here. With K triplets, the object can be represented by using the following vector:

$$R = (r_1, \ldots, r_k, \ldots, r_{3K}). \tag{5-5}$$

The main advantage of this descriptor is its ability to perform as a geometrical measure for shape comparison, and thus can be used as a local shape dissimilarity metric for detecting subsets of the shape that are inconsistent with the model. We show in the next section how to construct such a model and calculate the associated dissimilarity likelihood measures.

With the invariant shape metric presented above, each landmark is associated with a set of ratios. The idea behind the proposed method is that the outliers are inconsistent with the corresponding landmark points in the training samples, and thus some of the associated ratios are invalid. The first step of the process is to find a suitable definition for extreme or invalid ratios. This can be achieved by using the tolerance intervals introduced

in Chapter 3. Statistical tolerance intervals T_{ijk} are calculated from the training samples for each variable r_{ijk} and any new ratio found outside of the interval is considered as an extreme value, which indicates the presence of an outlier.

The exhaustive use of all $n(n-1)(n-2)/6$ possible ratios to build the shape vector in (5-5) can be time consuming. Moreover, some of the ratios can be calculated from uncorrelated landmarks, resulting in large tolerance intervals that are not useful, or even detrimental to outlier detection. As suggested in Section 3.3.4, it is beneficial for statistical-based shape analysis to select ILDs of statistical significance. In Chapter 4, for example, the inter-landmark conditional probabilities with the smallest covariance are selected for imposing landmark constraints. For outlier handling, the proposed approach is to select for each landmark P_i at least K_0 ratios that have the smallest average intersection of the tolerance intervals with the local search window L_i based on the training samples. These selected ratios are ideal for outlier detection as they can capture movements of the point from its correct location.

By using the tolerance interval, a likelihood measure f_r is calculated for each ratio r_{ijk} to detect extreme values due to potential outliers. Typically, this measure is equal to 1 if the ratio is within the tolerance interval and 0 otherwise:

$$f_r\left(r_{ijk}\right) = \begin{cases} 1 & \text{if } r_{ijk} \in T_{ijk} \\ 0 & \text{elsewhere.} \end{cases} \tag{5-6}$$

With the definition of the consistent ratio function in Equation (5-11), it is now possible to calculate the point consistency measure in Equation (5-3) by using the iterative algorithm described in the previous section. The terminating threshold for the iterative outlier detection procedure corresponds to the minimal proportion of valid ratios for each inlier. It was found that by choosing any limit that is close to the confidence coefficient γ, similar results can be achieved. This is because the main outliers are detected well before reaching this limit, whilst the same level of uncertainty is given to both tolerance interval calculation and outlier detection. The outlier detection algorithm is illustration with a simple shape as an example in Figure 5.2.

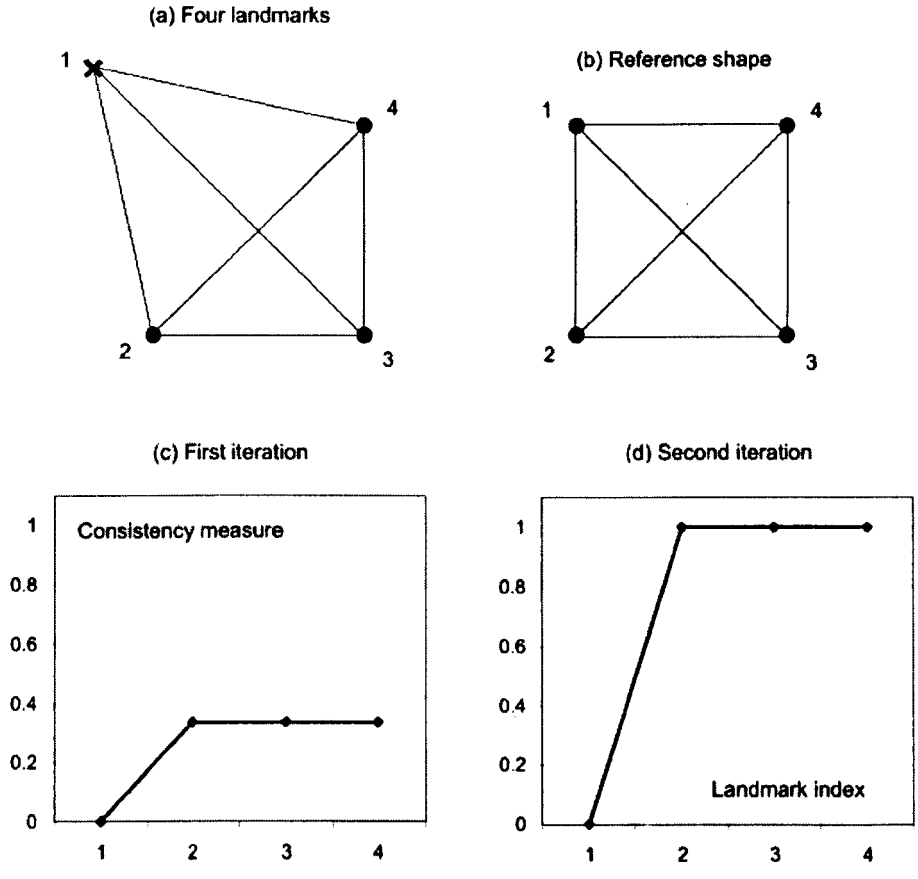

Figure 5.2 Illustration of the proposed outlier detection algorithm for a simple shape. For landmark 1, all the ILD ratios are invalid (123, 134 and 124) and therefore its consistency measure is equal to 0 (0/3). For all other landmarks, only ILD ratios associated with 234 are valid, their consistency measure is therefore equal to 1/3. At the second iteration and after rejection of landmark 1, the consistency measures for points 2-4 are updated and their values equal 1 (1/1). At this point, the outlier detection process is completed.

5.2.3 Outlier Correction

Once the outliers are detected, their positions must be adjusted so as to eliminate their influence on ASM model fitting. A replacement point must be selected from the initial candidate points in the local search window L_i within the image space such that its associated ratios with respect to the inliers are close to or within the corresponding tolerance intervals. This is equivalent to maximising the product of the p.d.f. of the ILD ratios. The function to be maximised is therefore proportional to:

$$\prod_{j,k\in I} \frac{1}{s_{ijk}\sqrt{2\pi}} \exp\left(-\frac{\left(r_{ijk}-\overline{r}_{ijk}\right)^2}{2{s_{ijk}}^2}\right). \tag{5-7}$$

The problem can now be reduced to selecting the point that minimises the following least-squares function:

$$\sum_{j,k\in I}\left(\frac{r_{ijk}-\overline{r}_{ijk}}{s_{ijk}}\right)^2 = \sum_{j,k\in I}\left(\frac{d_{ij}-d_{jk}\overline{r}_{ijk}}{d_{jk}s_{ijk}}\right)^2. \tag{5-8}$$

The value suggested by the above step by using the geometrical information represents a good approximation of the true boundary position but may not fit optimally to the underlying image evidence. Therefore, a final local search in the vicinity of the candidate position is required by using the grey-level information. Computationally, only a few candidate positions around the current point are considered at this stage (h_c positions from either side of the point, $h_c = 2$ in the experiments). After this adjustment, more reliable ASM model fitting can be achieved. Figure 5.3 shows a simple illustration of the

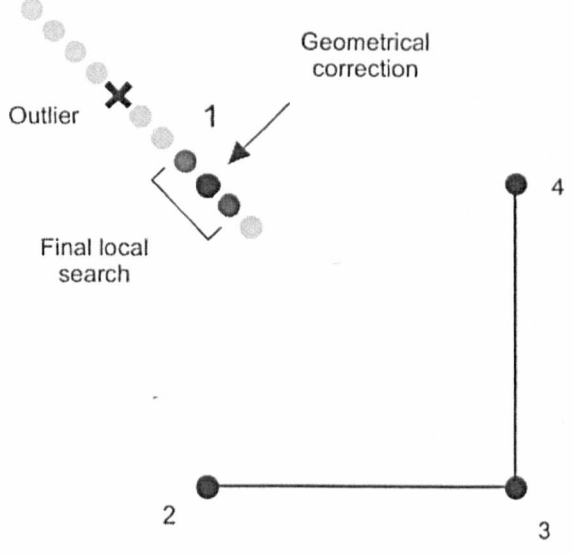

Figure 5.3 Illustration of the main steps involved in outlier correction. A geometrical-based replacement is first suggested from the initial search profile by using the tolerance model and the positions of valid feature points 2, 3 and 4. A final local search based on grey-level appearance information is carried out for geometrical correction.

outlier correction step.

5.2.4 Geometrically Weighted Feature Search

To prevent outliers from reappearing during subsequent feature point search, the grey-level based fitness measure is weighted by a function w that is calculated by using the geometric information gathered during outlier detection. The total fitness measure becomes:

$$f_{total}(P_i) = d_g(P_i)\, w(P_i) \tag{5-9}$$

where d_g is the grey-level based distance measure to maximise. By using set I of inliers, a geometric likelihood measure is drawn for each search position in the local search window L_i as follows:

$$f_g(P_i) = \frac{1}{K_i} \sum_{j,k \in I} f_r(r_{ijk}) f_r(r_{jki}) f_r(r_{kij}) \tag{5-10}$$

where K_i is the number of triplets associated with P_i. This function describes the degree of intersection of the different tolerance intervals and takes a value between 0 and 1. By setting $w = f_g$, the region around the true boundary is heavily weighted and the weight decreases for regions that are further away. Figure 5.4 illustrates an example of a feature point search, where the normalised cross correlation is used as the grey-level fitness measure. In this example, local search based on grey-level information alone generates an outlier due to a local maximum located at an incorrect boundary position as shown in Figure 5.4(a). By combining the geometric likelihood measure as shown in Figure 5.4(b), the total weighted cost function of Figure 5.4(c) permits the localisation of the correct maximum position for the feature point.

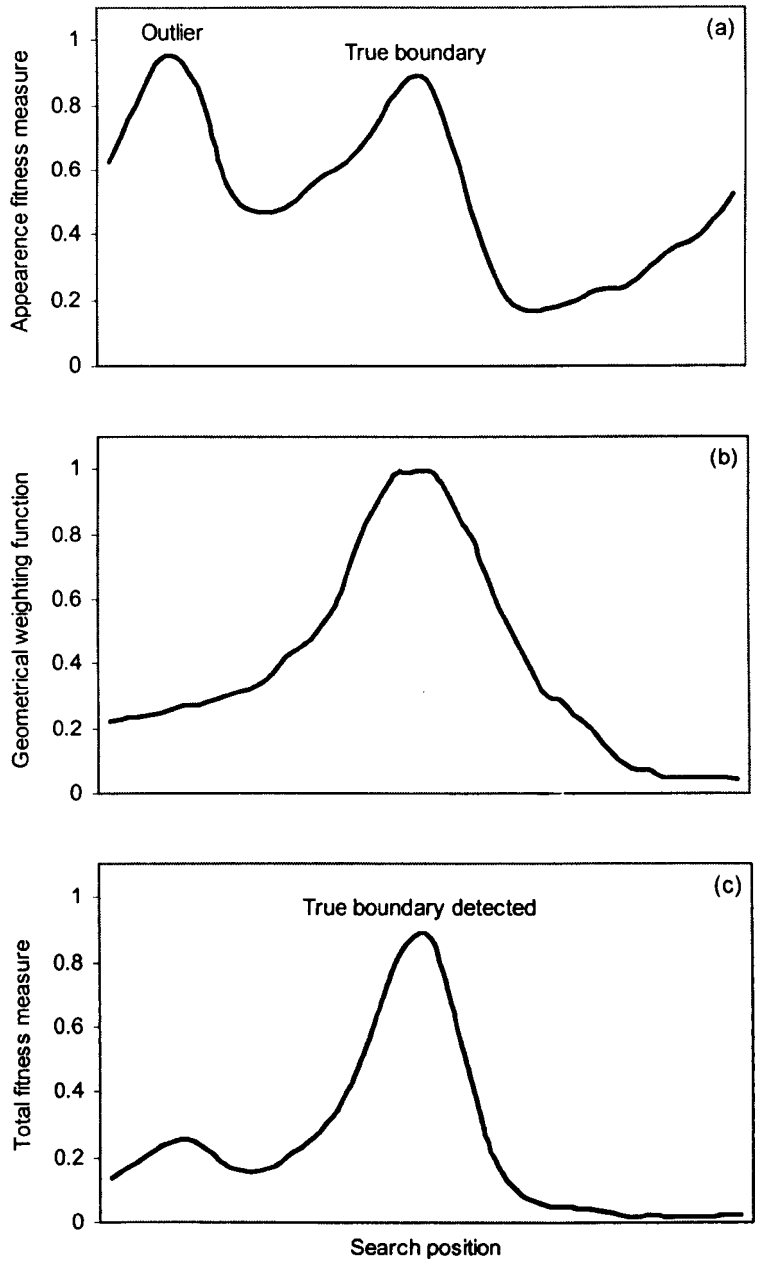

Figure 5.4 An example of a feature point search where an outlier is avoided by using the geometrically weighted fitness measure. Local search based on grey-level information alone generates an outlier due to a local maximum located at an incorrect boundary position as shown in (a). By combining the geometric likelihood measure plotted in (b), the total weighted cost function in (c) permits the localisation of the correct maximum position for the feature point.

It is also possible to limit the extent of the local search by considering only positions in the search window with a high geometric likelihood value beyond a predefined threshold l_g. In this case, the weights are calculated as follows:

$$w(P_i) = \begin{cases} 1 & \text{if } f_g(P_i) > l_g \\ 0 & \text{otherwise.} \end{cases} \tag{5-11}$$

Setting $l_g = 0$ is equivalent to using the entire local search window. In general, the true boundary position lies in a region of geometric likelihood value that is close to the maximum value of f_g within the local search window. Therefore, choosing $l_g = \max(f_g) - \delta_g$ (with δ_g a small number, equal to 0.02 in the experiments) allows the window to be increasingly restricted after each iteration. This significantly limits the presence of outliers, thus permitting the final convergence of the algorithm within a few iterations. This combined fitness measure is mainly required for difficult image search tasks with a high level of outliers (more than 20%), but can be omitted otherwise to decrease the time complexity of the segmentation procedure.

5.3 Validation

5.3.1 Experiments

The validation of the proposed technique is carried out for the segmentation of the endo- and epi-cardial borders of the LV, as well as the luminal and outer walls of the carotid artery. These two datasets have distinctively different intensity appearance, topological and geometrical structures. The lumen of the carotid artery tends to have strong edges but is frequently affected by residual blood flow artefacts. The outer vessel wall, on the other hand, usually has a poor contrast to the surrounding structure and therefore is particularly difficult to localise.

Table 5.1 Parameters of the segmentation framework used in the experiments.

Parameter		Carotid	LV
n	Number of landmarks	272	136
N	Number of datasets	40	36
	Part of shape variation explained by the statistical models	0.99	0.99
	Bounds on eigenvalues	3	3
h_p	Grey-level profile length on either side of the landmark point	7	7
h_s	Local search size on either side of the current point	10	10
h_c	Final search size for outlier correction on either side of the point	2	2
	Profiles step size (mm)	0.2	1.5
	Maximum number of iterations for the ASM search	100	100
	Convergence threshold (mm)	0.05	0.2
β	Statistical tolerance intervals coverage coefficient	0.99	0.99
γ	Statistical tolerance intervals confidence coefficient	0.95	0.95
K_0	Minimum number of ratios per point in the tolerance model	200	200
k_2	Two-sided tolerance intervals factor	3.22	3.27
l_d	Threshold for terminating the iterative outlier detection	0.95	0.95
δ_c	Threshold for the geometrically weighted fitness measure	0.02	0.02

The carotid artery datasets were collected from 40 subjects using a 1.5T MR scanner (Sonata, Siemens, Erlangen Germany) with a purpose-built two element phased-array surface carotid coil and a specially designed head and neck cushion for immobilisation. A 3D volume-selective TSE sequence [110] was used with a pixel size of 0.47 mm and slice thickness of 2 mm. For each dataset, 20 slices around the bifurcation were selected as a region for measurement. For the LV datasets, 36 subjects were scanned using the same scanner and a TrueFISP sequence (TE = 1.5 ms, TR = 3 ms, slice thickness = 10 mm, pixel size of 1.5 to 2 mm) within a single breath-hold.

For all the datasets used for this study, manual delineation was carried out by an expert observer as the ground truth reference. The statistical shape model was built for each case with simple point correspondences by using the parameters listed in Table 5.1. In all experiments, the iterative ASM procedures are terminated when the change between two successive iterations is below a convergence threshold which is specified in Table 5.1. The datasets used for grey-level appearance and tolerance model construction and evaluation were selected on a leave-one-out basis. For comparison, the proposed method was compared to existing ASM techniques (Original ASM by Cootes *et al.* [5] and those by Rogers and Graham [62], Duta and Sonka [60], and Li and Chutatape [61]) by using the same parameters as shown in Table 5.1. All techniques were initialized by placing the mean shape at the centre of the target structures based on the manual delineations. The segmentation error was measured by calculating the absolute point-to-surface distance from each final point to the corresponding manual delineation.

5.3.2 Numerical Validation

The performance of the technique with respect to different levels of outliers, both in terms of amplitude and percentage, was first assessed with synthetic outliers introduced to the manual delineation of the carotid datasets. This was achieved by perturbation of randomly selected points using non-Gaussian noise. In the first experiment, the percentage of outliers was fixed to 25% of the total number of landmarks while the amplitude varied from 0 to half of the average vessel diameter.

In the second experiment, the percentage of the outliers generated from the manual delineations varied from 0 to 50% and the standard deviation of the perturbation was fixed to 25% of the average vessel diameter. The generated points were used as feature points for a single iteration of the ASM search with the proposed outlier handling technique. The experiment was repeated 10 times, each with different random perturbation.

The reliability of the proposed outlier detection algorithm was measured by considering the number of false outlier/inlier identification by using the following measure:

$$1 - 0.5\left(\frac{\text{missed outliers}}{n_o} + \frac{\text{false outliers}}{n - n_o}\right) \tag{5-12}$$

where n_o is the number of outliers introduced. The outlier detection step was applied to the synthetic feature points for each sample and the average reliability together with one standard deviation error bars are plotted against the amplitude and the percentage of the outliers in Figure 5.5(a). The results show that the proposed outlier detection algorithm can distinguish the outliers from valid points with a consistently high reliability, despite the extent and the number of outliers involved. This is important as the performance of the subsequent ASM model fitting relies heavily on the correct identification of the outliers.

In Figure 5.5(b), the segmentation errors after one iteration of the ASM search by using the proposed outlier detection and correction algorithms are plotted against the amplitude and the percentage of the outliers. The relatively flat curves of the figure indicate that the accuracy of the method is independent of the amplitude of the outliers and the accuracy is maintained for up-to 50% of erroneous feature points, thus demonstrating the robustness of the method proposed.

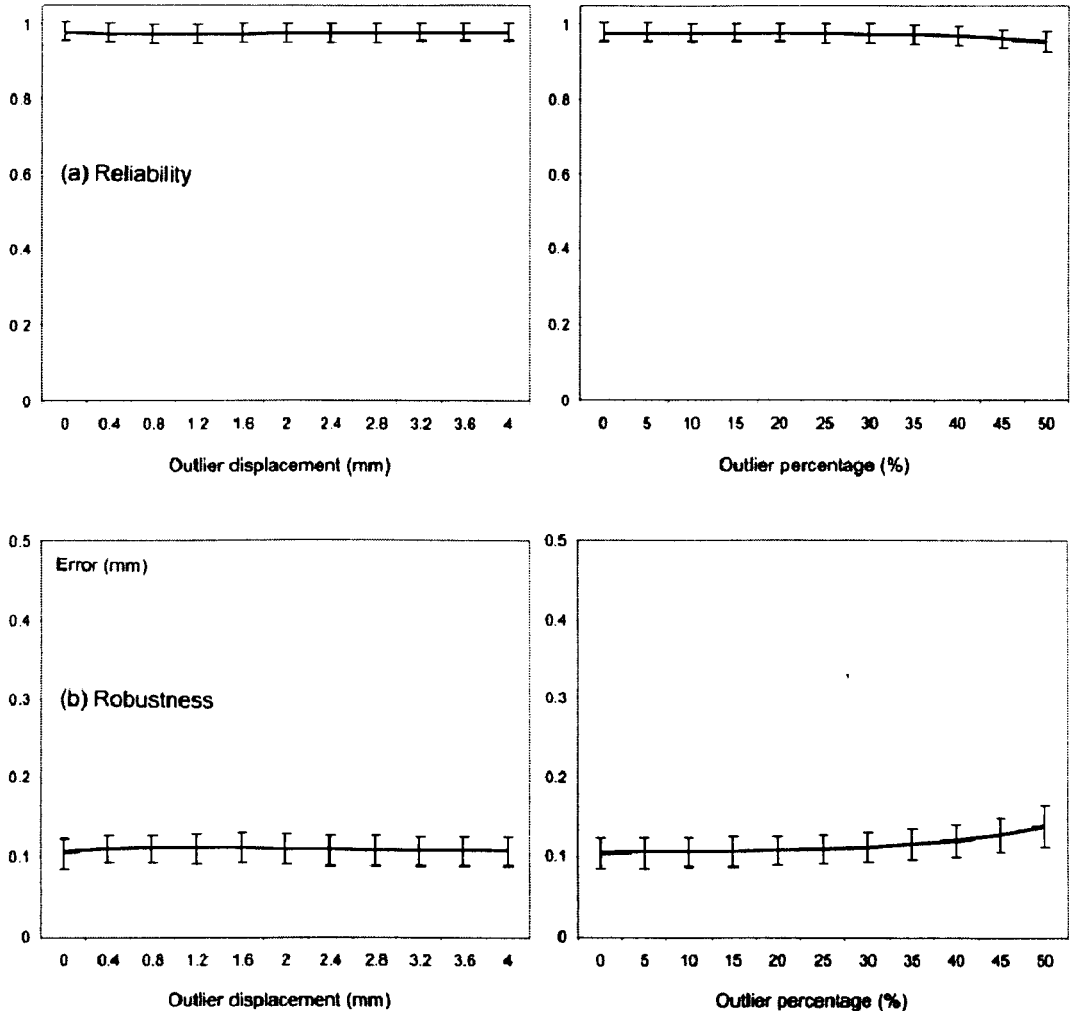

Figure 5.5 Results of the simulation study to evaluate the reliability (a) and robustness (b) of the proposed outlier detector in response to different amplitudes and percentages of the outliers.

5.3.3 *In vivo* Validation

For *in vivo* validation, the average and standard deviation of the segmentation errors are plotted in Figure 5.6 for the carotids and LV datasets. The corresponding results by using the existing ASM approaches are also provided for comparison. It can be seen from the graphs that the proposed technique outperforms all of the existing ASM methods, particularly for the segmentation of the outer vessel walls and epi-cardial borders, as they are more prone to outliers due to poorer contrast against the surrounding structures and a low intrinsic signal-to-noise ratio.

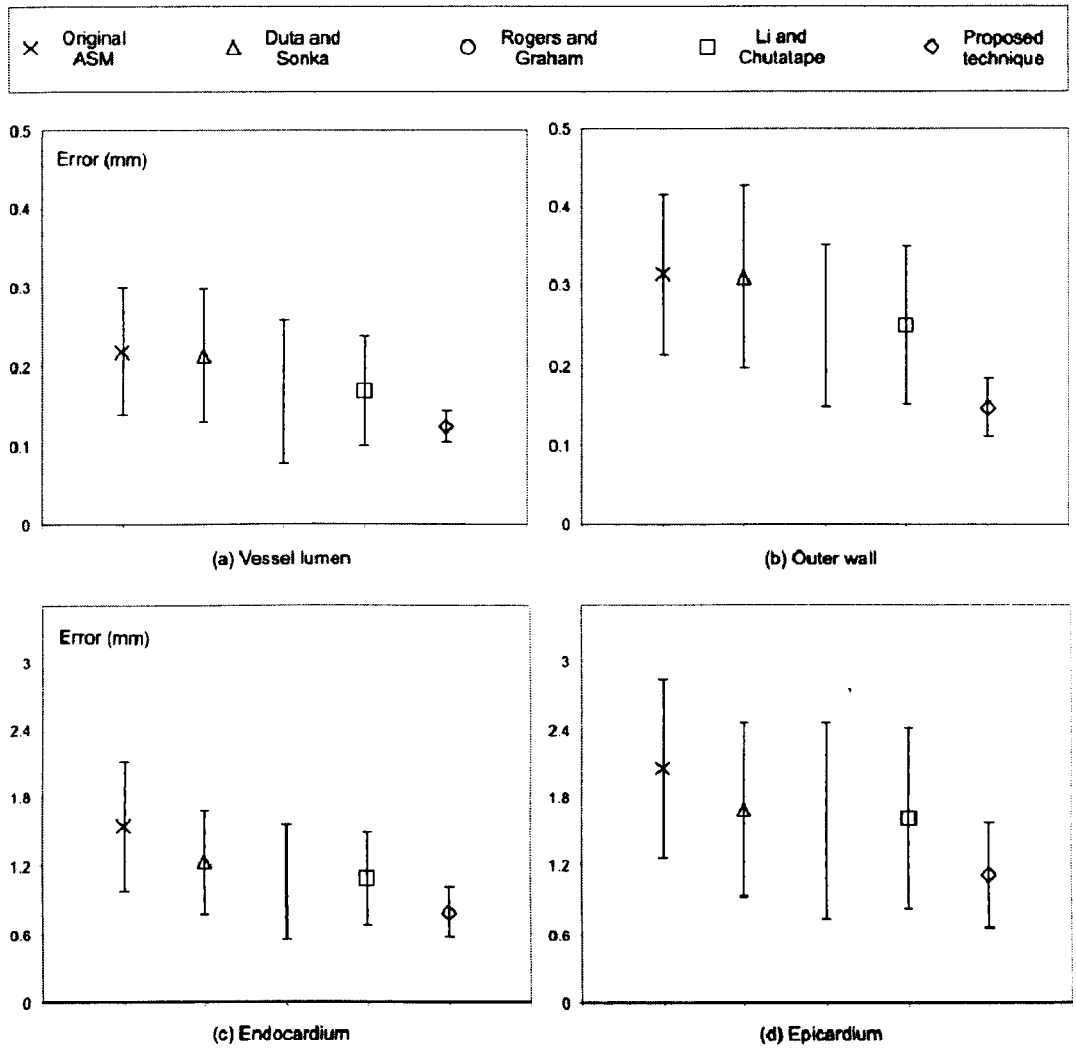

Figure 5.6 The accuracy of the proposed segmentation framework when applied to the different datasets and compared to existing robust ASM methods. The proposed technique outperforms the existing ASM approaches, especially for the outer wall of the carotid arteries and the epi-cardial border of the LV.

Table 5.2 provides a detailed assessment of each step involved in the proposed segmentation framework. In particular, it can be seen that the outlier correction stage improves the position of the feature points before the application of the ASM model fitting procedure. It is also clear from the results presented in Table 5.3 that the use of the geometrically weighted feature detection significantly reduces the percentage of erroneous feature points, and therefore enhances the stability of the algorithm by minimising the reoccurrence of the outliers during the iterative segmentation process.

Table 5.2 Detailed error analysis of the main steps involved in the proposed technique.

	Error (*mm*) feature point search	Error (*mm*) outlier correction	Final segmentation error (*mm*)	
			Using proposed method	Best results from existing methods
Vessel lumen	0.29 ± 0.09	0.16 ± 0.02	0.12 ± 0.01	0.16 ± 0.06
Outer wall	0.32 ± 0.06	0.19 ± 0.03	0.14 ± 0.03	0.25 ± 0.10
Endocardium	2.09 ± 0.62	1.25 ± 0.55	0.78 ± 0.21	1.05 ± 0.50
Epicardium	2.42 ± 0.82	1.52 ± 0.46	1.11 ± 0.46	1.59 ± 0.86

Table 5.3 Detailed performance of the proposed geometrically weighted cost function.

	% outliers (grey-level fitness measure)	% outliers (combined cost function)
Vessel lumen	14.8 ± 5.8	4.1 ± 3.3
Outer wall	16.0 ± 5.7	3.2 ± 3.5
Endocardium	22.3 ± 10.6	6.4 ± 7.9
Epicardium	31.0 ± 9.7	9.5 ± 6.6

Figures 5.7 to 5.9 illustrate the boundary localisation results for varying amount of outliers, demonstrating the improvement achieved by using the proposed outlier handling algorithm and its ability in dealing with both the number and distribution of the erroneous points. In particular, the proposed method performs well in the presence of clustered outliers (Figure 5.8) as the invariant metric used represents the global relative positions of the points, *i.e.*, each point can be analysed with respect to the position of other landmarks in the entire shape (not only in a localised region). For detailed visual assessment in 3D, Figure 5.10 to 5.13 show volumetric illustrations of the performance of the proposed outlier handling framework for varying levels of outliers. It can be seen that in all cases,

the ASM search alone introduces significant errors, especially in regions with localised outliers, *e.g.*, around the bifurcation point of the carotid artery. In contrast, the proposed technique returns accurate and consistent segmentations, even in the presence of significant amount of outliers (*e.g.*, Figures 5.11 and 5.13).

Finally, Table 5.4 shows the convergence behaviour and time complexity of the proposed method as compared to existing ASM methods. It can be seen that with the proposed technique, convergence was generally reached within 25 iterations of the segmentation process for over 90% of the datasets, demonstrating the stability of the method. With the proposed method, although the time spent on each individual iteration is longer than that of the original ASM, the results show that the overall time complexity of the method is in fact better than the existing ASM methods used for comparison.

Table 5.4 Convergence properties and time complexity of the proposed technique.

ASM method	Carotid outer wall datasets			LV epicardium datasets		
	within 25 iterations (%)	max. iterations (%)	Average time (seconds)	within 25 iterations (%)	max. iterations (%)	Average time (seconds)
Original ASM	7.5	67.5	2.2 ± 0.6	8.3	88.8	1.1 ± 0.3
Duta and Sonka	20.0	55.0	2.4 ± 1.0	11.1	36.8	1.1 ± 0.4
Rogers Graham	47.5	15.0	1.5 ± 1.1	41.6	11.1	0.9 ± 0.7
Li and Chutatape	42.5	7.5	1.4 ± 0.7	36.1	30.5	0.7 ± 0.5
Proposed technique	97.5	0	0.8 ± 0.3	91.6	0	0.5 ± 0.2

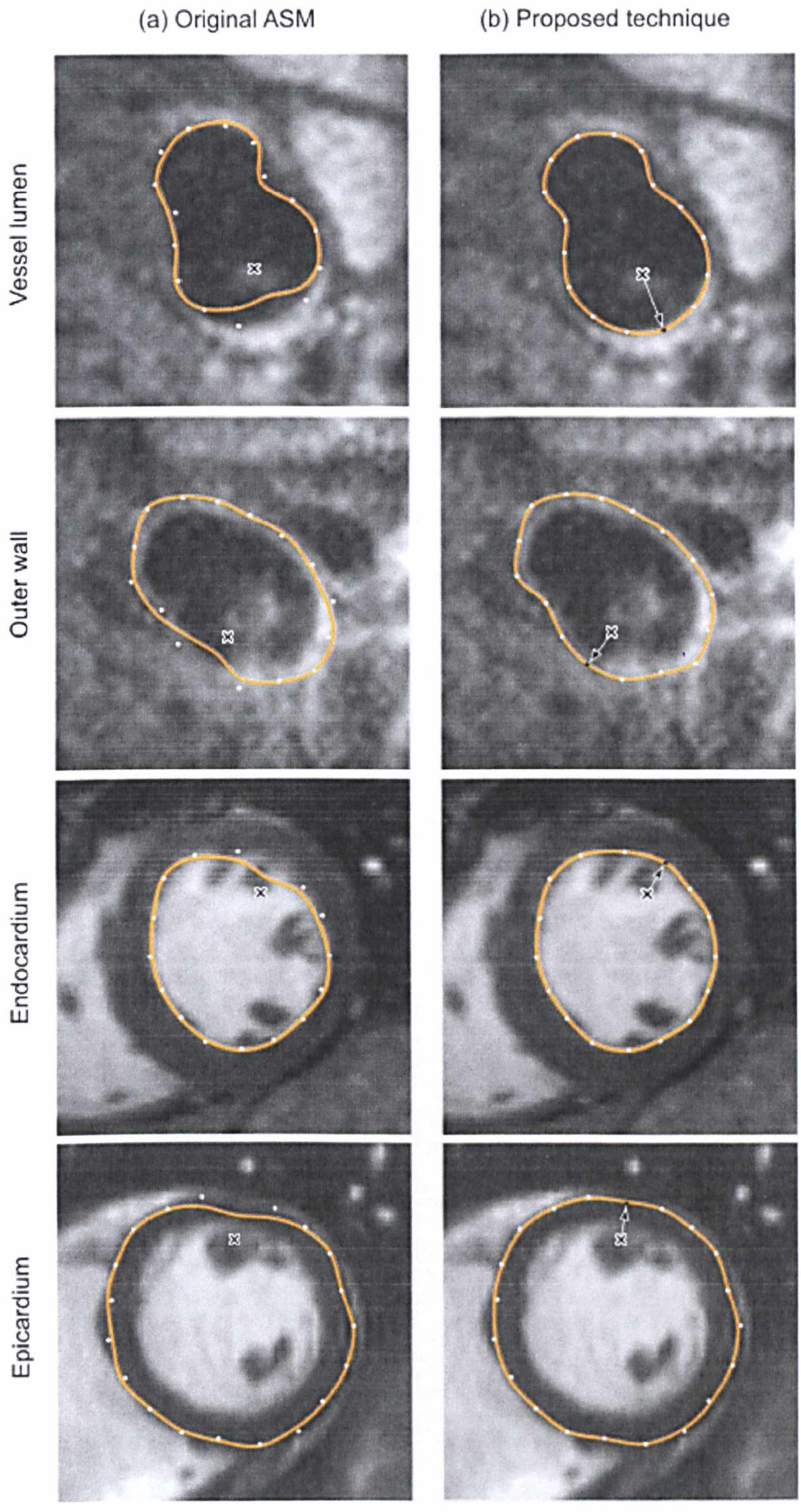

Figure 5.7 Relative performance of the original and the proposed ASM with a single outlier.

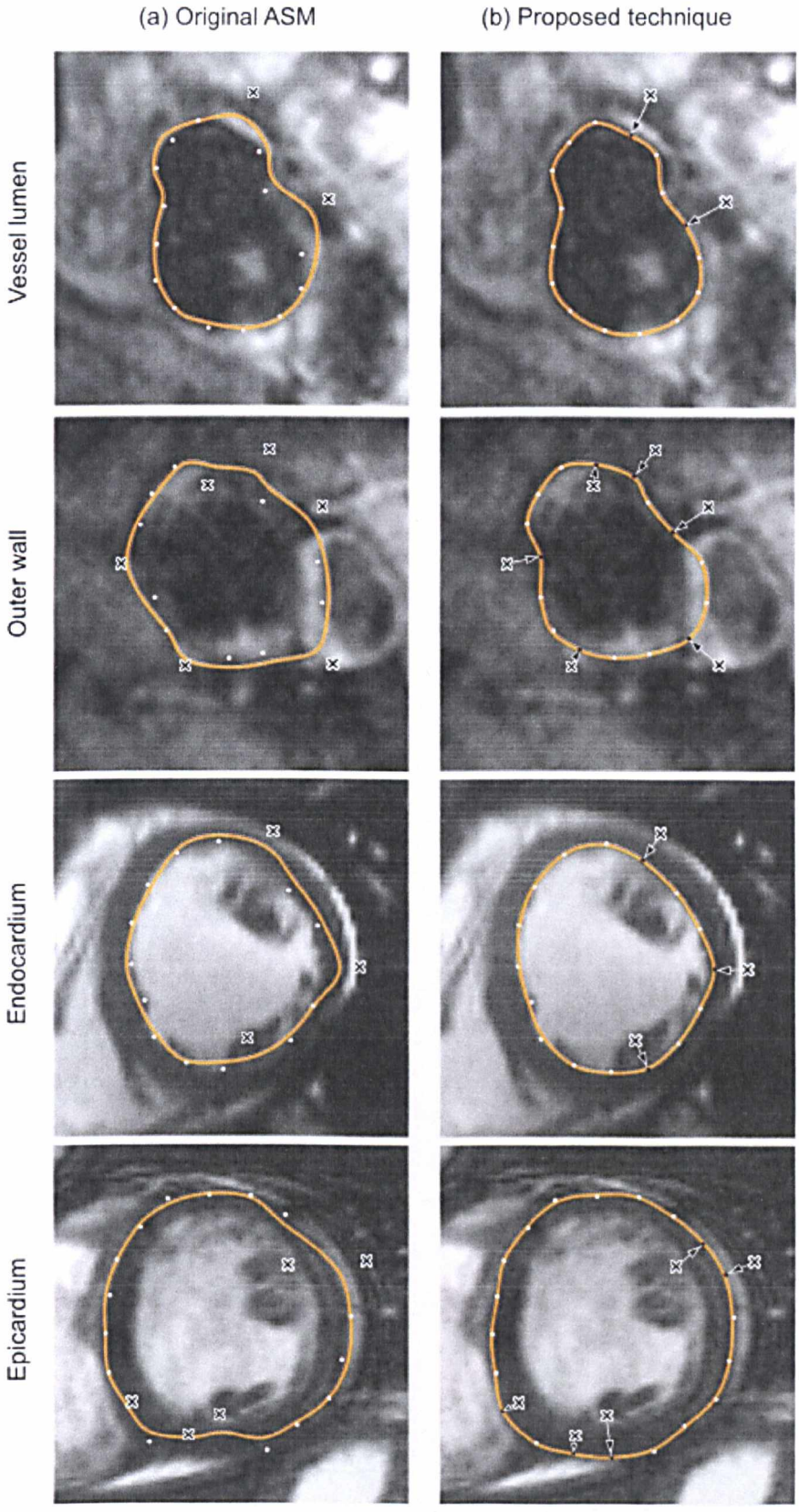

Figure 5.8 Relative performance of the original and the proposed ASM with distributed outliers.

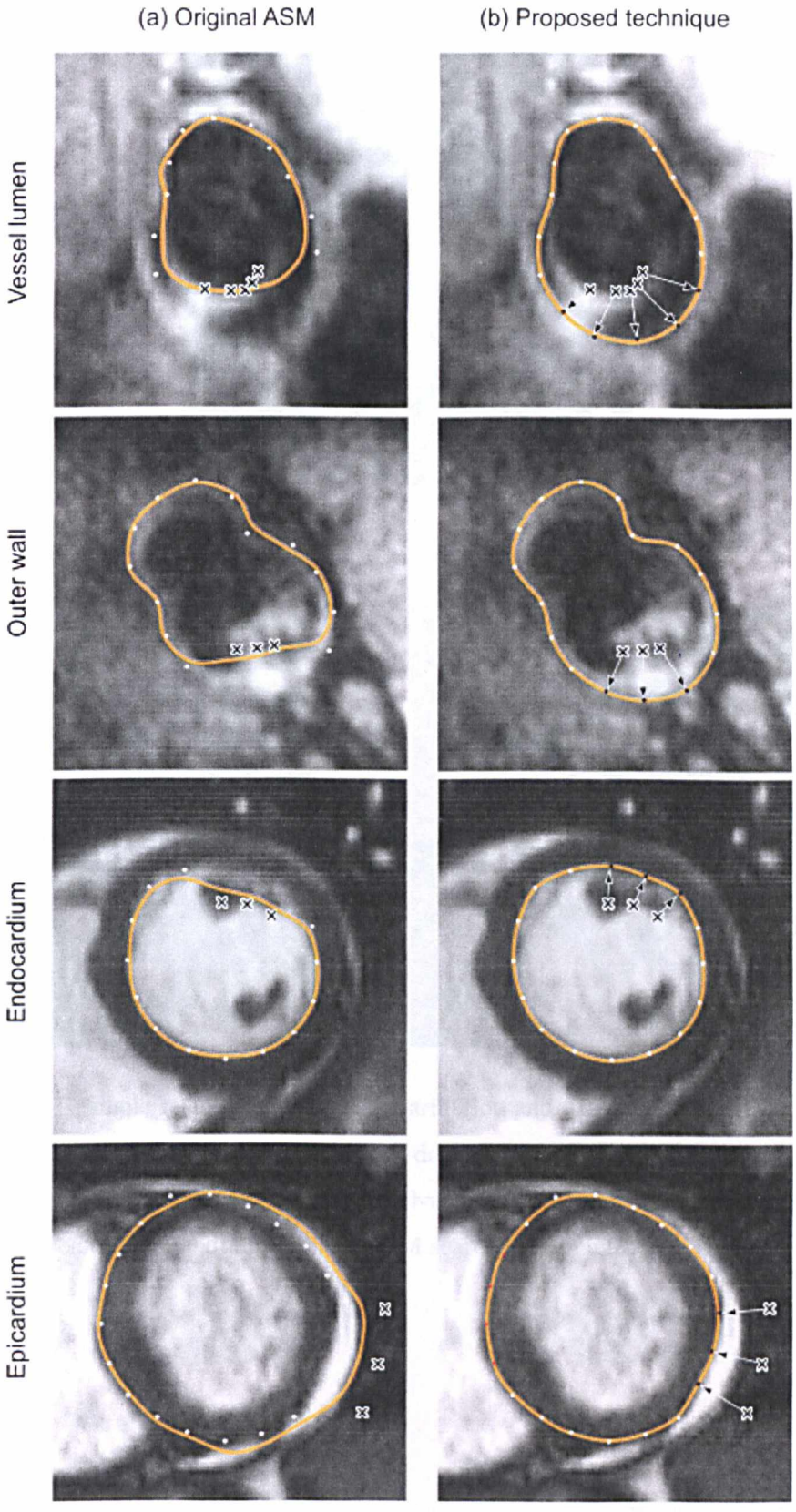

Figure 5.9 Relative performance of the original and the proposed ASM when encountered with clustered outliers.

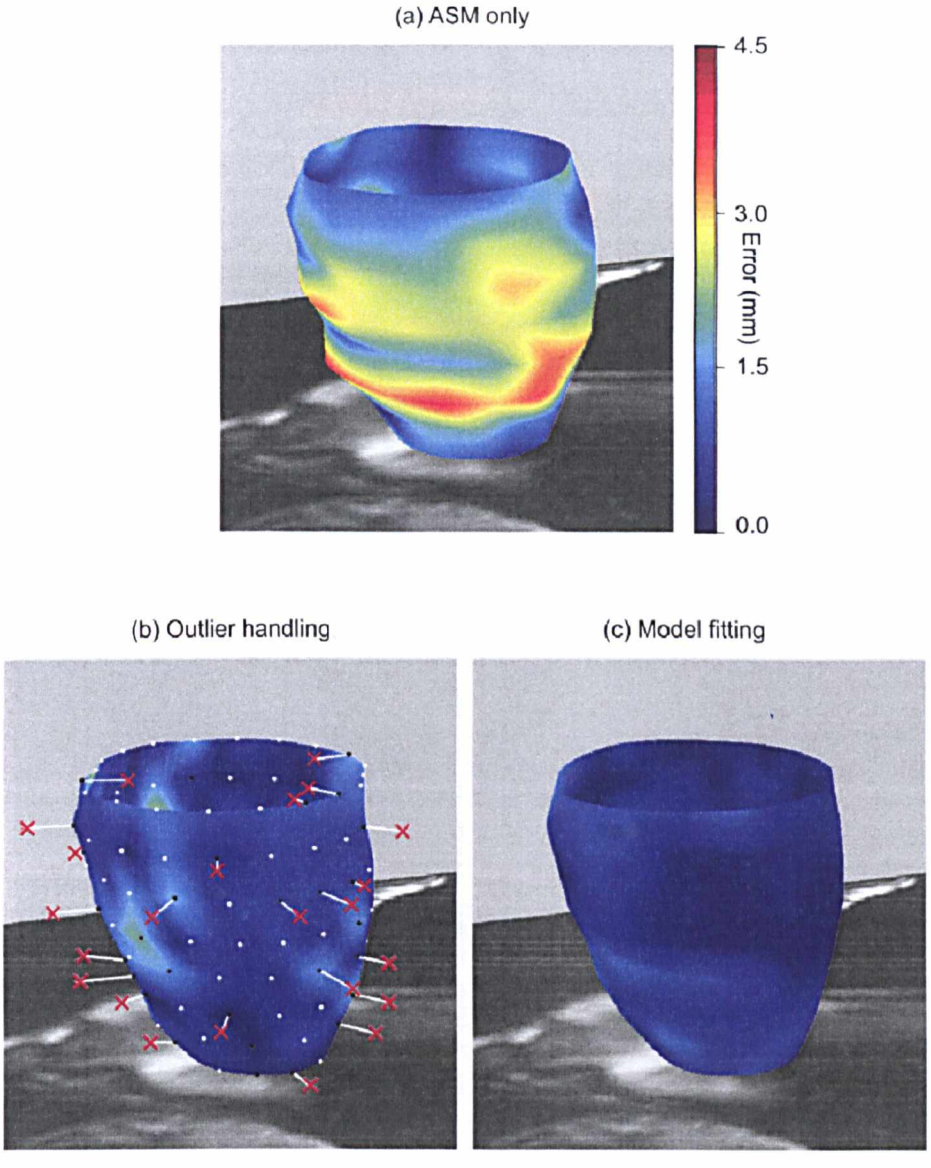

Figure 5.10 Example results showing the distribution and extent of 3D surface localisation errors after the application of the outlier detection and correction algorithms (b) and the subsequent ASM model fitting (c) for left-ventricular segmentation. Without the use of the proposed outlier handling step, the ASM search (a) can introduce significant errors.

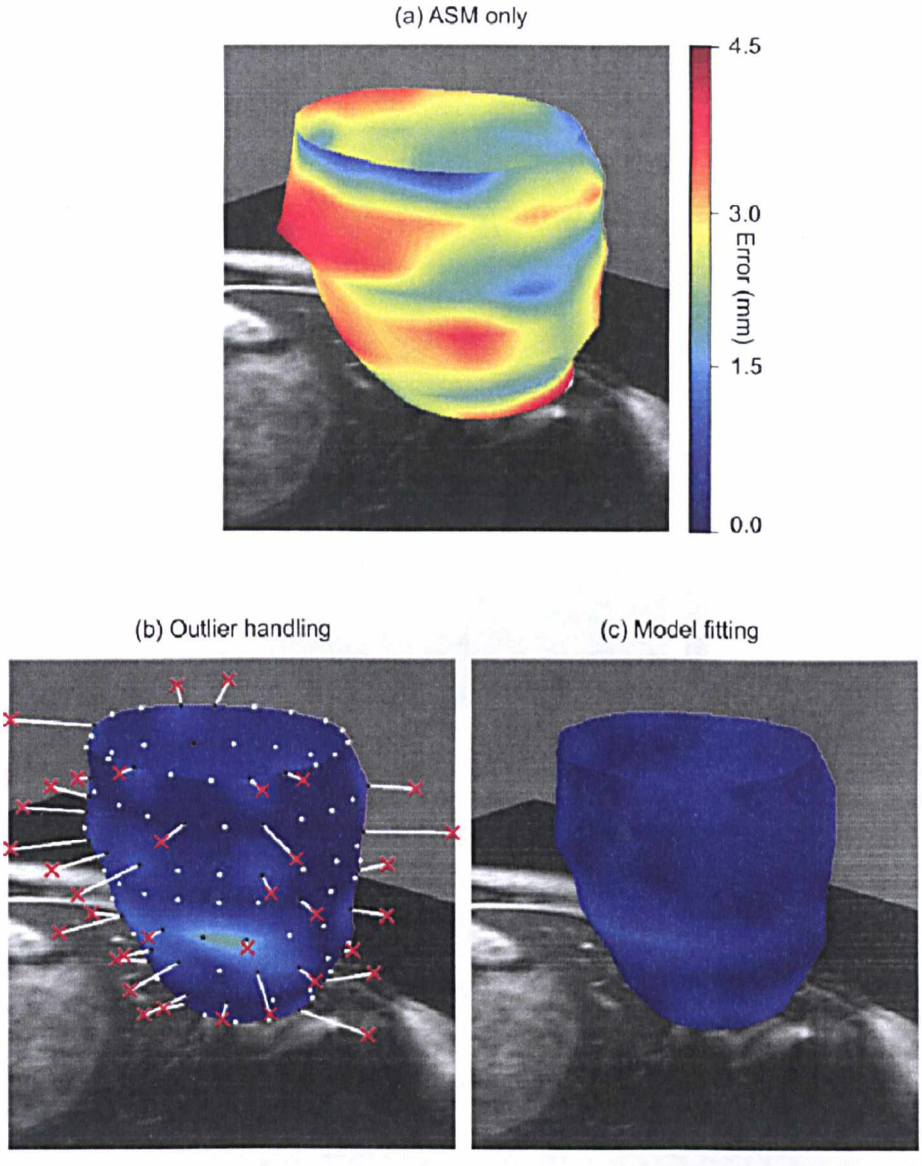

Figure 5.11 The effect of segmentation in the presence of significant outliers. In this case, the standard ASM search is significantly affected (a). Through effective handling of outliers (b), the proposed technique accurately recovers the entire epi-cardial surface (c).

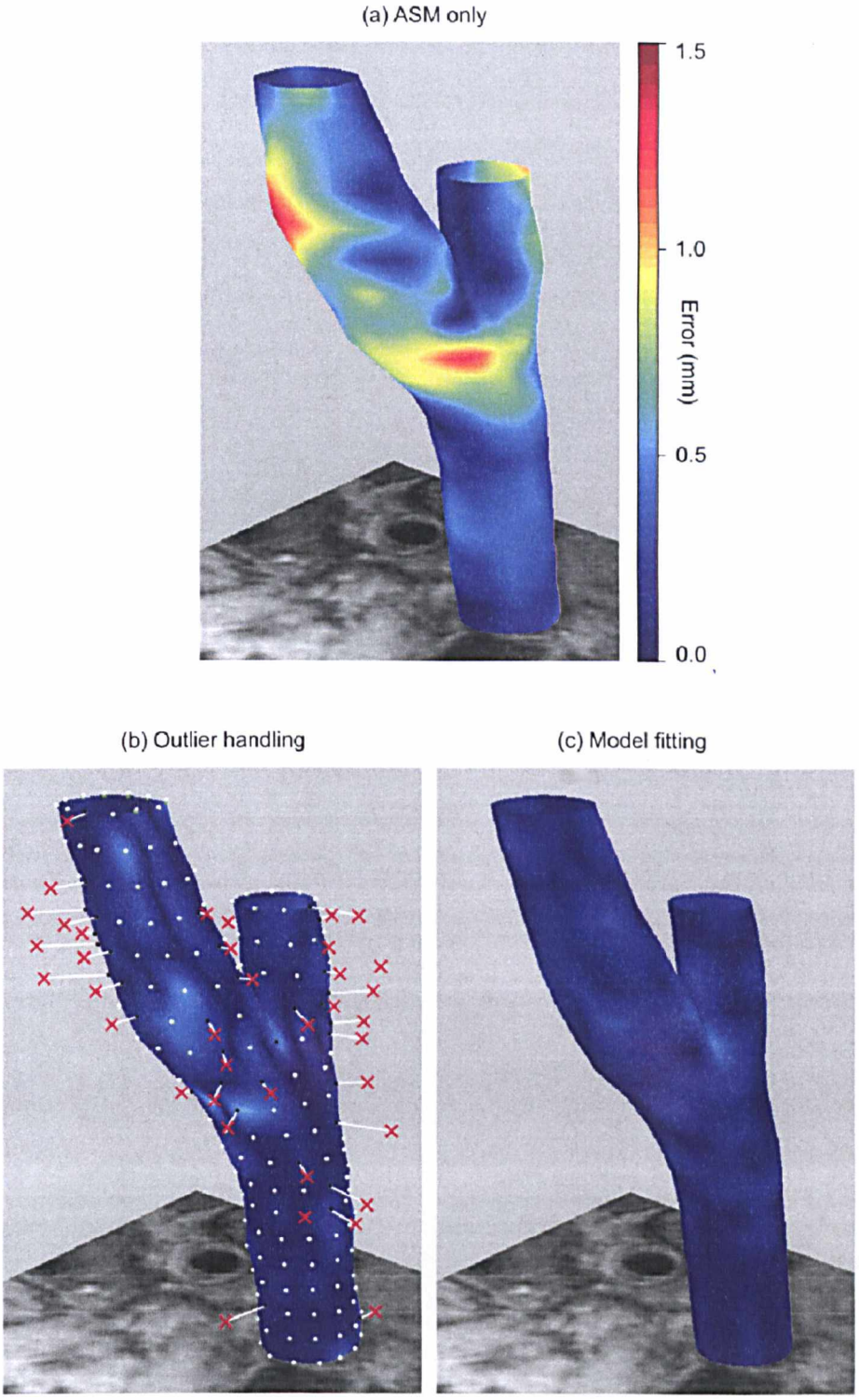

Figure 5.12 Example 3D carotid artery segmentation results showing erroneous ASM segmentation in (a) due to the presence of outliers (less than 20%). The model fitting in (c), however, is not affected when the proposed outlier handling process is incorporated as shown in (b).

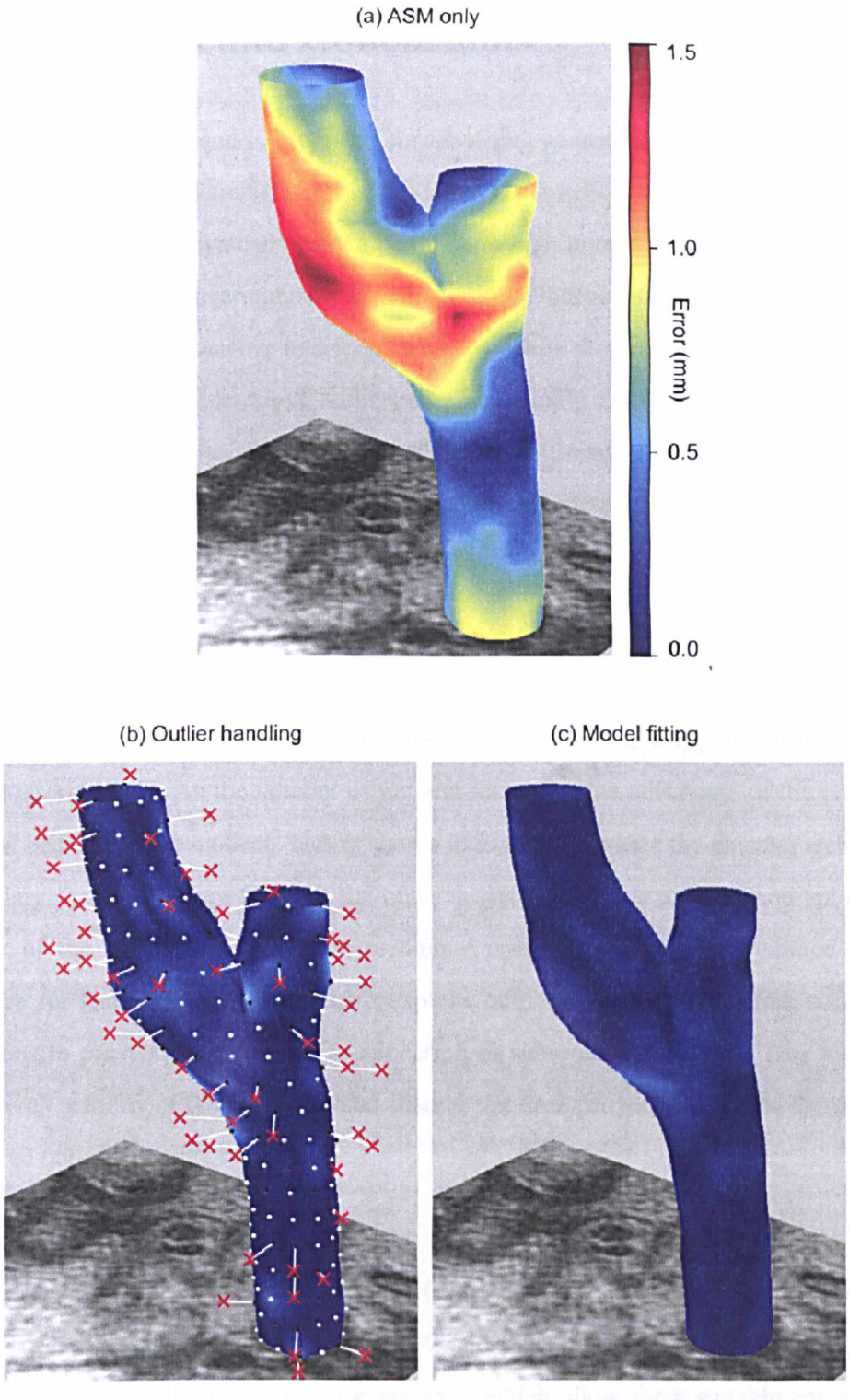

Figure 5.13 Example 3D carotid artery segmentation results in the presence of a significant amount of outliers, which results in poor ASM segmentation (a). The outliers are correctly handled by the proposed technique (b) leading to a more accurate and consistent segmentation result (c).

5.4 Discussion and Conclusions

In this chapter, a technique is presented for localising geometrical inconsistencies of the landmarks based on invariant analysis of ILDs. The method is based on the idea that inconsistent landmarks typically have a particularly high number of inconsistent ILDs. In ASM, the use of an invariant shape metric allows outlier analysis to rely on shape information alone without the interference of the shape alignment procedure. With the proposed method, the identified outliers are not simply rejected or replaced by the corresponding mean values, as often adopted by conventional ASM techniques. Instead, a correction mechanism based on both appearance and geometrical criteria is used to rectify each detected outlier before the model fitting procedure.

The results derived from this study suggest that when the contrast of the local image features is strong and the amount of outliers is relatively small, the performance of the proposed algorithm is similar to that of the existing ASM methods, particularly to those presented in [61,62]. As the number of outliers increases, the advantage of the proposed method becomes more evident. This is shown in Figure 5.4 where the existing techniques show large residual errors for both the outer vessel wall of the carotids and epi-cardial border of the LV. Furthermore, the technique uses a geometrically weighted fitness measure for feature point search which exploits outlier analysis results from successive iterations to prevent outliers from re-appearing in subsequent iterations. This improves the overall stability of the algorithm and ensures the final convergence of the algorithm is achieved only with a few iterations.

The outlier handling algorithm presented in this work relies on three main parameters (k_2, l_d and δ_g). The two-sided tolerance factor k_2 is calculated from the coverage and confidence coefficients, being equal to 0.99 and 0.95, respectively in all experiments. These are typical settings in tolerance analysis, which allow for a suitable coverage of most of the variations. In general, the terminating threshold l_d for outlier detection should be chosen to be similar to that of the confidence coefficient so that the same level of uncertainty in both tolerance interval calculation and outlier detection is used. Finally, the choice of the third parameter δ_g is not critical as it is mainly used to restrict the local search window and our experience has shown that any value around 0.05 can provide

similarly good results. It can be seen from the experimental results in Table 5.1 that identical parameters are used for the carotids and LV datasets despite their morphological and image intensity differences. The proposed method therefore does not require case- or subject-specific tuning of these parameters. For practical applications, this is an important advantage which underpins the potential clinical value of the technique.

In this work, the construction of the statistical shape model and the model fitting procedure are achieved by using the standard ASM including the use of normal search profiles. No changes are made to the ASM itself in order to demonstrate the general applicability of the ILDs. The proposed outlier detection technique is applicable to other extensions of the ASM framework. In this chapter, the method is presented in its simplest form and some adaptations can be introduced. For example, a final outlier detection step could be added after outlier correction so as to further identify and subsequently reject the remaining outliers. Alternatively, the outlier detection and correction stages can be iteratively applied until no further outliers are detected. It is also worth noting that the geometrically weighted fitness measure is mainly used to limit the reoccurrence of the outliers in complex segmentation tasks, particularly when the amount of erroneous feature points is high (more than 20%).

It must be noted that the proposed technique detects the largest subset of points that are consistent with the statistical tolerance model. It is thus theoretically possible that in the presence of more than 50% of outliers, these points would be detected as inliers. In this case, the technique can fail as it relies on a good identification of the outliers. However, it can be argued that this situation is unlikely to happen in practical situations. In next chapter, the method will be further extended for analysing localised dynamic behaviour of anatomical shapes with application to the assessment of myocardial contractility.

6

Motion Abnormality Localisation

6.1 Introduction

In the previous chapter, we have introduced a method for analysing individual landmarks in an extracted anatomical shape. The algorithm enables the localisation of geometrical inconsistencies based on predefined inter-landmark descriptions. This has been used for improving the ASM fitting through effective decoupling of initial shape alignment and subsequent model fitting combined with outlier handling. In this chapter, the proposed framework is to be extended further for a post segmentation task involving the localisation of motion abnormalities. The method is applied for the challenging analysis of regional myocardial contractility*.

The ultimate goal of shape-based analysis in medical imaging is to understand the extracted geometrical information for the detection of morphology or dynamic related abnormalities. Many methods based on geometrical information have been proposed in the past but they have also raised a number of important issues that need to be addressed. One of the key problems is related to the type of motion analysis carried out by conventional methods. The use of global markers is insufficient for interpreting subtle details present in regional abnormalities. Methods based on computational anatomy, such as the ASM, the output shape coefficients can be analysed with respect to the limits of the

* Results first presented at 10th MICCAI Conference, Brisbane, 2007.

corresponding shape space. This is widely used for anomaly detection but the shape parameters are associated with all landmarks, and therefore are not ideal for localised analysis.

Alternative techniques have been proposed in the past to allow for more local analysis of anatomical shapes [74,76]. But their performance is influenced by shape alignment and poor generalisation of the models in the presence of morphological variations. As a result, regional abnormalities are undermined by bias during the model fitting process. To address this problem, the purpose of this chapter is to extend the proposed Inter-Landmark Descriptors (ILDs) for identifying regional abnormalities based on the invariant properties of the landmark configurations. To demonstrate the reliability and flexibility of the proposed method, regional contractile analysis based on spatial-temporal information of the left-ventricle (LV) is to be performed.

The first step towards LV assessment involves the delineation of endo- and epi-cardial borders over the entire cardiac cycle. This is traditionally performed by a combination of manual contouring and interactive editing tools. In addition to the results obtained in this thesis, it is worth mentioning some of the existing techniques that are specific to LV segmentation. Active contours were extended to the temporal domain for LV boundary tracking [111]. Active models have been also adapted for cardiac segmentation [68,112] and a hybrid active shape and appearance approach was proposed in [113]. Jacob *et al.* in [114] used a dynamic tracking approach based on shape and motion models, as well as smoothness and endo-/epi-cardial distance constraints. Lorenzo-Valdes *et al.* [12] used a probabilistic atlas and non-rigid registration to propagate cardiac shapes throughout the cardiac cycle.

A number of automatic techniques have also been suggested for LV motion analysis. Traditionally, global indices are extensively used in clinical practice, such as LV volumes and ejection fraction, despite their intrinsic limitations for detecting localised lesions. A popular alternative for regional assessment is based on the analysis of regional wall thickening but the method is problematic as it does not consider the global dynamics of the heart as a whole. Furthermore, specific disorders such as cardiac de-synchronisation as difficult to detect using conventional assessment methods. The condition is illustrated

in Figure 6.1 where changes in the endo- and epi-cardial radius are plotted over time for a normal subject (a) and a patient suffering from myocardial de-synchronisation (b) at two different myocardial locations. It can be seen that the extent of the contractility appears to be normal for these two myocardial regions in both datasets. A detailed examination, however, reveals that in Figure 6.1(b), the timing and extent of maximal contraction are different. A detailed comparison of the contractility of different myocardial segments is important for identifying these inconsistencies.

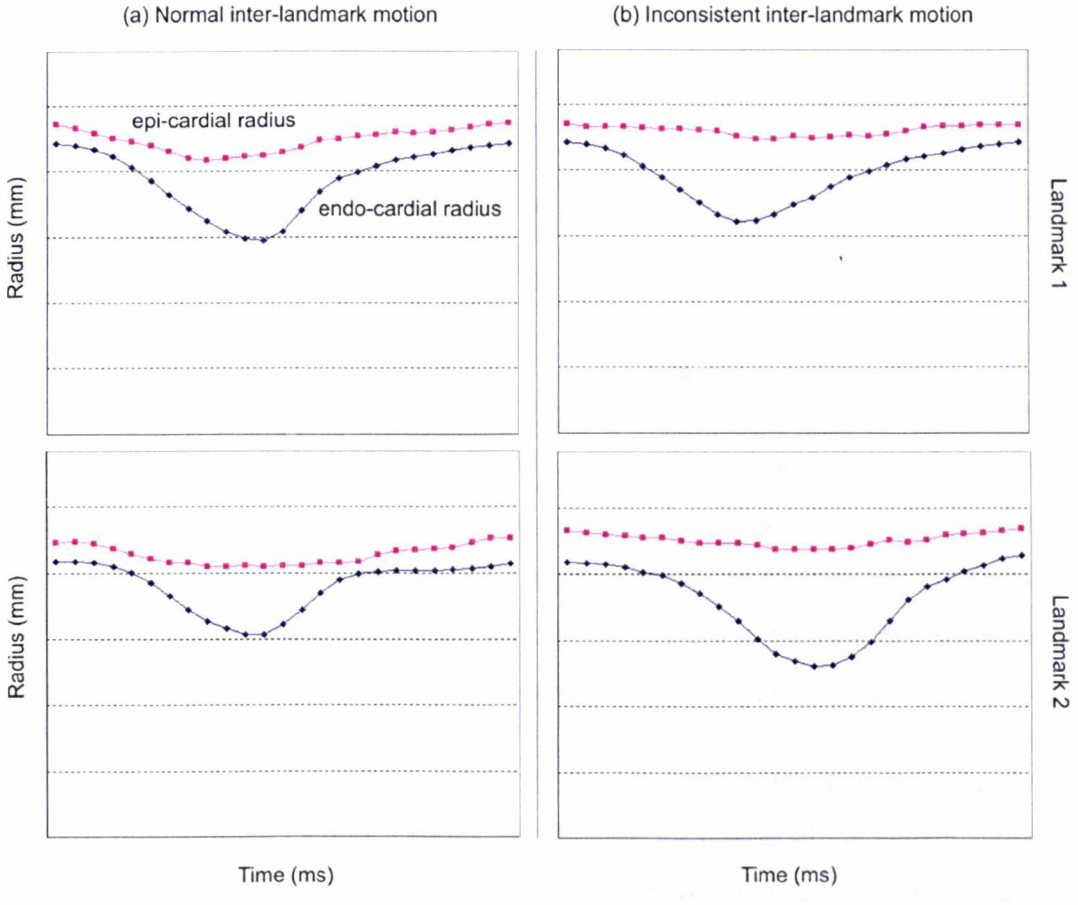

Figure 6.1 Examples of normal versus inconsistent inter-landmark motion. In (b), the timing of end-systole is different to that of (a) for Landmark 2, indicating de-synchronisation of the two myocardial segments. The two myocardial segments also differ in the extent of contractility, which may be associated with potential myocardial infarction.

Another limitation associated with the use of global indices is that subject-specific morphology is discarded. The emergence of statistical shape modelling has allowed the

construction of models for normal anatomy that can be used to detect size, dynamic and shape related abnormalities. Bosch *et al.* [115], for example, generated a global shape parameterisation scheme based on PDM coefficients. Comparison to visual scoring of myocardial wall motion demonstrated a good linear correlation, but the specific identification of local abnormalities is not feasible due to the global nature of the method. More recently, several methods for building more localised shape models have been proposed. Suinesiaputra *et al.* [75], for example, have proposed the use of independent component analysis as an alternative. Sparse PCA methods can also be used to extract more localised shape parameters [74]. PCA coupled with orthomax rotations have been also suggested [76] to classify wall motion abnormalities. Jacob *et al.* [114] defined a clinical interpretation space based on the AHA/ACC (American Heart Association/American College of Cardiology) 17-segment model for assessing regional thickening and excursion of the myocardium.

In this chapter, a new method is presented for both local and global invariant analyses of myocardial motion. To this end, a multi-dimensional ILD is introduced, which incorporates both endo- and epi-cardial changes occurring between coupled regions of the LV over the entire cardiac cycle. By combining coupled myocardial regions into the analysis framework, both geometrical and dynamic inconsistencies can be identified. Additionally, the proposed inter-landmark motion description implicitly incorporates shape, size, thickness, and endo-cardial displacement for regional dysfunction analysis.

To describe normal contractile properties of the LV, multivariate tolerance regions are derived from selected training samples. To improve the quality of the multidimensional tolerance model and ensure it is immune to the choice of the training set, robust estimators are used to calculate the tolerance region parameters. For a given LV dataset, inconsistent ILDs are identified based on the tolerance model and the landmark localisation algorithm from the previous chapter. The method is validated with data from 50 subjects containing both normal subjects and patients with different levels of left ventricular contractile abnormalities.

6.2 Methods

6.2.1 Inter-Landmark Motion Vectors

In this section, the landmark localisation algorithm presented in the last chapter is adapted for wall motion analysis. To this end, the definition of a multivariate ILD that represents the spatio-temporal behaviour of the myocardium is required. The proposed formulation is aimed at detecting local motion abnormality as well as temporal inconsistencies between different segments of the myocardium. Furthermore, the method needs to permit invariant analysis without the need for pre-alignment of the shapes.

Let's suppose that a landmark-based representation of the myocardium is first obtained through segmentation. Given two landmarks p_i and p_j on the boundary, an Inter-Landmark Motion (ILM) vector is introduced as follows:

$$\mathbf{v}\left(P_i, P_j\right) = \left(a_{i1}, b_{i1}, \ldots, a_{iF}, b_{iF}, \ldots, a_{j1}, b_{j1}, \ldots, a_{jF}, b_{jF}\right)^T \tag{6-1}$$

where F is the number of frames in the cardiac cycle. Based on a generalised cylindrical representation, a and b describe the radial distances of the endo- and epi-cardial borders to the axis of the epi-cardial volume. It is interesting to note that $\mathbf{v}$ is a high dimensional ILD (dimension $p = 4F$). In addition to the size and thickness measures encapsulated by these variables, the ILM vectors provide an implicit description of the shape of the myocardial borders. Although the coupled locations can be chosen for the entire LV, it is computationally more efficient to restrict this to be within the same cross-section, where there is a high covariance between the landmarks. For each landmark location, a set of K ILM vectors are derived.

It can be shown that the ILM vector $\mathbf{v}$ is invariant to translation and rotation, but not to scaling. This allows the detection of size-related abnormalities (e.g. ventricular dilatation). Representation of the coupled motion and geometry over the entire cardiac cycle allows both morphological and dynamic inconsistencies to be identified efficiently. For ventricular motion analysis, the configuration of the ILM vectors is schematically illustrated in Figure 6.2, where it can be seen that the invariant cylindrical variables are

extracted with respect to the axis of the LV. The contractility associated with landmarks p_i and p_j is implicitly compared by encapsulating the related variables into a single descriptor. In this figure, the difference between endo- and epi-cardial distances of the two landmarks reveals inconsistent endo-cardial displacement.

6.2.2 Modelling Normal Contractility

In this work, normal myocardial contractility properties are described by using multivariate tolerance regions for each ILM vector as described in Chapter 3. Given N training samples, a tolerance region $R_{\mathbf{v}}$ for the introduced ILM vectors in the p dimensional space can be described as:

$$R_{\mathbf{v}} = \{\mathbf{v} \in \mathbb{R}^p \mid (\mathbf{v} - \bar{\mathbf{v}})^T S_{\mathbf{v}}^{-1} (\mathbf{v} - \bar{\mathbf{v}}) < L\} \tag{6-2}$$

where $\bar{\mathbf{v}}$ and $S_{\mathbf{v}}$ correspond to the mean vector and the covariance matrix, respectively. For the tolerance region limit L in Equation (6-2), it can be estimated from the critical values of the chi-square distribution as [102]:

$$L = \chi^2_{t,(1-\alpha)^{1/N}}. \tag{6-3}$$

A training sample of normal subjects is used to capture the normal variability of myocardial contractility. In practice, the choice of training samples may be limited by the available data and extreme values of the ILM vectors may arise. Even if all samples are normal on a global scale, some undesirable local abnormalities may be present. Aberrant values can also be associated with errors during delineation which can further contaminate the training set. This can affect the calculation of the tolerance regions as the covariance matrix is known to be sensitive to extreme values. Therefore, the construction of the tolerance regions must be independent of the choice of training samples. A robust estimation of the tolerance region parameters is thus required.

A natural robust estimator for the central observation of the distribution can be achieved by replacing the mean by the median vector, denoted as $\mathbf{v}^*$:

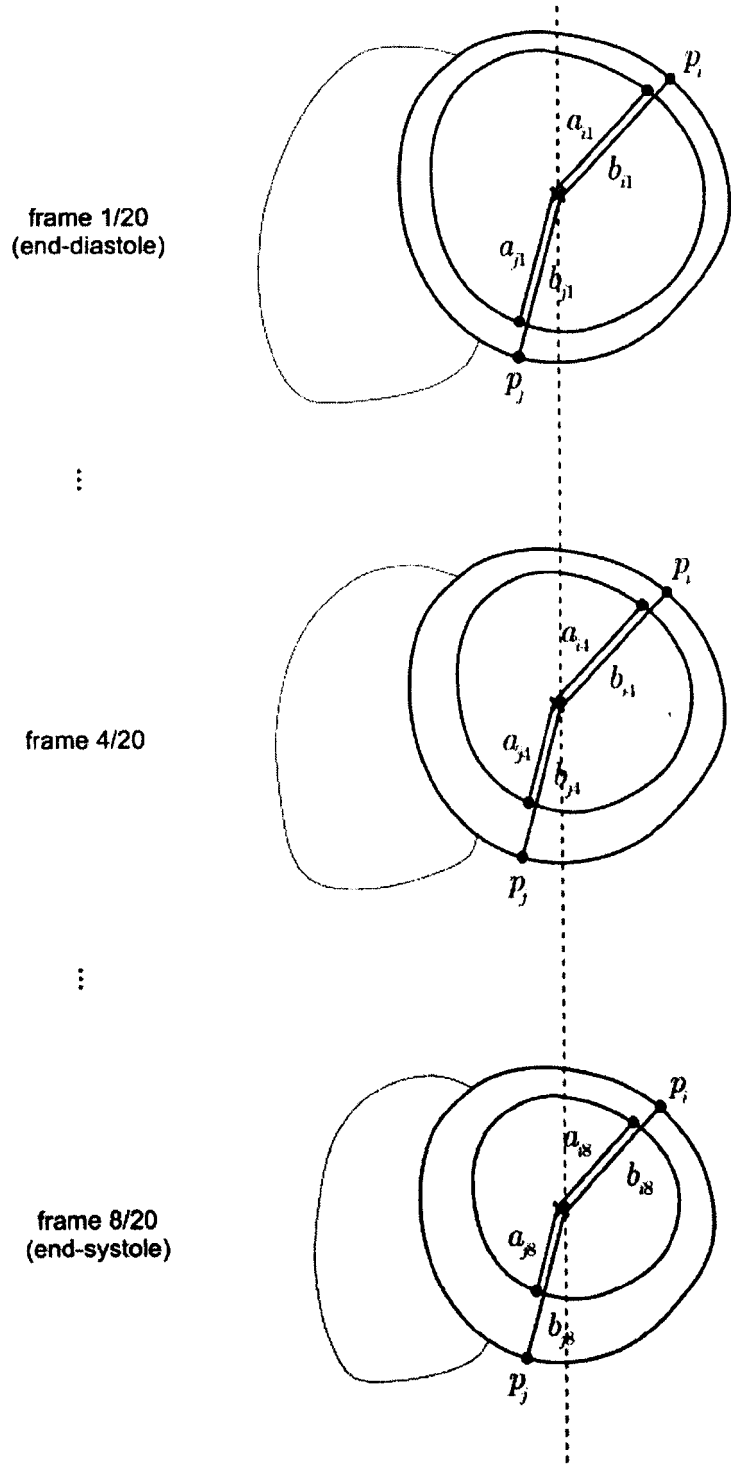

Figure 6.2 Graphical illustration of the ILM vectors, representing coupled contractility at two distinct locations of the myocardium. The axis of the LV is used as the reference to calculate the endo- and epi-cardial variables a and b. The endo-cardial displacement towards the lateral region can be identified by the difference in the variables between the landmarks p_i and p_j.

$$\mathbf{v}^* = \underset{1 \le j \le N}{\text{median}} \left(\mathbf{v}^{(j)} \right). \tag{6-4}$$

A robust estimation of the covariance can then be achieved by iterative weighting of the residuals for all observations. The robust covariance matrix $S_{\mathbf{v}}^*$ at iteration $t+1$ is calculated as:

$$S_{\mathbf{v}}^*(t+1) = \frac{\sum_{j=1}^{N} w^2 \left(\mathbf{v}^{(j)}, \mathbf{v}^*, S_{\mathbf{v}}^*(t) \right) \left(\mathbf{v}^{(j)} - \mathbf{v}^* \right) \left(\mathbf{v}_i - \mathbf{v}^* \right)^T}{\sum_{j=1}^{N} w \left(\mathbf{v}^{(j)}, \mathbf{v}^*, S_{\mathbf{v}}^*(t) \right)} \tag{6-5}$$

where w is a weighting factor calculated from the observation, the median and the covariance matrix of previous iteration. The idea behind this formulation is to assign a large weighting factor for observations that are close to the median and a smaller one for observations that are further away. This procedure is iteratively applied until the values of w do not change significantly. Mathematically, w is defined as follows:

$$w\left(\mathbf{v}^{(j)}, \mathbf{v}^*, S^* \right) = \begin{cases} 1 & \text{if } d\left(\mathbf{v}^{(j)}, \mathbf{v}^*, S^* \right) < d_0 \\ \exp\left(-\dfrac{\left(d\left(\mathbf{v}^{(j)}, \mathbf{v}^*, S^* \right) - d_0 \right)^2}{2\sigma_0^2} \right) & \text{elsewhere} \end{cases} \tag{6-6}$$

where d_0 is a threshold used to identify potential extreme ILM values and σ_0 specifies the decay rate of the penalty function. Both parameters are calculated automatically by analysing $d\left(\mathbf{v}, \mathbf{v}^*, S^* \right)$ at each iteration for $\mathbf{v}^{(j)}$. In essence, the equation rejects observations that deviate from normality, and therefore requires a robust estimation of the distribution of function d such that it is resistant to the presence of extreme values. This can be achieved through the following formulae based on robust statistics [116]:

$$\begin{aligned} d^* &= \underset{1 \le j \le N}{\text{median}} \left(d\left(\mathbf{v}^{(j)}, \mathbf{v}^*, S^* \right) \right), \\ \sigma^* &= 1.4826 \underset{1 \le j \le N}{\text{median}} \left| d\left(\mathbf{v}^{(j)}, \mathbf{v}^*, S^* \right) - d^* \right|. \end{aligned} \tag{6-7}$$

For normal distribution, all valid values are expected to lie within a number of standard deviations (σ^*) from the estimated mean (d^*). It is reasonable to define the threshold d_0 as follows:

$$d_0 = d^* + c_1\sigma^* \ (2 \le c_1 \le 3). \tag{6-8}$$

The decay rate can be set to be equal to $c_2\sigma^*$ ($0<c_2<1$). In this study, we found that $c_2 = 0.2$ could achieve reasonably good results in excluding errors from the training set. Figure 6.3 illustrates an example of a set of distances calculated from an ILM vector. It can be seen that d_0 separates well the extreme values due to the errors incorporated in the training set. Figure 6.4 further compares between conventional and the proposed robust estimation of multivariate tolerance regions. In this 2D illustration, the extreme values induce a translation and rotation of the tolerance region, which is corrected for by using the proposed robust estimation.

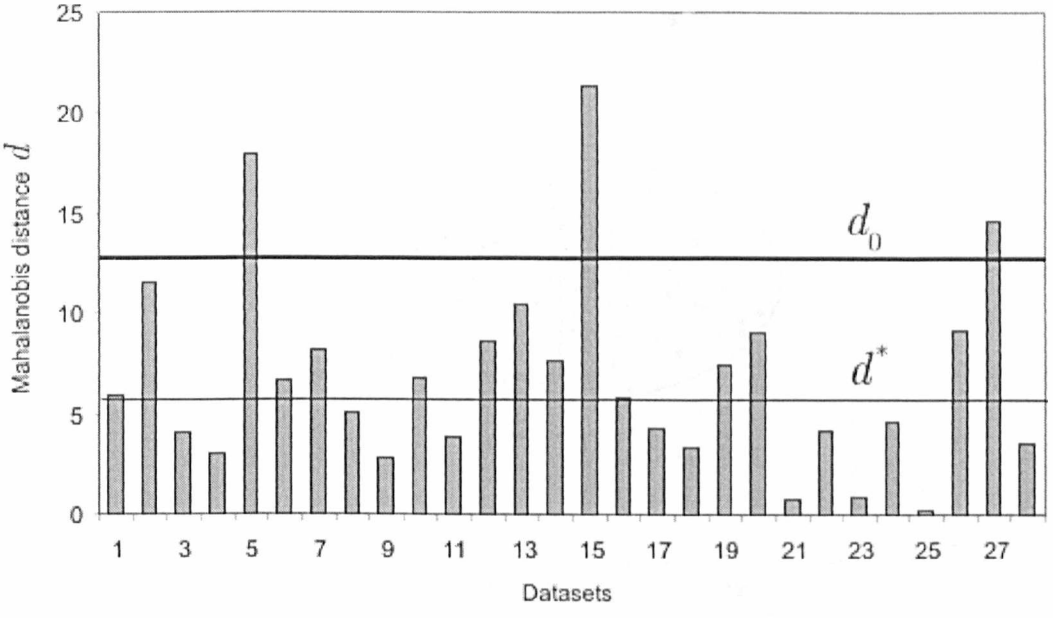

Figure 6.3 Illustration of the minimisation of the effect of extreme ILM vectors on the multivariate tolerance region calculation. The Mahalanobis distances are plotted for the 28 subjects in the training set. It can be seen that the threshold calculated from Equation (6-8) separates well the extreme values that are due to local errors incorporated in the training set. The extreme values are subsequently assigned with small weights while the remaining subjects have a weight equal to 1.

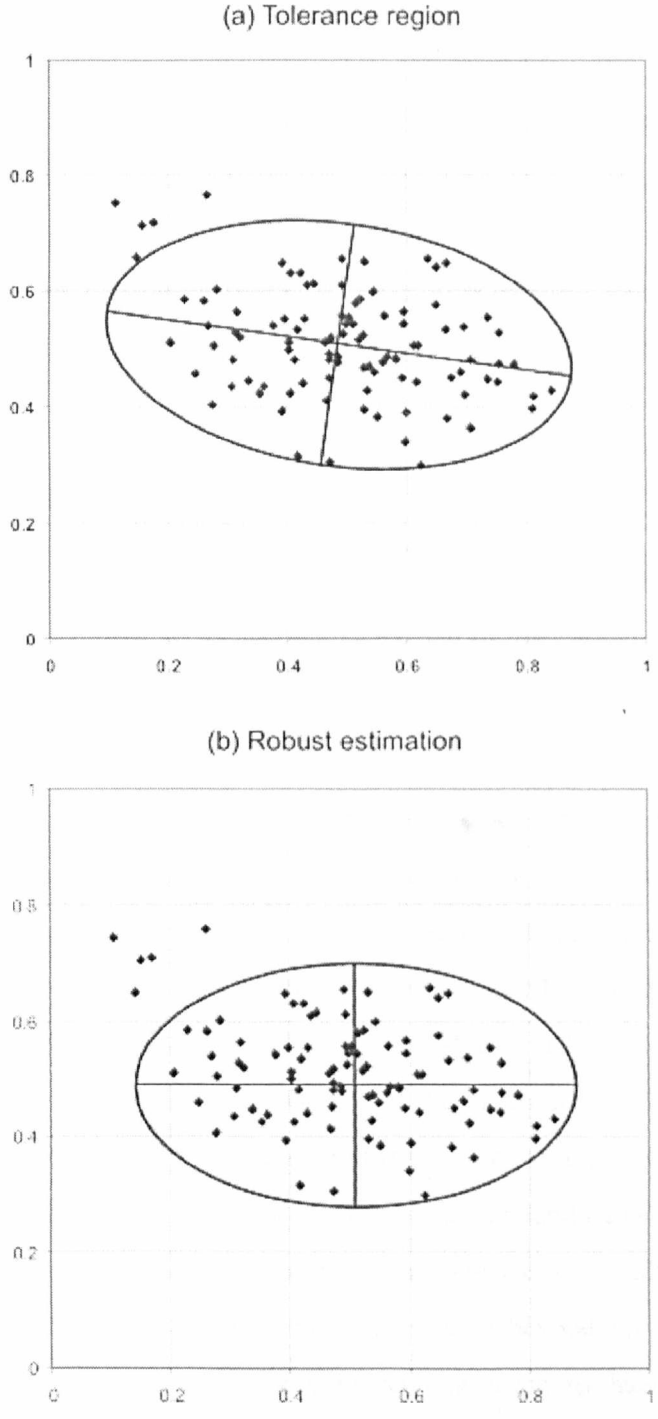

Figure 6.4 Example showing a comparison between conventional and robust estimation of multivariate tolerance regions. In this example, the extreme values induce a translation and rotation of the tolerance region, which is corrected for by using the proposed robust estimation.

6.2.3 Abnormality Localisation

In this section, the iterative algorithm for inconsistent landmark localisation is developed for cardiac motion analysis. For a given left ventricular dataset with delineated boundaries, the ILM vectors are calculated by using Equation (6-1). By using the multivariate tolerance regions introduced in the previous section, it is now possible to identify abnormal inter-landmark relationships. To this end, a Boolean consistency measure is derived as follows:

$$f_d(\mathbf{v}) = \begin{cases} 1 & \text{if } \mathbf{v} \in R_v \\ 0 & \text{if } \mathbf{v} \notin R_v. \end{cases} \tag{6-9}$$

Because each inter-landmark vector incorporates a pair of myocardial segments, it is not straightforward to identify which of the two landmarks is responsible for the potential motion abnormality when the vector in question is outside of the tolerance region.

However, similarly to the algorithm presented in the previous chapter, abnormal myocardial boundary points are expected to have more invalid inter-landmark vectors. A likelihood measure of abnormality can therefore be calculated for each landmark by summing all measures of Equation (6-9) for the associated ILM vectors as detailed in Chapter 5. The iterative localisation procedure introduced in Chapter 5 is adapted for myocardial motion analysis, and a flow-chart of the algorithm derived is provided in Figure 6.5. At each iteration, the location with the lowest consistency measure is detected as abnormal. The likelihood measures of the remaining landmarks are subsequently updated by subtracting the contribution from the rejected myocardial segment. The procedure is repeated until the lowest consistency value is beyond a predefined threshold close to 1, suggesting all the remaining myocardial locations have consistent ILM vectors. In this study, the threshold value used for termination is chosen to be close to 1 to allow for small perturbations around the landmark points.

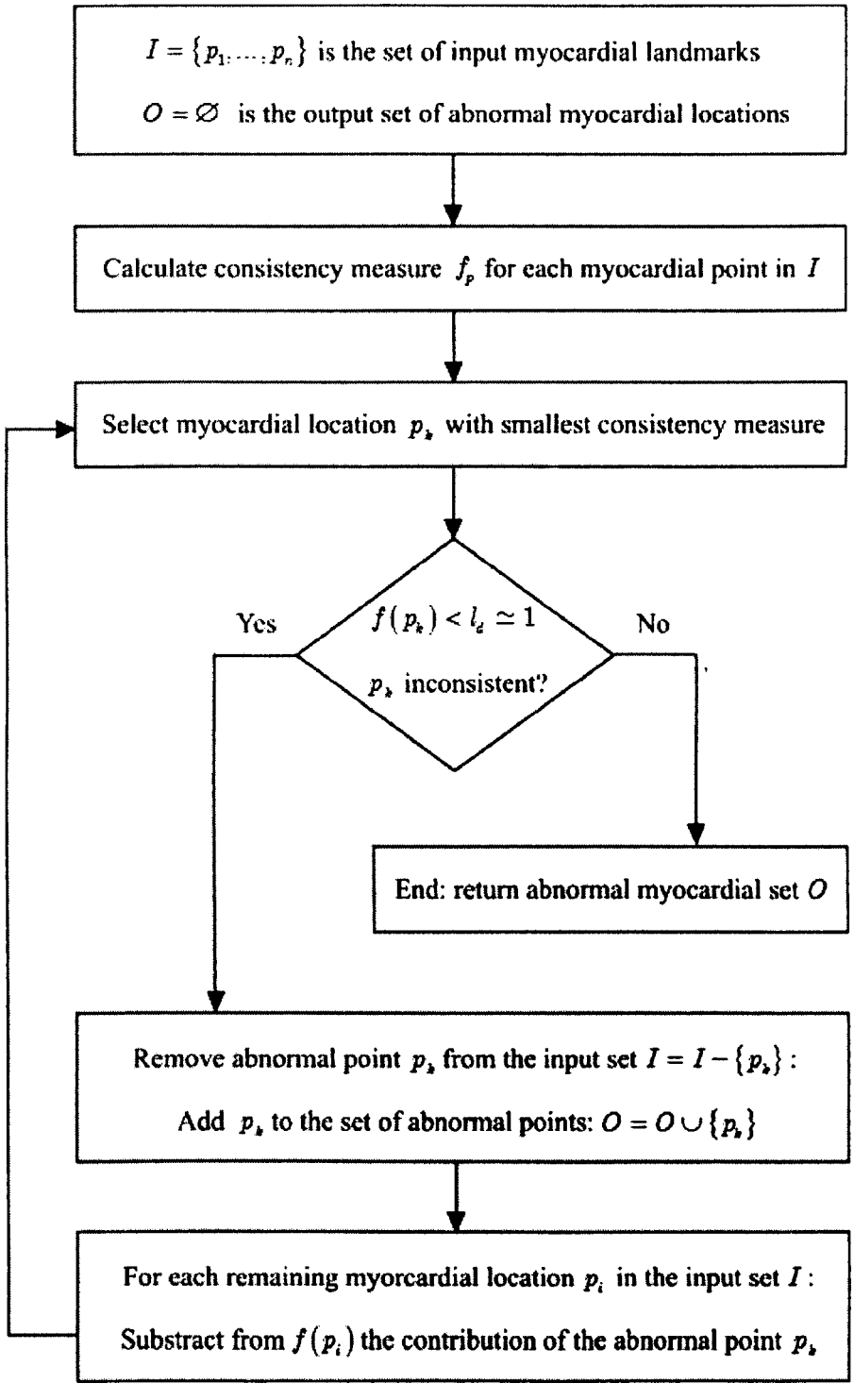

Figure 6.5 A schematic diagram of the iterative myocardial abnormality localisation algorithm. The output is a subset of abnormal myocardial landmarks. The threshold for termination is chosen to be close to 1 to permit some small perturbation of landmark point positions.

6.3 Validation

6.3.1 Experiments

The validation of the technique is carried out on a relatively large dataset consisting of 50 subjects. As in the previous chapters, the subjects were scanned using a 1.5T MR scanner (Sonata, Siemens, Erlangen Germany) and a TrueFISP sequence (TE = 1.5 ms, TR = 3 ms, slice thickness = 10mm and pixel size from 1.5 to 2mm) within a single breath-hold. Retrospective cardiac gating was used to ensure an even coverage of the entire cardiac cycle and for each subject 25 cine frames were acquired.

For all datasets, delineation of the myocardial boundaries was carried out by an expert observer by using a semi-automatic ventricular analysis tool (CMRtools [117]). From the contours obtained, 182 landmarks were uniformly distributed by arc length for each of the boundaries and at all temporal frames of the cardiac cycle, where point correspondences were determined based on the location of the LV/RV junction points. Contractile indices such as ejection fraction, stroke volumes and thickening were calculated and a detailed visual assessment was carried out by the expert observer for regional abnormality localisation. In this study, a total of 28 subjects were identified as normal by the expert observer. These are used for the tolerance model construction. Of the remaining 22 datasets, the observer identified 11 datasets as intermediately abnormal and 11 as severely diseased. All datasets were then evaluated using the proposed method, where the normal subjects were assessed on a leave-one-out basis. The parameters used in the experiments are summarised in Table 6.1.

6.3.2 Results

The percentage of abnormal landmarks was calculated for each dataset and plotted in Figure 6.6 against the ground truth derived from visual examination ((a) normal, (b) intermediately abnormal and (c) severely abnormal). It can be seen from the figure that the calculated percentage of abnormality correlates well with visual classification and a good separation is achieved for almost all datasets. For numerical assessment of class separation, non-parametric tests were used and a significant difference between the 3

groups was found using the Kruskal-Wallis test ($p<0.001$) and post-hoc multiple comparisons using Mann-Whitney test. The average abnormality percentage found for the normal, mildly abnormal and severely abnormal subjects were 1.0 ± 2.0, 14.2 ± 6.0 and 63.8 ± 25.1, respectively. Two normal datasets (shown in crosses) were misclassified by the proposed technique. The first one, characterised by excessive thickening of the myocardium probably due to stress suffered by the patient during scanning, was misclassified since the training sample did not include the corresponding variability. The second misclassification was due to right ventricular dysfunction which will be discussed in detail in Figure 6.8(b).

Table 6.1 Parameters used for the experiments in this study.

Variable	Description	Value
n	Number of landmarks used to represent the myocardial locations along the LV	182
	Total number of datasets for validation	55
N	Number of normal subjects for calculating the multivariate tolerance regions	28
K	Number of ILM vectors for each myocardial location	20
F	Number of interpolated frames for each dataset	25
	Part of shape variation explained by the statistical models	0.99
	Maximum number of iterations for tolerance region estimation	100

For regional assessment, five datasets were selected from each of the three classes and further analysed using the AHA/ACC recommended 17-segment model. The segments were classified by the expert as normal or abnormal and for the proposed method and the abnormality measures were averaged for each segment. By counting the number of misclassifications, percentage accuracy between the proposed method and visual examination was calculated for the fifteen datasets and they are summarised in Figure 6.7. It is evident from the figure that a good agreement has been achieved for all the datasets, with

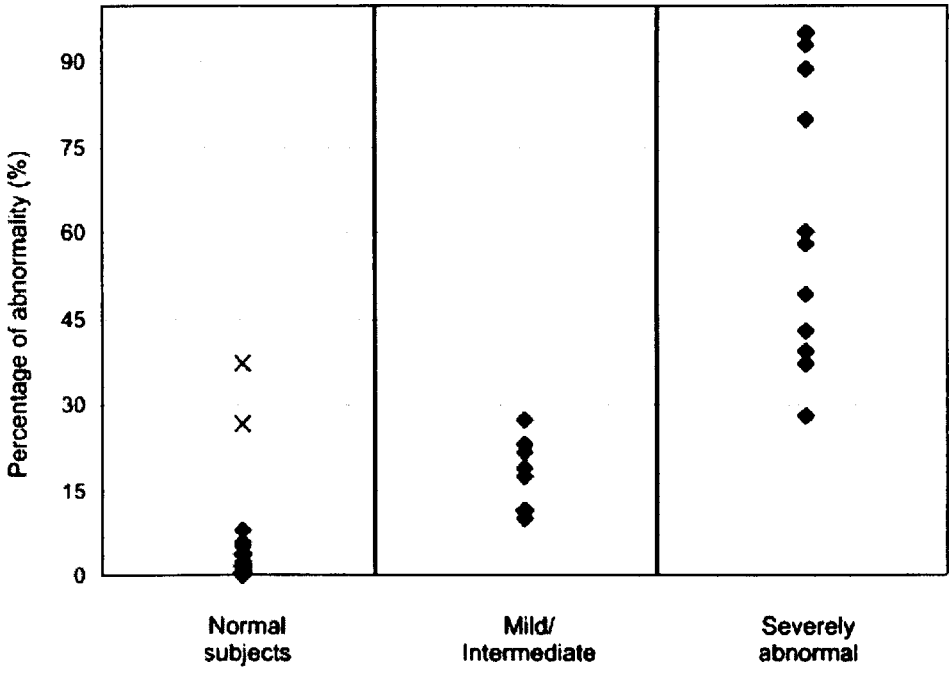

Figure 6.6 Percentage of abnormality as calculated by the proposed technique for the entire dataset, plotted against the visual classification by the expert observer. Only two normal datasets (shown in crosses) are misclassified by the automatic method.

an average accuracy of 91.3 ± 6.9 %. Figure 6.8 shows an example of the segmental assessment by both automatic and manual methods. The identified abnormal segments correspond to the suspected myocardial infarct region, as evident from the short axis images.

To facilitate detailed visualisation of localised contractile abnormalities, 3D LV surface maps were constructed by using the results derived. Three examples are shown in Figures 6.9 to 6.11, where lighter shading corresponds to normal myocardial contractility whereas darker shading indicates a local abnormality. The example in Figures 6.9 shows a LV with partial dilatation and an abnormal ejection fraction of 36 % due to the formation of the scar tissue at the antero-lateral region. The example in Figure 6.10 corresponds to the second misclassification from Figure 6.5, but with normal ejection fraction and thickening measures. The subject has an abnormal right ventricle which is affected by pulmonary hypertension, thus causing abnormal deformation of the LV. More specifically, this causes a severe deformation at the septal region of the LV, which is correctly identified by the proposed method. This illustrates the capability of the proposed technique to

identify both dynamic and shape related abnormalities, unlike conventional techniques. In Figure 6.11, the wall thickening analysis shows normal contractility in all myocardial segments but it is less significant at the infero-lateral region than other locations of the LV. This indicates potential localised myocardial injury due to coronary disease, which affects the extent of contractility at the infero-lateral region.

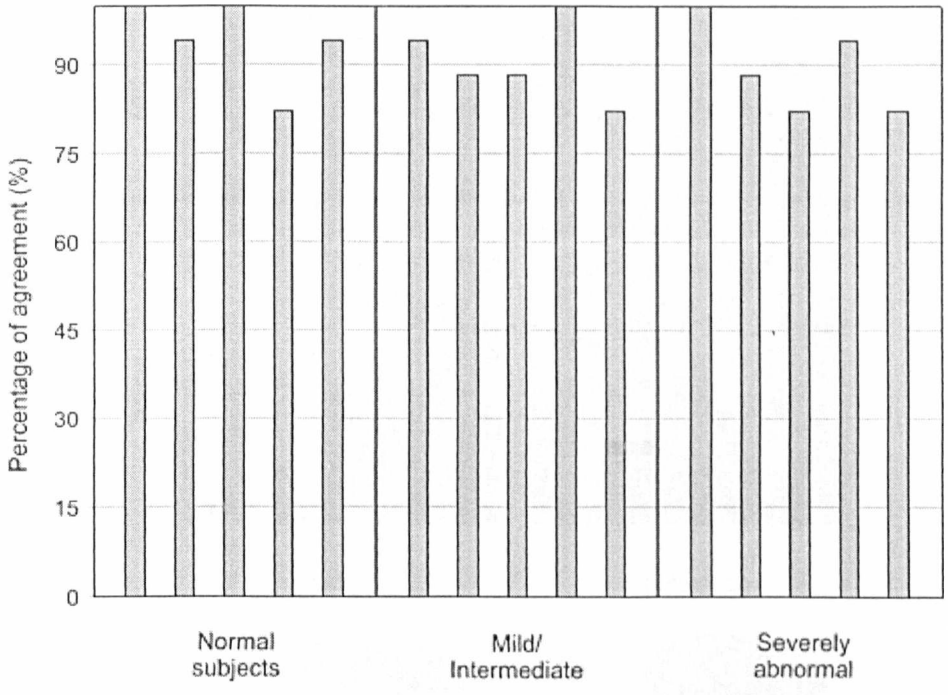

Figure 6.7 Percentage agreement between automatic and manual analysis of myocardial motion for the normal and abnormal segments.

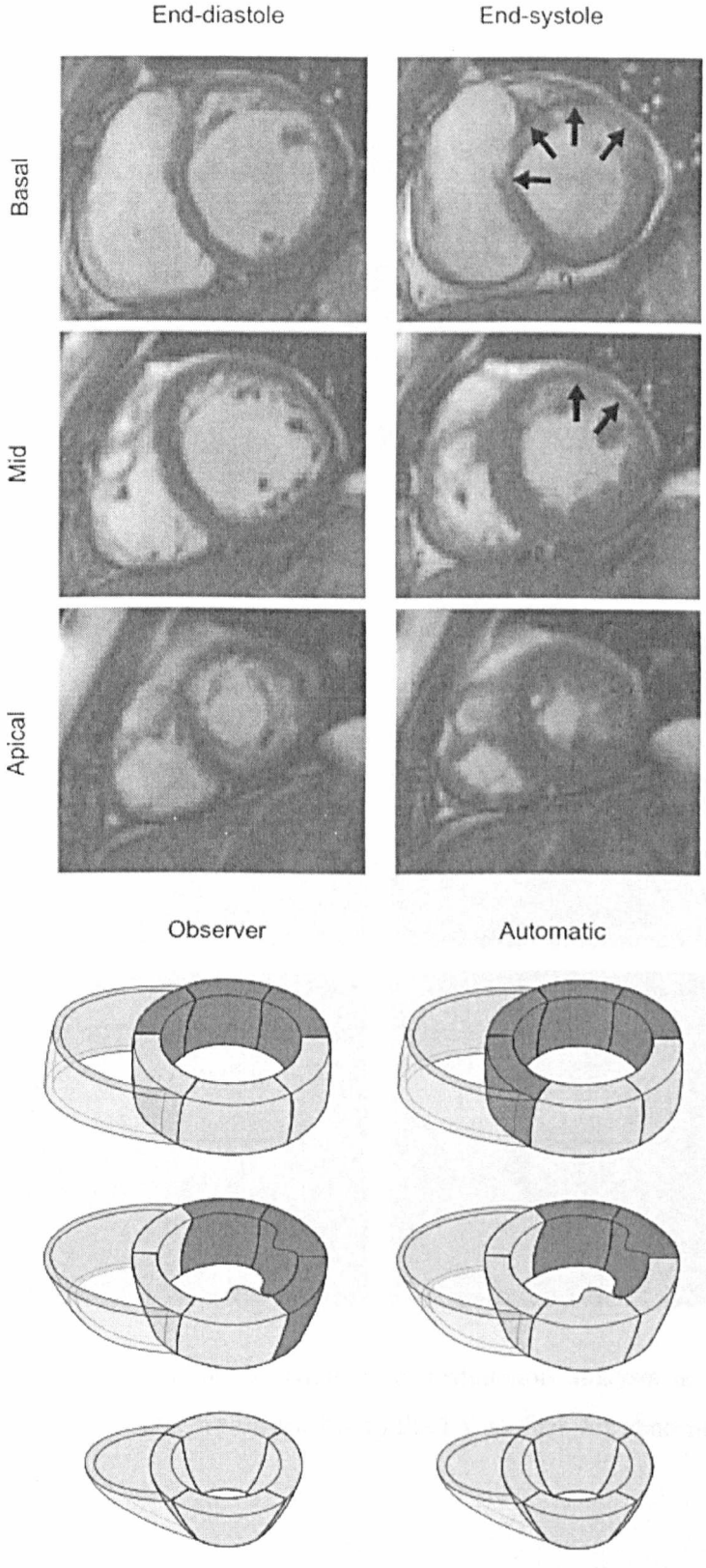

Figure 6.8 An example comparing the 17-segment based local assessment achieved by the automatic and manual abnormality analysis methods.

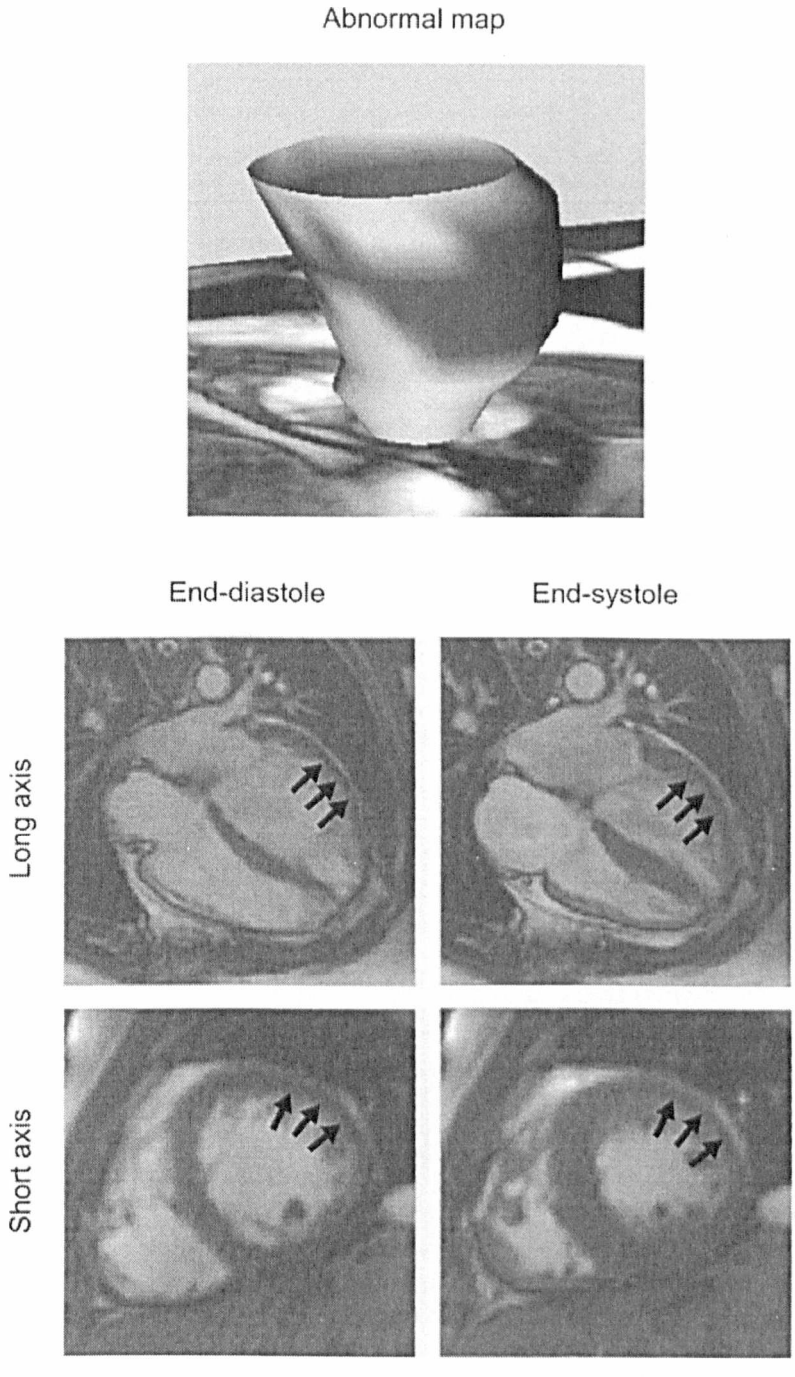

Figure 6.9 Example illustrating the contractile dysfunction analysis achieved by the proposed method. The results are mapped onto the LV surface for abnormality localisation and visualisation.

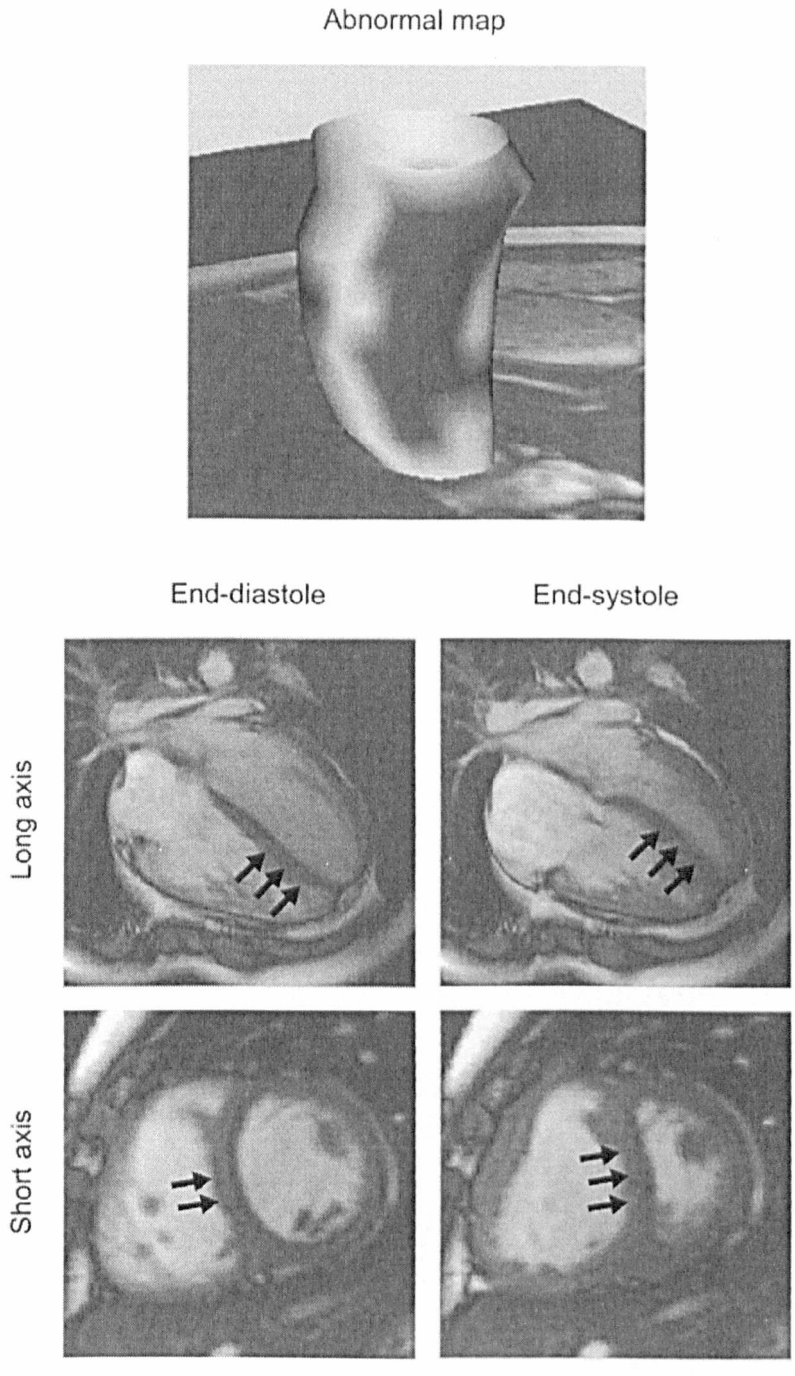

Figure 6.10 In this example, a morphological abnormality due to the right ventricle pushing onto the LV is identified by the proposed method.

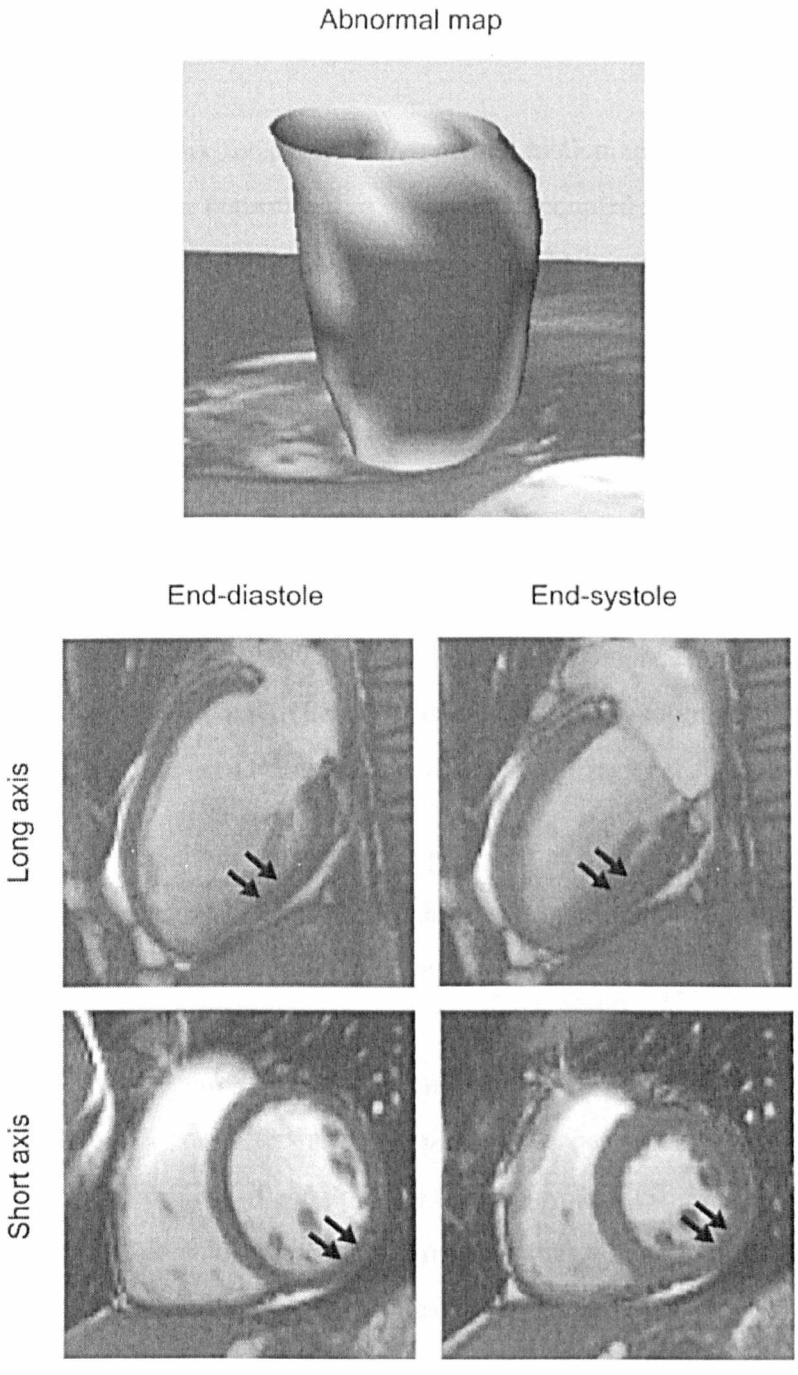

Figure 6.11 In this example, normal thickening can be seen at all regions of the myocardium, but it is less significant at the infero-lateral region than at other locations of the myocardium. This suggests potential myocardial injury affecting the local extent of contractility. The abnormality is successfully identified by the proposed method.

6.4 Discussion and Conclusions

In this chapter, a framework for localised myocardial motion analysis based on ILDs is presented. ILM vectors are constructed to describe the coupled motion of inter-regional myocardial segments throughout the cardiac cycle. This combined spatio-temporal representation allows both morphological and dynamic inconsistencies to be identified. With the proposed framework, the normal contractility properties are captured by estimating the multivariate tolerance region for the introduced ILM vectors. Robust estimators are used to overcome the influence of extreme values, allowing more flexible training set selection and accurate model definition. From a theoretical stand point, the proposed method is adapted from the inconsistent landmark localisation algorithm presented in Chapter 5. For a given LV, a consistency measure is estimated for each myocardial location, which enables iterative detection of local abnormality. A segmental motion distribution can be derived to enable visualisation of regional abnormality.

The technique shows clear advantages of the proposed technique over existing regional assessment approaches based on myocardial thickness and thickening. First, it performs motion analysis independently of shape alignment, and therefore is immune to the effect of localised abnormality. Furthermore, both global and local aspects of myocardial motion are taken into account by the use of multiple ILM vectors. The technique also encodes implicitly other parameters such as thickness, shape and size. Unlike traditional methods based on the analysis of end-diastolic and end-systolic differences, the proposed approach incorporates complete temporal information, thus allowing the identification of abnormalities that are related to different phases of the cardiac cycle.

In summary, this chapter demonstrates the flexibility of ILDs for studying anatomical structures in terms of both shape extraction and motion analysis. It is important to note that although the technique permits localisation of abnormalities but in its current form it does not quantify the extent of dysfunction involved. A possible solution would be to use the individual ILM vectors and their deviations from the normal distribution. Although this is not the main subject of this thesis, the degree of regional abnormality is important in clinical assessment particularly for serial examinations to assess the efficacy of therapeutic measures. Another limitation is that in the current implementation, the

proposed method does not take into account twisting motion of the ventricle, which is important factor to consider for myocardial contractility analysis. Due to the unique fibre-architecture of the myocardium, the contraction and relaxation of the heart consists of the base twisting in one direction while the apex twisting in the opposite direction. In order to capture these motions, it is necessary to use different MR sequences, either MR tagging or MR phase contrast velocity imaging [118]. Nevertheless, the basic theoretical frame-work will hold. For MR tagging, for example, ILM vectors can be defined at tag intersection points, which permit detailed modelling of intra-mural motion of the myo-cardium.

7

Conclusions

7.1 Summary of the Thesis

Anatomical shape analysis is an important topic in medical image computing as it is the pre-requisite for deriving functional indices and tracking morphological changes in responses to therapeutic measures. With increasing capabilities of image modalities, particularly the emergence of real-time imaging techniques, automatic techniques are required for robust boundary shape extraction as well as for detailed investigation of geometrical information. Due to the morphological complexity and variability involved, as well as to difficulties that are inherent to medical image data, the study of anatomical structures requires effective approaches for shape description, modelling, extraction and analysis. While landmark coordinates have been used extensively, the materials introduced in this thesis represent a first attempt at using Inter-Landmark Descriptors (ILDs) for shape-based image analysis. This work is motivated clinically by the following requirements:

- the demand for interactive and consistent frameworks that require minimal user interaction.
- the need for effective incorporation of suitable prior geometrical knowledge that can allow detailed shape extraction and interpretation;
- the need for generic frameworks that are resistant to challenging imaging conditions and applicable to different applications;

In order to incorporate prior knowledge about the anatomical shapes under investigation, statistical shape modelling based on landmark data represents the basic framework for the work presented in this thesis. The aim of the proposed approach using ILDs is to address specific drawbacks of existing methods based on coordinates and multivariate statistics, particularly the Active Shape Model (ASM). The lack of invariance to the pose parameters is problematic in the presence of inconsistencies, while the global nature of the shape parameters prohibits detailed localised shape analysis. As a result, despite recognised merits, the ASM framework suffers from a range of technical difficulties in challenging applications, *i.e.*,

- the use of global shape model for reliable and effective initialisation of image search is difficult, particularly for volumetric and dynamic datasets;
- the current feature search strategy results in limited coverage of the image space and unconstrained localisation of feature points;
- the presence of image inhomogeneities can easily introduce outliers which can affect considerably the shape alignment and model fitting processes;
- the model does not bode well for regional abnormality analysis.

In this work, we have presented a shape modelling framework based on ILDs. Throughout the thesis, we have demonstrated many advantages of these variables for shape-based image analysis. First of all, unlike landmark coordinates, ILDs are invariant to similarity transformations, which is beneficial when pose parameters are either unknown or difficult to be estimated accurately. Secondly, they provide a practical means of decomposing global shape alignment from local shape analysis, thus enhancing the overall consistency and robustness of shape analysis. Finally, by effective modelling of suitable inter-landmark relationships, relevant correlations between different parts of the shape can be captured and subsequently used for identifying shape inconsistencies.

7.2 Technical Contributions

One of the key contributions of the thesis is the proposal of ILDs for statistical shape analysis. We have presented some of the key features of ILD and proposed a number of new algorithms and statistical implementations that enable the effective use of the ILDs. In particular, issues related to invariance to non-shape parameters, implicit encoding of correlations between different parts of the shape, and shape parameter decomposition are addressed. Multivariate ILDs have also been discussed, which include barycentric coordinates and spatio-temporal ILD vectors. Their properties for modelling normal anatomy, particularly through the use of statistical intervals, are illustrated. The intersection of multiple tolerance intervals is used in this thesis as the basis for imposing constraints on individual landmarks.

Since each ILD is associated with more than one point, it is not straightforward to make statistical inference on individual landmarks by simple analysis of the ILD values. The same problem arises in terms of landmark prediction, which also depends on the position of other landmarks of the shape. New algorithms and statistical modelling are therefore introduced in order to effectively manipulate these ILDs for shape-based image analysis. In this thesis, we have developed a method for the construction of geometrical priors that can be used to constrain individual landmarks during image search. This is achieved through the inter-landmark conditional probability, a statistical representation of inter-landmark patterns invariant to the location of the shape, which assists the prediction of an unknown landmark by taking into account positions of other points in the shape. To improve the ASM output, a feature point search algorithm is introduced based on a combinatorial approach. With this method, instead of searching for feature points independently using conventional normal profiles, a sequential approach is used where the inter-landmark constraints are applied successively to limit the search space. The A* algorithm is then adapted to the problem to ensure the detection of the optimal set of feature points given the local models of appearance. Automatic initialisation based on the inter-landmark constraints is also derived based on heuristics for estimating the degree of intersection of the landmark prediction regions with the boundary of interest.

Another important contribution of the thesis is the effective handling of outliers. The method is based on the idea that inconsistent landmarks typically have a particularly high number of inconsistent ILDs. In ASM, the use of an invariant shape metric allows outlier analysis to rely on shape information alone without the interference of the shape alignment procedure. With the proposed method, the identified outliers are not simply rejected or replaced by the corresponding mean values, as often adopted by conventional ASM techniques. Instead, a correction mechanism based on both appearance and geometrical criteria is used to rectify each detected outlier before the model fitting procedure. The technique uses a geometrically weighted fitness measure for the feature point search which exploits outlier analysis results from successive iterations to prevent outliers from re-appearing in subsequent iterations. This improves the overall stability of the algorithm and ensures the final convergence of the algorithm is achieved only within a few iterations.

The ultimate goal of shape-based analysis in medical imaging is to understand the extracted geometrical information for the detection of abnormalities, either geometrically or dynamically. A framework for localised myocardial motion analysis based on ILDs is presented in this thesis. ILM vectors are constructed which describe the coupled motion of inter-regional myocardial segments throughout the cardiac cycle. This combined spatio-temporal representation allows both morphological and dynamic inconsistencies to be identified. With the proposed framework, the normal contractility properties are captured by estimating the multivariate tolerance region for the introduced ILM vectors. Robust estimators are used to overcome the influence of extreme values, allowing for a more flexible training set selection and accurate model definition. The experimental results derived demonstrate the flexibility of ILDs for studying anatomical structures in terms of both shape extraction and motion analysis.

In summary, the main contributions of this thesis are:

- Theoretical investigation and algorithm development of ILDs for shape-based medical image analysis;

- Formulation of partial and invariant geometrical constraints for landmark search;

- Development of an invariant landmark analysis algorithm for inconsistent landmark identification;

- Incorporation of the above methodologies for addressing the current limitations of ASM including shape initialisation, optimal feature point search, outlier handling and localisation of shape and motion anomalies;

- Validation of the proposed methods with concrete clinical data with applications to left ventricular segmentation, carotid artery segmentation, and myocardial motion analysis.

7.3 Discussion and Further Research

Despite the unique strength demonstrated in this thesis, the proposed framework does have some limitations that deserve future work. For example, the proposed technique in its current implementation requires additional computation particularly during initialisation, which makes real-time, interactive shape localisation difficult. Although this can be resolved to some extent by improved software coding and hardware, it is necessary to further optimise the algorithm design, for example by using a multi-resolution approach. In terms of outlier detection, the method presented in this thesis is relatively simple and there is additional scope for improvement. For example, a final outlier detection step could be added after outlier correction so as to further identify and subsequently reject the remaining outliers. Alternatively, the outlier detection and correction stages can be iteratively applied until no further outliers are detected.

For motion analysis, it is important to note that although the technique permits localisation of abnormalities, it does not quantify the extent of dysfunction involved in its current form. A possible solution would be to use the individual ILM vectors and their deviations from the normal distribution. Although this is not the main subject of this thesis, the degree of regional abnormality is important in clinical assessment particularly for serial examinations to assess the efficacy of therapeutic measures. In addition to the applications demonstrated in this thesis, the proposed method can potentially be generalised to other areas of research.

One of the interesting areas for further exploration is in predictive modelling. Predictive modelling of anatomical structures in medical imaging is mainly concerned with predicting *invisible* (immeasurable) parts of an anatomical shape from observable data. The procedure has a wide range of applications such as surgical planning, motion adaptive radiation therapy, and motion adaptive imaging. Most of the existing techniques for predictive motion modelling have so far been based on simple linear regression. More recently, a technique called Partial Least Squares Regression (PLSR) has been used for predictive motion modelling [119]. The goal of PLSR is to resolve some of the difficulties involved in linear regression methods (*e.g.* multi-linear regression) due to multi-collinearity of the predictors.

The advantage of these statistical based predictive models is that they forgo the traditional approach of using biomechanical modelling such as finite element modelling. It is well known that biomechanical models work well if all the mechanical properties of the tissue and tissue-tissue interaction are known. For *in vivo* applications, however, these properties are patient specific and difficult to obtain. This suggests the potential strength of using model-free techniques for predictive motion modelling, by learning and utilizing the associated geometrical patterns. To this end, the use of ILDs can have significant advantages, particularly in its independence to shape alignment which is difficult to achieve in the presence of local tissue deformation. More importantly, the ILDs provide a flexible means to build explicit local deformation constraints by considering varying combination of landmarks and by modelling different intra-shape relationships. Combining ILDs and PLSR for predictive modelling will require specific algorithmic implementation to provide a mapping onto the image space.

Another important application of the proposed ILDs is for assessing post-operative recovery of the heart through a systematic follow-up. For example, a long-term project is currently underway to examine the impact of septal myectomy on patients with hypertrophic cardiomyopathy, a pathology which is a leading cause for sudden cardiac death in young adults [120]. In this regard, ILDs are well suited for long-term follow-up of these patients in a consistent and detailed fashion. The major technical challenges involved are concerned with elucidating subtle sequential remodelling of the myocardium, and to

correlate this with coupled biomechanical and haemodynamic factors that lead to improved cardiac function. We believe that the invariant properties of modelling techniques developed in this thesis can play an important part in this challenging area of clinical research.

7.4 Conclusions

In conclusion, we have presented in this thesis a novel approach for shape-based analysis based on ILDs. The proposed methods are in response to the increasing demand for computational tools that can incorporate suitable prior geometrical knowledge, minimise user interaction, and can be consistently applied to varying imaging conditions. They cater for both morphological and motion analysis of complex anatomical structures. The experimental results demonstrate the potential clinical value of the techniques. It is expected that the proposed analysis framework is particularly suited for serial examination of dynamic 3D models, which currently is still limited to labour intensive examination. The methods proposed therefore address one of the major bottlenecks of current imaging techniques, particularly ultra-fast high-resolution imaging modalities such as MRI. The sensitivity of the method can contribute towards the identification of early image biomarkers for assessing the onset of pathological changes and the efficacy of therapeutic measures.

Bibliography

[1] I. L. Dryden and K. V. Mardia, *Statistical shape analysis*. New York: Wiley, 1998.

[2] C. Goodall, "Procrustes methods in the statistical analysis of shape," *Journal of the Royal Statistical Society B*, vol. 53, no. 2, pp. 285-339, 1991.

[3] L. Dorst, "First order error propagation of the procrustes method for 3D attitude estimation," *IEEE Transactions on Pattern Analysis and Machine Intelligence*, vol. 27 no. 2, pp. 221–230, 2005.

[4] D. E. Slice, "Geometric morphometrics," *Annual Review of Anthropology*, vol. 36, pp. 261-281, 2007.

[5] T. F. Cootes, D. Cooper, C. J. Taylor, and J. Graham, "Active shape models - Their training and application," *Computer Vision and Image Understanding (CVIU)*, vol. 61, no. 1, pp. 38-59, 1995.

[6] R. C. Gonzalez and R. E. Wood, *Digital Image Processing*: Addison-Wesley, 1992.

[7] M. Sezgin and B. Sankur, "Survey over image thresholding techniques and quantitative performance evaluation," *Journal of Electronic Imaging*, vol. 13, no. 1, pp. 146-165, 2004.

[8] G. B. Coleman and H. C. Andrews, "Image segmentation by clustering," *Proc. IEEE* vol. 67, pp. 773-785, 1979.

[9] D. L. Pham and J. L. Prince, "An adaptive fuzzy c-means algorithm for image segmentation in the presence of intensity inhomogeneities," *Pattern Recognition Letters*, vol. 20, no. 1, pp. 57-68, 1999.

[10] W. M. W. III, W. E. L. Grimson, R. Kikinis, and F. A. Jolesz, "Adaptive segmentation of MRI data," *IEEE Transactions on Medical Imaging*, vol. 15 no. 4, pp. 429-442, 1996.

[11] T. Rohlfing, R. Brandt, R. Menzel, D. B. Russakoff, and J. C.R. Maurer, "Quo vadis, atlas-based segmentation?," in *The Handbook of Medical Image Analysis* -

Volume III: Registration Models, J. Suri, D. L. Wilson, and S. Laxminarayan, Eds. New York: Kluwer Academic / Plenum Publishers, 2005, pp. 435-486.

[12] M. Lorenzo-Valdes, G. I. Sanchez-Ortiz, R. Mohiaddin, and D. Rueckert, "Atlas-based segmentation and tracking of 3D cardiac MR images using non-rigid registration," in Medical Image Computing and Computer Assisted Intervention (MICCAI), 2002.

[13] J. B. A. Maintz and M. A. Viergever, "A survey of medical image registration," *Medical Image Analysis*, vol. 2, pp. 1-36, 1998.

[14] P. Thompson and A. W. Toga, "Detection, visualization and animation of abnormal anatomic structure with a deformable probabilistic atlas based on random vector field transformations," *Medical Image Analysis*, vol. 1, no. 4, pp. 271–294, 1997.

[15] M. Kass, T. McInerney, and D. Terzopoulos, "Snakes: active contour models," *International Journal of Computer Vision*, vol. 1, no. 4, pp. 321-331, 1987.

[16] S. Joshi, S. M. Pizer, P. T. Fletcher, A. Thall, and G. Tracton, "Multi-scale 3-D deformable model segmentation based on medial description," in Information Processing in Medical Imaging (IPMI), 2001.

[17] S. Pizer, D. Fritsch, P. Yushkevich, V. Johnson, and E. Chaney, "Segmentation, registration, and measurement of shape variation via image object shape," *IEEE Transactions on Medical Imaging*, vol. 18, pp. 851-865, 1999.

[18] F. J. Rohlf, "Fitting curves to outlines," in Proc. of the Michigan Morphometrics Workshop, 1990.

[19] L. H. Staib and J. S. Duncan, "Boundary finding with parametrically deformable models," *IEEE Transactions on Pattern Analysis and Machine Intelligence*, vol. 14, no. 11, pp. 1061-1075, 1992.

[20] C. Brechbuehler, G. G. Gerig, and O. Kuebler, "Parametrization of closed surfaces for 3D shape description," *Computer Vision and Image Understanding (CVIU)*, vol. 61, no. 2, pp. 154-170, 1995.

[21] P. Schroeder and W. Sweldens, "Spherical wavelets: Efficiently representing functions on the sphere," in Proc. of SIGGRAPH 1995.

[22] R. Malladi, J. A. Sethian, and B. C. Vemuri, "Shape modeling with front propagation: A level set approach," *IEEE Transactions on Pattern Analysis and Machine Intelligence*, vol. 17, no. 2, pp. 158-175 1995.

[23] T. F. Cootes, D. H. Cooper, C. J. Taylor, and J. Graham, "A trainable method of parametric shape description," *Image and Vision Computing*, vol. 10, no. 5, pp. 289–294, 1992.

[24] K. S. Arun, T. S. Huang, and S. D. Blostein, "Least squares fitting of two 3-D point sets," *IEEE Transactions on Pattern Analysis and Machine Intelligence*, vol. 9, no. 5, pp. 698-700, 1987.

[25] B. K. P. Horn, H. M. Hilden, and S. Negahdaripour, "Closed form solution of absolute orientation using orthonormal matrices," *Journal of the Optical Society of America*, vol. 5, no. 7, pp. 1127-1135, 1988.

[26] S. Umeyama, "Least-squares estimation of transformation parameters between two point patterns," *IEEE Transactions on Pattern Analysis and Machine Intelligence*, vol. 13, no. 4, pp. 376-380, 1991.

[27] M. W. Walker, L. Shao, and R. A. Volz, "Estimating 3-D location parameters using dual number quaternions," *Computer Vision Graphics and Image Processing: Image Understanding*, vol. 54, no. 3, pp. 358 - 367, 1991.

[28] A. F. Siegel, "A robust comparison of biological shapes," *Biometrics*, vol. 38, pp. 341–350, 1982.

[29] I. L. Dryden and G. Walker, "Highly resistant regression and object matching," *Biometrics*, vol. 55, pp. 820–825, 1999.

[30] F. L. Bookstein, *Morphometric tools for landmark data: Geometry and biology*. Cambridge: Cambridge University Press, 1991.

[31] A. Hill and C. J. Taylor, "Automatic landmark generation for point distribution models," in British Machine Vision Conference (BMVC), York, 1994.

[32] A. C. W. Kotcheff and C. J. Taylor, "Automatic construction of eigenshape models by direct optimization," *Medical Image Analysis*, vol. 2, no. 4, pp. 303-314, 1998.

[33] R. H. Davies, C. J. Twining, T. F. Cootes, J. C. Waterton, and C. J. Taylor, "A minimum description length approach to statistical shape modeling," *IEEE Transactions on Medical Imaging*, vol. 21, pp. 525–537, 2002.

[34] H. H. Thodberg and H. Olafsdottir, "Adding curvature to minimum description length shape models," in British Machine Vision Conference (BMVC), 2003.

[35] P. Horkaew and G.-Z. Yang, "Optimal deformable surface models for 3D medical image analysis," in Information Processing in Medical Imaging (IMPI), 2003.

[36] A. Hill, A. D. Brett, and C.J.Taylor, "Automatic landmark identification using a new method of non-rigid correspondence," in Information Processing in Medical Imaging (IPMI), Poulteney, 1997.

[37] A. D. Brett and C. J. Taylor, "A method of automated landmark generation for automated 3D PDM construction," *Image and Vision Computing*, vol. 18, no. 9, pp. 739-748, 1999.

[38] Y. Wang, B. S. Peterson, and L. H. Staib, "Shape-based 3D surface correspondence using geodesics and local geometry," in IEEE Conference on Computer Vision and Pattern Recognition (CVPR), 2000.

[39] H. D. Tagare, "Shape-based nonrigid correspondence with application to heart motion analysis," *IEEE Transactions on Medical Imaging*, vol. 18, pp. 434–349, 1999.

[40] D. Rueckert, A. F. Frangi, and J. A. Schnabel, "Automatic construction of 3D statistical deformation models using non-rigid registration," in Medical Image Computing and Computer Assisted Intervention (MICCAI), 2001.

[41] A. F. Frangi, D. Rueckert, J. A. Schnabel, and W. J. Niessen, "Automatic construction of multiple-object three-dimensional statistical shape models: Application to cardiac modeling," *IEEE Transactions on Medical Imaging*, vol. 21, pp. 1151–1166, 2002.

[42] Y. Wang and L. H. Staib, "Boundary finding with prior shape and smoothness models," *IEEE Transactions on Pattern Analysis and Machine Intelligence*, vol. 22, no. 7, pp. 738-743, 2000.

[43] T. F. Cootes and C. J. Taylor, "Combining point distribution models with shape models based on finite element analysis," *Image and Vision Computing*, vol. 13, no. 5, pp. 403–409, 1995.

[44] C. Davatzikos, X. Tao, and D. Shen, "Hierarchical active shape models, using the wavelet transform," *IEEE Transactions on Medical Imaging*, vol. 22, pp. 414-423, 2003.

[45] M. d. Bruijne, B. v. Ginneken, M. Viergever, and W. Niessen, "Adapting active shape models for 3D segmentation of tubular structures in medical images," in Information Processing in Medical Imaging (IPMI), 2003.

[46] J. Lötjönen, K. Antila, E. Lamminmäki, J. Koikkalainen, M. Lilja, and T. F. Cootes, "Artificial enlargement of a training set for statistical shape models: Application to cardiac images," in Functional Imaging and Modelling of the Heart (FIMH), 2005.

[47] D. Shen and C. Davatzikos, "An adaptive-focus deformable model using statistical and geometric information," *IEEE Transactions on Pattern Analysis and Machine Intelligence*, vol. 22, pp. 906–913, 2000.

[48] S. Romdhani, S. Gong, and A. Psarrou, "A multi-view non-linear active shape model using kernel PCA," in British Machine Vision Conference (BMVC), Nottingham, 1999.

[49] P. D. Sozou, T. F. Cootes, and C. J. Taylor, "A non-linear generalisation of point distribution models using polynomial regression," in British Machine Vision Conference (BMVC), 1994.

[50] T. F. Cootes and C. J. Taylor, "A mixture model for representing shape variation," *Image and Vision Computing*, vol. 17, no. 8, pp. 567–574, 1999.

[51] T. F. Cootes and C. J. Taylor, "Active shape model search using local grey-level models: a quantitative evaluation," in British Machine Vision Conference (BMVC), 1993.

[52] B. v. Ginneken, A. F. Frangi, J. J. Staal, B. M. t. H. Romeny, and M. A. Viergever, "Active shape model segmentation with optimal features," *IEEE Transactions on Medical Imaging*, vol. 21, no. 8, pp. 924-933, 2002.

[53] F. Jiao, S. Li, H. Shum, and D. Shuurmans, "Face alignment using statistical models and wavelet features," *IEEE Conference on Computer Vision and Pattern Recognition*, vol. 1, 2003.

[54] D. Cristinacce and T. F. Cootes, "Boosted regression active shape models," in British Machine Vision Conference (BMVC), 2007.

[55] G. Langs, P.Peloschek, R. Donnner, M. Reiter, and H. Bischof, "Active feature models," in International Conference on Pattern Recognition (ICPR), Hong-Kong, 2006.

[56] T. F. Cootes, C. J. Taylor, and A. Lanitis, "Multi-resolution search with active shape models," in International Conference on Pattern Recognition, 1994.

[57] G. Behiels, F. Maes, D. Vandermeulen, and P. Suetens, "Evaluation of image features and search strategies for segmentation of bone structures in radiographs using active shape models," *Medical Image Analysis*, vol. 6, no. 1, pp. 47-62, 2002.

[58] G. Hamarneh and T. Gustavsson, "Deformable spatio-temporal shape models: extending active shape models to 2D+time," *Image and Vision Computing*, vol. 6, pp. 461-470, 2004.

[59] T. F. Cootes and C. J. Taylor, "Data driven refinement of active shape model search," in British Machine Vision Conference (BMVC), 1996.

[60] N. Duta and M. Sonka, "Segmentation and interpretation of MR brain images: an improved active shape model," *IEEE Transactions on Medical Imaging*, vol. 17, no. 6, pp. 1049-1067, 1998.

[61] H. Li and O. Chutatape, "Boundary detection of optic disk by a modified ASM method," *Pattern Recognition*, vol. 36, pp. 2093-2104, 2003.

[62] M. Rogers and J. Graham, "Robust active shape model search," in European Conference on Computer Vision (ECCV), 2002.

[63] M. d. Bruijne, B. v. Ginneken, M. A. Viergever, and W. J. Niessen, "Interactive segmentation of abdominal aortic aneurysms in CTA images," *Medical Image Analysis*, vol. 8, no. 2, pp. 127-138, 2004.

[64] T. Heimann, S. Münzing, H.-P. Meinzer, and I. Wolf, "A shape-guided deformable model with evolutionary algorithm initialization for 3D soft tissue segmentation," in Information Processing in Medical Imaging, Kerkrade, 2007.

[65] Z. Zhao, S. R. Aylward, and E. K. Teoh, "A novel 3D partitioned active shape model for segmentation of brain MR images," in Medical Image Computing and Computer-Assisted Intervention (MICCAI), Palm Spring, 2005.

[66] M. Seise, S. McKenna, I. W. Ricketts, and C. A. Wigderowitz, "Learning active shape models for bifurcating contours," *IEEE Transactions on Medical Imaging*, vol. 26, no. 5, pp. 666–677, 2007.

[67] H. C. v. Assen, M. G. Danilouchkine, A. F. Frangi, S. Ordas, J. J. M. Westenberg, J. H. C. Reiber, and B. P. F. Lelieveldt, "SPASM: A 3D-ASM for segmentation of sparse and arbitrarily oriented cardiac MRI data," *Medical Image Analysis*, vol. 10, no. 2, pp. 286-303, 2006.

[68] H. C. V. Assen, M. G. Danilouchkine, F. Behloul, H. J. Lamb, R. J. V. D. Geest, J. H. C. Reiber, and B. P. F. Lelieveldt, "Cardiac LV segmentation using a 3D active shape model driven by fuzzy inference," in Medical Image Computing and Computer Assisted Intervention (MICCAI), 2003.

[69] R. Casero and J. A. Noble, "A novel explicit 2D+t cyclic shape model applied to echocardiography," in Medical Image Computing and Computer Assisted Intervention (MICCAI), 2008.

[70] F. J. Rohlf, "Statistical power comparisons among alternative morphometric methods," *American Journal of Physical Anthropology*, vol. 111, no. 4, pp. 463–478, 2000.

[71] A. Hill and C. Taylor, "Model-based image interpretation using genetic algorithms," *Image and Vision Computing*, vol. 10, no. 5, 1992.

[72] M. Brejl and M. Sonka, "Object localization and border detection criteria design in edge-based image segmentation: automated learning from examples," *IEEE Transactions on Medical Imaging*, vol. 19, no. 10, pp. 973-985, 2000.

[73] M. d. Bruijne and M. Nielsen, "Shape particle filtering for image segmentation," in Medical Image Computing and Computer Assisted Intervention (MICCAI), 2004.

[74] K. Sjoestrand, M. B. Stegmann, and R. Larsen, "Sparse principal component analysis in medical shape modeling," in SPIE Medical Imaging: Image Processing, 2006.

[75] A. Suinesiaputra, M. Üzümcü, A. F. Frangi, T. A. M. Kaandorp, J. H. C. Reiber, and B. P. F. Lelieveldt:, "Detecting regional abnormal cardiac contraction in short-axis MR images using independent component analysis.," in Medical Image Computing and Computer Assisted Intervention (MICCAI), 2004.

[76] K. Y. E. Leung and J. G. Bosch, "Localized shape variations for classifying wall motion in echocardiograms," in Medical Image Computing and Computer Assisted Intervention (MICCAI), Brisbane, 2007.

[77] T. F. Cootes, D. Cooper, C. J. Taylor, and J. Graham, "A trainable method of parametric shape description," in British Machine Vision Conference (BMVC), 1991.

[78] G. Hamarneh and T. Gustavsson, "Deformable spatio-temporal shape models: extending ASM to 2D+time," *Image and Vision Computing*, vol. 22, no. 6, pp. 461-47, 2004.

[79] D. W. Thompson, *On growth and form*. Cambridge: Cambridge University Press, 1917.

[80] F. L. Bookstein, "Principal warps: Thin-plate splines and the decomposition of deformations " *IEEE Transactions on Pattern Analysis and Machine Intelligence*, vol. 11, no. 6, 1989.

[81] S. Lele and J. T. Richtsmeier, *An invariant approach to statistical analysis of shapes*. New York: Chapman & Hall, 2001.

[82] F. L. Bookstein, *The measurement of biological shape and shape change*. New York: Springer-Verlag, 1978.

[83] S. Lele, "Euclidean distance matrix analysis: Estimation of mean form and form differences," *Mathematical Geology*, vol. 25, pp. 573-602, 1993

[84] C. R. Rao and S. Suryawanshi, "Statistical analysis of shape through triangulation of landmarks: a study of sexual dimorphism in hominids," *Proc. of the National Academy of Sciences, U.S.A.*, vol. 95, no. 8, pp. 4121-4125, 1998.

[85] K. V. Mardia and P. E. Jupp, *Directional statistics*: Wiley, 2000.

[86] M. Hills, "On ratios-A response to Atchley, Gaskins, and Anderson," *Systematic Zoology*, vol. 27, no. 1, pp. 61-62 1978.

[87] H. S. M. Coxeter, "Barycentric coordinates," in *Introduction to geometry, 2nd ed.* New York: Wiley, 1969, pp. 216-221.

[88] M. Floater, "Parametrization and smooth approximation of surface triangulations," *Computer Aided Geometric Design*, vol. 14, no. 3, pp. 231–250, 1997.

[89] N. Sukumar and E. A. Malsch, "Recent advances in the construction of polygonal finite element interpolants," *Archives of Computational Methods in Engineering*, vol. 13, no. 1, pp. 129–163, 2006.

[90] S. Roweis and L. Saul, "Nonlinear dimensionality reduction by locally linear embedding," *Science*, vol. 290, pp. 2623-2326, 2000.

[91] J. Warren, "Barycentric coordinates for convex polytopes," *Advances in Computational Mathematics*, vol. 6, pp. 97–108, 1996.

[92] M. Meyer, H. Lee, A. J.Barr, and M. Desbrun, "Generalized barycentric coordinates on irregular polygons," *Journal of Graphics Tools*, vol. 7, no. 1, pp. 13-22, 2002.

[93] D. G. Kendall, "Shape manifolds, Procrustean metrics and complex projective spaces," *Statistical Science*, vol. 16, pp. 81-121, 1984.

[94] I. Guttman, *Statistical tolerance regions: Classical and Bayesian*. London: Griffin, 1970.

[95] E. v. Collani and K. Baur, "Prediction intervals, tolerance intervals and standards in quality control - Part I," *Economic Quality Control*, vol. 17, pp. 81-98, 2002.

[96] A. Wald and J. Wolfowitz, "Tolerance limits for a normal distribution," *Annals of Mathematical Statistics*, vol. 17, no. 208-215, 1946.

[97] W. G. Howe, "Two-sided tolerance limits for normal populations - some improvements," *Journal of the American Statistical Association*, vol. 64, pp. 610-620, 1969.

[98] J. W. Pratt and J. D. Gibbons, *Concepts of nonparametric theory*: Springer-Verlag, 1981.

[99] S. S. Wilks, "Determination of sample sizes for setting tolerance limits," *Annals of Mathematical Statistics*, vol. 12, pp. 91-96, 1941.

[100] M. Siotani, "Tolerance regions for a multivariate normal population," *Annals of the Institute of Statistical Mathematics*, vol. 16, pp. 135-, 1964.

[101] M. J. R. Healy, "Multivariate normal plotting," *Applied Statistics*, vol. 17, no. 2, pp. 157-161, 1968.

[102] C. Becker and U. Gather, "The masking breakdown point of multivariate outlier identification rules," *Journal of the American Statistical Association*, vol. 94, pp. 947-955, 1999.

[103] A. D. Bucchianico, J. H. J. Einmahl, and N. A. Mushkudiani, "Smallest non-parametric tolerance regions," *The Annals of Statistics*, vol. 29, no. 5, pp. 1320-1343, 2001.

[104] R. E. Strauss and F. L. Bookstein, "The Truss: Body form reconstructions in morphometrics," *Systematic Zoology*, vol. 31, no. 2, pp. 113-135 1982.

[105] F. J. Rohlf and J. W. Archie, "Least-squares mapping using interpoint distances," *Ecology*, vol. 59, no. 1, pp. 126-132, 1978.

[106] C. Davatzikos, X. Tao, and D. Shen, "Hierarchical active shape models, using the wavelet transform," *IEEE Transactions on Medical Imaging*, vol. 22, pp. 414-423, Mar. 2003.

[107] H. Lilliefors, "On the Kolmogorov–Smirnov test for normality with mean and variance unknown," *Journal of the American Statistical Association*, vol. 62, pp. 399–402, 1967.

[108] S. J. Russell and P. Norvig, *Artificial intelligence: a modern approach*: Prentice-Hall, 2003.

[109] T. F. Cootes, A. Hill, C. J. Taylor, and J. Haslam, "The use of active shape models for locating structures in medical images," *Image and Vision Computing*, vol. 12, no. 6, pp. 355-366, 1994.

[110] L. A. Crowe, P. Gatehouse, G.-Z. Yang, R. H. Mohiaddin, A. Varghese, C. Charrier, J. Keegan, and D. N. Firmin, "Volume selective 3D TSE imaging for vascular wall imaging and distensibility measurement," *Journal of Magnetic Resonance Imaging*, vol. 17, pp. 572-580, 2003.

[111] V. Chalana, D. T. Linker, D. R. Haynor, and Y. Kim, "A multiple active contour model for cardiac boundary detection on echocardiographic sequences," *IEEE Transactions on Medical Imaging*, vol. 15, pp. 290–298, 1996.

[112] S. C. Mitchell, J. G. Bosch, B. P. F. Lelieveldt, R. J. V. D. Geest, J. H. C. Reiber, and M. Sonka, "3-D active appearance models: segmentation of cardiac MR and

ultrasound images," *IEEE Transactions on Medical Imaging*, vol. 21, no. 9, pp. 1167-1178, 2002.

[113] S. C. Mitchell, B. P. F. Lelieveldt, R. J. v. d. Geest, H. G. Bosch, J. H. C. Reiver, and M. Sonka, "Multistage hybrid active appearance model matching: segmentation of left and right ventricles in cardiac MR images," *IEEE Transactions on Medical Imaging*, vol. 20, no. 5, pp. 415-423, 2001

[114] G. Jacob, J. A. Noble, C. Behrenbruch, A. D. Kelion, and A. P. Banning, "A shape-space-based approach to tracking myocardial borders and quantifying regional left-ventricular function applied in echocardiography," *IEEE Transactions on Medical Imaging*, vol. 21, no. 3, pp. 226-238, 2002.

[115] J. G. Bosch, F. Nijland, S. C. Mitchell, B. P. F. Lelieveldt, O.Kamp, M.Sonka, and J. H. C. Reiber, "Computer-aided diagnosis via model-based shape analysis: automated classification of wall motion abnormalities in echocardiograms," *Academic Radiology*, vol. 12, no. 3, pp. 358-367, 2005.

[116] P. J. Huber, *Robust statistics*. New York: Wiley, 1981.

[117] "http://www.cmrtools.com/cmrweb/LVtoolsIntroduction.htm."

[118] S. Masood, G.-Z. Yang, D. J. Pennell, and D. N. Firmin, "Investigating intrinsic myocardial mechanics: the role of MR tagging, velocity phase mapping, and diffusion imaging," *Journal of Magnetic Resonance Imaging*, vol. 12, no. 6, pp. 873-83, 2000.

[119] P. Geladi and B. Kowlaski, "Partial least square regression: A tutorial," *Analytica Chemica Acta*, vol. 35, pp. 1–17, 1986.

[120] F. Cecchi, M. H. Yacoub, and I. Olivotto, "Hypertrophic cardiomyopathy in the community: why we should care," *Nature Clinical Practice Cardiovascular Medicine*, vol. 2, no. 7, pp. 324-325, 2005.